TÉCNICO LISBOA

Probing the quark gluon plasma medium through B meson production measurements in PbPb collisions at the LHC

Júlia Manuela Cardoso Silva

Thesis to obtain the Master of Science Degree in

Engineering Physics

Supervisor: Prof. Dr. Nuno Teotónio Viegas Guerreiro Leonardo

Examination Committee

Chairperson: Prof. Dr. Jorge Manuel Rodrigues Crispim Romão
Supervisor: Prof. Dr. Nuno Teotónio Viegas Guerreiro Leonardo
Member of the Committee: Prof. Dr. José Ricardo Morais Silva Gonçalo

October 2019

To my sisters.

.

Acknowledgments

First and foremost I acknowledge LIP, specially the CMS-LIP group for allowing me to start my life as an experimental particle physics researcher. I further acknowledge my supervisor, who guided me through stressful times, always being available to provide feedback. I will be forever thankful for all the knowledge he imparted me with. This work was done in collaboration with the MIT Heavy Ion Group and so I would like to thank all its members. A special thanks goes to Gwang-Jun Kim and Zhaozhong Shi, my fellow analysers. Furthermore, while doing this work at LIP, I had the pleasure to help supervise some students for some months. So another thanks goes to Alexandra Ramalho, João Gonçalves and Giuseppe Crupi, for their hard work and for being my brothers in arms. I further thank all the people from LIP who made this experience more enjoyable, and who were always ready to help, whenever I asked: Ana Luísa, Diogo, Beatriz, Ricardo, Glória, João, Mariana, Marco and Alex. Thanks for all the lunches, all the dinners, all the ”Carocha do Amor” listening parties, and for being all around an awesome group.

I would now like to thank the people who helped review this thesis: Bruno, João and Ana Luísa. Your input is always invaluable. An extra special thanks goes to Gonçalo, who didn't just review this thesis but made sure I would not despair until submission time. Even being in Italy, you keep being there in the most crucial times. I hope I can deserve your friendship one day.

I want to thank the people who were not directly involved with getting this thesis ready, but still helped indirectly. First, I thank Cristóvão for being the best teacher while I did my summer internship at LIP. He is one of the most knowledgeable people I know and one of the researchers I look up to the most. I would like to thank António for helping me become a better programmer, and for being my connection with society whenever I go to my hometown. Skype sessions with you are the best kind of Skype sessions. I thank my friend Laura for her amazing pep-talks. I am sorry that I couldn't see you in Lisbon, but I will make it a priority to visit you, whenever it is possible. You were indeed my summer love. I further thank Daniel for checking up on my sanity, and for being the best person I will ever have the pleasure to play with.

I cannot list all the important people in my life, so I won't try. You know who you are and I will tell you each chance I get. But I would be remiss if I didn't thank the most important ones, my family. An enormous thank you goes to my aunt and uncle for giving me a home while I was studying and for enduring my many sleepless nights in the kitchen. Thank you Elsa for always supporting me and for being the kindest person I know. Thank you Filipa for always worrying about me and for inspiring me to become a researcher. And last, but not least, thanks mom and dad for raising me and for teaching me to be a good person, by example. Even though I won't be a doctor, I hope to make you proud.

Resumo

Colisões de iões pesados relativistas permitem o estudo de Cromodinâmica Quântica a densidades e temperaturas elevadas. Nestas condições, prevê-se a formação do Plasma de Quarks e Gluões (QGP). Estas colisões de iões pesados produzem ainda, no seu início, quarks pesados, que consequentemente viverão através da evolução completa do QGP. Medidas exclusivas da produção de *beauty* dão precisão ao estudo da perda de energia dos partões e permitem sondar a influência do sabor. Uma superprodução de *tstrangeness* é prevista no meio em estudo. Se a hadronização de *beauty* tiver uma contribuição significativa de recombinação com quarks no meio, a produção de B_s relativamente à de B^+ vai aumentar. Esta análise usa dados adquiridos pelo *Compact Muon Solenoid* em colisões de PbPb com uma energia de centro de massa de 5.02 TeV, no *Large Hadron Collider*. A primeira observação significativa do mesão B_s em colisões PbPb é conseguida, com uma significância acima de 5 sigma. Secções eficazes de B_s e B^+ são medidas em função de momento transverso p_T e centralidade. Os rácios entre as duas são calculados e comparados com medidas publicadas de f_s/f_u em colisões de pp. Evidências de hadronização de beauty através de recombinação no meio são apresentadas para B p_T baixo e colisões mais centrais. Factores de modificação nucleares são calculados para p_T no intervalo de 15-50 GeV/c, usando valores publicados das secções eficazes de B_s em colisões pp. Esta medida indica supressão da produção de B_s, na região cinemática estudada.

Keywords: Plasma de quarks e gluões, *Large Hadron Collider*, *Compact Muon Solenoid*, Física dos Mesões B, Colisões de Iões Pesados, Secções Eficazes.

Abstract

Relativistic heavy ion collisions allow the study of Quantum Chromodynamics at high energy density and temperature. Under such conditions, a medium of deconfined quarks and gluons is predicted to be formed, the Quark-Gluon Plasma (QGP). Heavy quarks are produced in the early stages of heavy ion collisions, experiencing the full evolution of the QGP medium. Exclusive beauty production measurements add precision to the study of parton energy loss and allow to probe its flavour dependence. An enhancement in strangeness content is expected in the probed medium. If beauty hadronisation happens through quark-recombination in the QGP, B_s production is expected to be larger than B^+ production. This work employs data collected by the Compact Muon Solenoid, in PbPb collisions with a center-of-mass energy of 5.02 TeV, at the Large Hadron Collider. The first observation of B_s in PbPb is presented, with a significance over 5 sigma. B_s and B^+ cross sections are measured as a function of transverse momentum (p_T) and centrality. The ratios between the two are computed and compared to the fragmentation fraction ratio f_s/f_u, measured in pp collisions. Evidences of bottom hadronisation through recombination in the medium are shown for low B p_T and more central collisions. Using the published B_s cross sections in pp collisions, in the p_T range of 15-50 GeV/c, the B_s nuclear modification factor is computed. The measurements indicate an overall suppression of B_s production in the QGP medium, in the probed kinematic region.

Keywords: Quark Gluon Plasma, Large Hadron Collider, Compact Muon Solenoid, B Physics, Heavy Ion Collisions, Cross sections.

Contents

Acknowledgments v
Resumo vii
Abstract ix
List of Tables xiii
List of Figures xv
Glossary xix

1 Introduction **1**
1.1 Theoretical Framework 1
1.1.1 Quantum Chromodynamics 2
1.1.2 Quark-Gluon Plasma 3
1.1.3 Ultrarelativistic Heavy Ion Collisions 4
1.2 Heavy Flavour Probes of the QGP 6
1.2.1 B mesons 8
1.2.2 Production Measurements 10
1.2.3 State of the Art 11
1.3 Thesis Outline 13

2 Experimental Framework **15**
2.1 The Large Hadron Collider 15
2.2 Compact Muon Solenoid 17
2.2.1 CMS Coordinate System and Parametrization 17
2.2.2 Silicon Tracker 18
2.2.3 Hadron Calorimeter 19
2.2.4 Muon Stations 21
2.2.5 Trigger System 21

3 Data, MC Samples and Selection **23**
3.1 Datasets 23
3.2 Monte Carlo Samples 24
3.3 B meson Reconstruction and Baseline Selection 24
3.4 Optimised Selection 27

3.5 Fiducial Region . . . 31

4 Signal Extraction **33**

4.1 Extended Unbinned Maximum Likelihood Method . . . 33

4.2 Invariant Mass Fits . . . 34

4.3 Signal Statistical Significance . . . 36

5 Acceptance and Efficiency **39**

5.1 Acceptances and Efficiencies Estimation . . . 39

5.2 Muon Efficiency: Tag and Probe Corrections . . . 41

6 Data-MC Comparison **43**

6.1 Sideband Subtraction Method . . . 43

6.2 SPlot Method . . . 45

6.3 Method Comparison . . . 46

6.4 Variable Distributions . . . 48

7 Systematic Uncertainties **51**

7.1 PDF Variation . . . 51

7.2 Fit Bias . . . 55

7.3 Efficiency Systematics . . . 56

7.4 Summary . . . 58

8 Results and Discussion **61**

8.1 Cross Section . . . 61

8.2 B_s/B^+ Production Ratio . . . 64

8.3 Nuclear Modification Factors . . . 66

9 Conclusions **69**

Bibliography **71**

List of Tables

1.1 Properties of B mesons ground states [2]. 8
1.2 b fragmentation fractions in $Z \to b\bar{b}$, and in $p\overline{p}$ collisions at $\sqrt{s} = 1.96$ TeV [2]. 9
1.3 Measured branching fractions used in this thesis [2]. 10

3.1 List of PbPb HLT datasets and triggers with the corresponding integrated luminosities used in the analysis. 24
3.2 Selection criteria used for B_s, depending on its p_T. 31
3.3 Selection criteria used for B^+, depending on its p_T. 32

7.1 Summary table of the value obtained for the parameter *a*, when using the signal model described by (7.1), in different p_T bins. 53
7.2 Total systematic uncertainties associated with PDF variation for B^+ p_T bins. All values are in units of %. 55
7.3 Total systematic uncertainties associated with PDF variation for inclusive B^+ p_T and different centrality bins. All values are in units of %. 55
7.4 Total systematic uncertainties associated with PDF variation for B_s p_T bins. All values are in units of %. 55
7.5 Total systematic uncertainties associated with PDF variation for inclusive B_s p_T and different centrality bins. All values are in units of %. 55
7.6 Relative systematic uncertainty associated with fit bias, for both channels of the analysis. 56
7.7 Efficiency systematic uncertainties for different B^+ p_T bins, calculated from the discrepancies between data and MC for BDT score. This comparison was done using the B^+ channel. 57
7.8 Efficiency systematic uncertainties, for different centrality ranges, calculated from the discrepancies between data and MC for BDT score. This comparison was done using the B^+ channel. 57
7.9 Efficiency systematic uncertainties for different B_s p_T bins, calculated with 7.4. The B^+ channel was used as a baseline channel. 58
7.10 Efficiency systematic uncertainties for different centrality ranges, calculated with 7.4. The B^+ channel was used as a baseline channel. 58
7.11 Global systematic uncertainties of the analysis. All the values are in form of percentages. 59

7.12 Summary of systematic uncertainties from each factor for different p_T bins within centrality 0-90% of B_s. All the values are shown in percentage. 59
7.13 Summary of systematic uncertainties for the B_s meson, for different centrality ranges. All the values are shown in percentage. 59
7.14 Summary of systematic uncertainties from each factor for different p_T bins within centrality 0-90% of B^+. All the values are shown in percentage. 60
7.15 Summary of systematic uncertainties for the B^+ meson, for different centrality ranges. All the values are shown in percentage. 60

8.1 Summary of the $N_{\rm coll}$, $T_{\rm AA}$ and $N_{\rm part}$ values for the centrality bins used in the analysis. In brackets are also the associated systematic uncertainties [25]. 62
8.2 Cross section measurements for 0-90% centrality, within the analysis fiducial region defined in (3.3). 64
8.3 Production ratio in different centrality ranges. 65
8.4 B_s nuclear modification factor for the two p_T intervals studied. 67

List of Figures

1.1 Schematic of the SM, including all the known particles divided in quarks, leptons, gauge bosons and the Higgs. The masses, charges and spins of each particle are displayed. . . 1

1.2 Current understanding of the QCD phase diagram, as funcion of baryon doping and temperature [5]. 4

1.3 Schematic of the proposed space-time evolution of the medium, with and without QGP [6]. We are assuming the b) possibility. 5

1.4 Schematic of the geometry used in the Glauber model [8]. A longitudinal view and a transverse view are shown. 6

1.5 Feynman diagrams for the medium induced energy loss processes. 7

1.6 Measured $f_s/(f_u + f_d)$ and $f_{\Lambda_b}/(f_u + f_d)$ in pp collisions, at $\sqrt{s} = 13$ TeV [13]. The ratios are presented as a function of the transverse momentum of the b hadron. A strong dependence is verified for $f_{\Lambda_b}/(f_u + f_d)$. 9

1.7 Feynman diagrams for the decays relevant for this thesis [16]. 10

1.8 Nuclear modification factors of different hadrons, measured in PbPb collisions at $\sqrt{s}$ =5.02 TeV, as a function of transverse momentum. Results obtained by the CMS Collaboration [9]. 12

1.9 Measurements of strange heavy flavour meson production relative to their non-strange counterparts, as a function of transverse momentum [9]. 13

1.10 B_s nuclear modification factor measured in two p_T intervals, in the range 7-50 GeV/c (pink data points). This measurement was performed with the smaller 2015 dataset, with an integrated luminosity of 351 μb^{-1} [18]. Overlaid is also the B^+ nuclear modification obtained with the same dataset (blue data points). The rectangular boxes, in both cases, represent the systematic uncertainties. 13

2.1 Schematic of the accelerator sequence at the LHC. 16

2.2 The integrated luminosity delivered by the LHC, and measured by CMS, for lead-lead collisions during 2018 [21]. 17

2.3 Transverse view of the CMS detector, showing its different layers. 18

2.4 z-R transverse section of the CMS detector [23]. 19

2.5 A view of the CMS detector in y-z projection with specified components of the hadronic calorimeter. 20

2.6 Distribution of the sum of HF measured total transverse energy, and the corresponding division of the event sample in centrality classes [25]. 20

3.1 A schematic of the B^+ meson decay and the definitions of variables included in the BDT training [32]. 25

3.2 Muon p_T and η 2D distribution in Monte Carlo simulation. The red line represents the single muon acceptance cuts applied [33]. 26

3.3 Flowchart of the B_s meson reconstruction workflow [32]. 27

3.4 Input variables signal and background distributions for MVA training used in PbPb B_s p_T 20-50 GeV/c. 30

3.5 Background and signal efficiencies, and the value of the figure of merit used as a function of the cut applied to the BDT score, in the case of B_s candidates with p_T of 20-50 GeV/c. 31

3.6 2-dimensional maps in p_T and y of B^+ candidates that met all the selection requirements. 32

3.7 2-dimensional map in p_T and $|y|$ of B_s candidates that met all the selection requirements. 32

4.1 Fit results associated with the signal extraction for B_s, for the centrality range 0%-90%, and the B p_T range of 7-50 GeV/c. The parameters shown in the boxes are the ones left free when fitting. In black are the data points; in blue the background model; in yellow the signal model; and in red the resulting total model. 36

4.2 Fit results associated with the signal extraction for B^+, for the centrality range 0%-90%, and the B p_T range of 5-60 GeV/c. The parameters shown in the boxes are the ones let free when fitting. In black are the data points; in blue the combinatorial background model; in yellow the signal model; in green the non-prompt background; and in red the resulting total model. 37

5.1 Product of B^+ meson acceptance and efficiency as a function of p_T and y within 0-90% centrality. The TnP scaling has already been applied. 40

5.2 Product of B meson acceptance and efficiency correction factors as a function of p_T within 0-90% centrality. The TnP scaling is included. 41

5.3 TnP scaling factors applied in efficiency calculation for B^+, as function of p_T and y. Computed in the centrality range 0%-90%. 42

6.1 Distribution of the separation variable (a). Distributions of one variable of interest, obtained through the sideband subtraction method (b). 44

6.2 Comparison between the signal B p_T distribution obtained with the sideband subtraction method (blue), and its distribution from MC simulation. The bottom panel displays the ratio between the two. 45

6.3 Signal (red) and background (blue) distributions of B^+ p_T, obtained by re-weighting the original distribution in data with the weights calculated through the SPlot method. 46

6.4 Comparison between the signal B p_T distribution obtained with the SPlot method (red), and its distribution from MC simulation (green). The bottom panel displays the ratio between the two. 47

6.5 Comparison between signal distributions obtained through the SSM (blue) and SPlot (red) for B^+ p_T. These distributions are further compared with the distribution in MC (green). . 47

6.6 Comparison of B^+ BDT score distributions in data (obtained through SPlot) and MC. . . . 49

6.7 Comparison of B_s BDT score distributions in data (obtained through SPlot) and MC. . . . 50

6.8 Comparison of B^+ distributions in data (obtained through SPlot) and MC, for track-related variables. Transverse momentum of the kaon (Top left); Pseudo-rapidity of the kaon (Top right); Transverse distance to the primary vertex (Bottom left); Longitudinal distance to the primary vertex (Bottom right). 50

7.1 Invariant mass fit of B_s candidates. The background PDF from left to right is linear, 2nd order polynomial and 3rd order polynomial. 52

7.2 Invariant mass fit of B^+ candidates for $5 < p_T < 50$ GeV/c, with an extra free parameter in the signal model *a*, as described by (7.1) ('c11' in the parameter box). 53

7.3 Invariant mass fit of B_s candidates. From left to right, top to bottom, the chosen signal pdf is triple gaussian (with widths and relative proportions fixed from MC), double gaussian with all the parameters fixed (including the mean), increased width (*a*=1.1), and decreased width (*a*=0.9). 54

7.4 Pull distributions obtained from toy MC study. 56

7.5 Comparison of nominal $\langle 1/(\alpha \times \epsilon) \rangle$ correction factor with the one obtained with re-weighted MC. 57

8.1 B^+ cross section in PbPb collisions, as a function of p_T. The measurement was performed within the analysis fiducial region, defined in (3.3). The data points (represented at the weighted-average of the p_T distributions of each bin), and their respective statistical uncertainties can be seen in light red. The rectangular boxes represent the systematic uncertainties. The horizontal bars do not represent uncertainties, but the range of the p_T bin. The p_T bins range from 5 to 60 GeV/c. 63

8.2 B_s cross section in PbPb collisions, as a function of p_T. The measurement was performed within the analysis fiducial region, defined in (3.3). The data points (represented at the weighted-average of the p_T distributions of each bin), and their respective statistical uncertainties can be seen in light red. The rectangular boxes represent the systematic uncertainties. The horizontal bars do not represent uncertainties, but the range of the p_T bin. The p_T bins range from 7 to 50 GeV/c. 63

8.3 B_s/B^+ production ratio, as a function of p_T. The measurement was performed within the analysis fiducial region, defined in (3.3). The data points (represented at the weighted-average of the B_s p_T distributions of each bin), and their respective statistical uncertainties can be seen in light red. The rectangular boxes represent the systematic uncertainties. The horizontal bars do not represent uncertainties, but the range of the p_T bin. The p_T bins range from 7 to 50 GeV/c. The f_s/f_u in pp collisions (LHCb measurement) is also displayed, for comparison [13]. The smaller (black) error bars represent the bin-by-bin systematics of that analysis, and the blue error bars represent the global uncertainties. The resulting function from the linear fit to those data points (performed in the LHCb analysis) is superimposed, in blue. The dashed lines give the total uncertainties on the fit results. 65

8.4 B_s/B^+ production ratio, as a function of $\langle N_{part} \rangle$ (corresponding to the centrality class being studied). The measurement was performed within the analysis fiducial region, defined in (3.3). The data points, and their respective statistical uncertainties can be seen in light red. The rectangular boxes represent the systematic uncertainties. The average fragmentation fraction ratio f_s/f_u, measured by LHCb in pp collisions [13] within its uncertainty is represented in blue. 66

8.5 B_s nuclear modification factor measured in two p_T intervals, in the range 15-50 GeV/c. The cross sections measured in this work were normalised by the cross sections measured in pp collisions at the same center-of-mass energy, published by CMS [18]. The data points (represented at the center of the bin), and their respective statistical uncertainties can be seen in light red. The rectangular boxes represent the systematic uncertainties. The horizontal bars do not represent uncertainties, but the range of the p_T bin. 67

Glossary

ALICE	A Large Hadron Collider Experiment
ATLAS	A Toroidal LHC Apparatus
BDT	Boosted Decision Tree
CMS	Compact Muon Solenoid
CSC	Cathode Strip Chambers
DT	Drift Tubes
EUML	Extended Unbinned Maximum Likelihood
HLT	High Level Trigger
IP	Interaction Points
LEP	Large Electron-Positron Collider
LHCb	Large Hadron Collider beauty
LHC	Large Hadron Collider
LIP	*Laboratório de Instrumentação e Física Experimental de Partículas*
MC	Monte Carlo
MVA	Multivariate Analysis
NN	Neural Network
PDF	Probability Density Function
PDG	Particle Data Group
PD	Primary Datasets
QCD	Quantum Chromodynamics
QED	Quantum Electrodynamics
QGP	Quark-Gluon Plasma
RF	Radiofrequency
RHIC	Relativistic Heavy Ion Collider
RPC	Resistive Plate Chambers
SM	Standard Model
SSM	Sideband Subtraction Method
TnP	Tag and Probe

Chapter 1

Introduction

1.1 Theoretical Framework

The Standard Model (SM) is the most complete theory built until today that includes all the known elementary particles and describes how they interact through three fundamental forces: electromagnetic, weak and strong. These particles are grouped in fermions (half-integer spin) and bosons (integer spin). The gauge bosons (W, Z, γ, g) serve as mediators of the forces. In the fermions category we have quarks (which couple to the electroweak and strong interaction mediators) and leptons (that only couple to the electroweak bosons). Figure 1.1 lists some properties of the SM particles. In its core the SM is the combination of two quantum field theories: electroweak theory - unified weak theory and quantum electrodynamics (QED) - and quantum chromodynamics (QCD). This can be formulated mathematically by a Lagrangian that is invariant under the gauge transformations of the symmetry group

$$SU(3)_C \times SU(2)_L \times U(1)_Y,$$

where C stands for colour, L the left chirality component of a fermion, and Y for hypercharge [1].

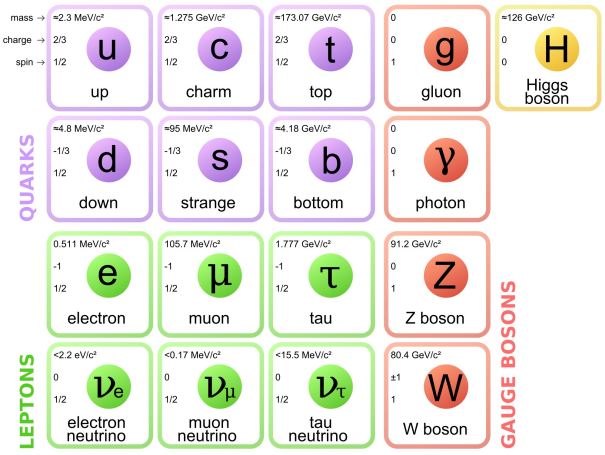

Figure 1.1: Schematic of the SM, including all the known particles divided in quarks, leptons, gauge bosons and the Higgs. The masses, charges and spins of each particle are displayed.

1.1.1 Quantum Chromodynamics

QCD is the theory that describes the strong force, corresponding to the $SU(3)_C$ component of the SM gauge group. This interaction is mediated by gluons that couple to particles that possess colour charge: quarks. There are three generations of quarks: up and down make the first, charm and strange the second, and the third is composed by the top and bottom quarks. Doing an analogy between QCD and QED, the colour charge is analogous to the electric charge. Nevertheless, contrary to the photon, the gluon does carry this colour charge, and as such, can couple to itself. Bound states of gluons and quarks (hadrons) are colour-neutral. Depending on how many valence quarks the hadron contains, the hadron can be referred to as a baryon (3 quarks with different colours) or a meson (a quark with its colour and an anti-quark with its anti-colour). The QCD langrangian can be written as [2]

$$L_{QCD} = \sum_q \overline{\Psi}_{q,a} \left(i\gamma^\mu \partial_\mu \delta_{ab} - g_s \gamma^\mu t^C_{ab} A^C_\mu - m_q \delta_{ab} \right) \Psi_{q,b} - \frac{1}{4} F^A_{\mu\nu} F^{A\mu\nu}. \tag{1.1}$$

γ_μ are the Dirac matrices, $\Psi_{q,a}$ are the quark fields of mass m_q, flavour *q* and colour a (a goes from 1 to 3). g_s is the QCD coupling constant, A^C_μ are the gluon fields and t^C_{ab} are the generators of the SU(3) group. C is the colour index and it runs from 1 to 8, which means there are 8 different types of gluons. t^C_{ab} are also 8 matrices, defined as $t^C_{ab} = \frac{\lambda^C_{ab}}{2}$, where λ^C_{ab} are the Gell-Mann matrices. We can physically interpret the second term of the sum by noting that a gluon will couple with a quark, taking away its colour and replacing it with another. The last term of this Lagrangian is purely gluonic, being the gluon field tensor, defined as

$$F^A_{\mu\nu} = \partial_\mu A^A_\nu - \partial_\nu A^A_\mu - g_s f_{ABC} A^B_\mu A^C_\nu, \tag{1.2}$$

in which f_{ABC} are the structure constants of SU(3). Looking at the Lagrangian we can see that the parameters of QCD are the quark masses and the coupling constant g_s or $\alpha_s = \frac{{g_s}^2}{4\pi}$. This is a running coupling constant, arising from the vacuum polarization. Just like we would have for electric charge, quark-antiquark pairs screen the colour charge, and if that were the only effect, we would measure a decreasing value for longer distances, or low momentum transfers. But in the case of QCD there is also gluon pair formation, that will ”smear” the colour charge and have an ”antiscreening” effect. This latter effect will be the dominant one. Fixing α_s at a certain energy scale μ^2, we can find that, after renormalization, the expression for α_s at the energy scale Q^2 is [3]

$$\alpha_s(Q^2) = \frac{\alpha_s(\mu^2)}{1 + \frac{\alpha_s(\mu^2)}{12\pi}(33 - 2N_f) ln\left(\frac{Q^2}{\mu^2}\right)}, \tag{1.3}$$

where N_f is the number of quark flavours actively contributing to the loops, namely those with mass $m_q < Q$. From this expression we can see that for high values of Q^2, α_s goes to 0. This property of QCD is called ’asymptotic freedom’ and indicates that when particles with colour charge are very close and have a high momentum transfer their interaction is weak, and they behave in a deconfined manner. On the other hand, for low energy transfers (long distances), α_s diverges, and quarks and gluons are in a state of ’confinement’. This is the reason why, experimentally, at normal energies, quarks and gluons

are never observed as free particles, and only as components of colour-neutral hadrons. In fact, the quark-antiquark interaction may be described by the effective potential

$$V_s = -\frac{4}{3}\frac{\alpha_s}{r} + kr. \tag{1.4}$$

The kr term comes from the gluon self-interaction effect. When trying to pull the quark and the anti-quark apart, the potential will become higher and higher, to the point that it will be energetically more favourable for the gluons to create a new quark-antiquark pair. All the quarks hadronise except for the top that is too heavy, and decays before that can happen.

An implication of the running α_s is that at low energies, because it diverges, a perturbative approach cannot be used. A frequent solution is the use of lattice QCD. In this approach, the QCD Lagrangian is discretised to a lattice of finite space-time points in which the Lagrangian can be solved [4].

1.1.2 Quark-Gluon Plasma

The property of asymptotic freedom anticipates that at high energy densities QCD matter undergoes a phase transition from a state composed by hadrons to a deconfined state of quarks and gluons, the quark-gluon plasma (QGP) [5]. The particles in this medium are deconfined, but far from behaving independently. In fact, they are strongly coupled, forming a collective medium that expands and flows as a relativistic hydrodynamic fluid, with a very low viscosity to entropy ratio. Analogous to a plasma with electric charges, the colour charges of quarks and gluons will be screened, and the QGP will be quasi-neutral as a whole. This state is predicted to have existed a microsecond or so after the Big Bang. After that, through expansion and cooling, there was the transition to hadronic matter. The physical conditions necessary for the existence of QGP can be shown in the QCD phase diagram (Figure 1.2). This is sketched as a function of temperature and baryon doping (excess of quarks over antiquarks), parametrized by the baryonic chemical potential (μ_B).

To summarise, it is predicted that at low temperatures and for $\mu_B \approx 1$ GeV, QCD matter is in its standard conditions (nuclear matter); as the energy density of the system increases (increasing T or μ_B) the hadronic gas phase is reached and increasing it further, and the QGP is formed. Lattice QCD calculations at $\mu_B = 0$ predict a critical temperature (T_c) for the transition of about 155 MeV [5]. For low baryon doping, the transition between hadron gas and QGP is known to be a crossover (free energy function and its derivatives are continuous). At higher doping, the transition may become first-order (transition occurs with a discontinuous pattern in the first derivative of the free energy) at some critical point.

In the beginning of the universe it is expected to have existed equal amounts of matter and anti-matter, which implies $\mu_B = 0$. That indicates that the transition between primordial QGP and hadrons was a continuous crossover, meaning that no fluctuations were introduced beyond the femtometre scale. This means that we cannot cosmologically observe this primodial QCD medium. Then, how can it be studied?

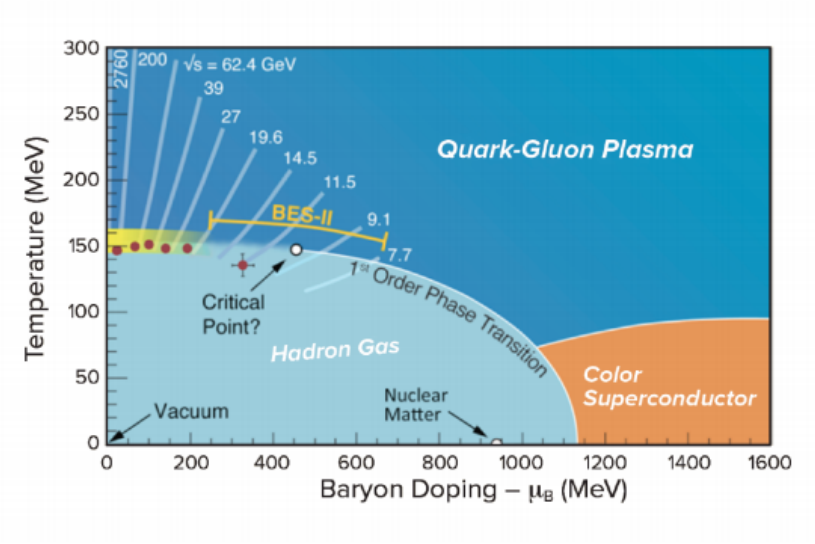

Figure 1.2: Current understanding of the QCD phase diagram, as funcion of baryon doping and temperature [5].

1.1.3 Ultrarelativistic Heavy Ion Collisions

In the past decades, collisions between protons and also heavy ions have been done at increasingly high energies at the Large Hadron Collider[1] (LHC). By colliding heavy ions it is possible to obtain energy densities much higher than those of standard matter. In these conditions, as explained above, a transition to QGP occurs. So, heavy ion collisions at ultrarelativistic energies, enable the study of the QGP [5]. Next we will describe qualitatively the sequence of events and the evolution of the medium after such a collision and then discuss the geometry of the resulting system.

Starting with two incident nuclei that, for having reached great velocities, are Lorentz contracted discs. The diameter of the discs is about 14 fm (for nuclei like Pb or Au) and their thickness is about $14/\gamma$ fm (with $\gamma = 1/\sqrt{1-v_z^2}$, v_z being the velocity in the direction of the beam, in units of the speed of light). Each disc is composed by quarks and antiquarks, with the excess of three more quarks (q) over antiquarks ($\bar{q}$) per nucleon of the original nucleous and with $q\bar{q}$ coming from quantum fluctuations in the initial state wave functions. When the two disks overlap, most partons (quarks, antiquarks or gluons, in Feynman's language) will interact softly, i.e., with low momentum transfer, but some hard perturbative interactions will also occur, leading to a very important production of particles with high transverse momentum (p_T). We will come back to this later. We can describe the strong interactions between the disks by imagining transverse colour fields interacting, colour charges colliding, exchanging colour charge and creating longitudinal colour fields between the two receding disks (now with reduced energy) which then gradually decay into $q\bar{q}$ pairs and gluons. A mass of hot and dense matter is formed and thermalises quickly, forming the QGP. As the discs recede from each other and the QGP formed between them is expanding and cooling, new QGP is continually being created in the wake of each receding disc. This happens because there are newly created partons moving at nearly the speed of

[1] Introduced in the next chapter.

light, allowing new QGP to form once enough time has passed in their frame. Through this process, the discs gradually lose energy as partons separate from it.

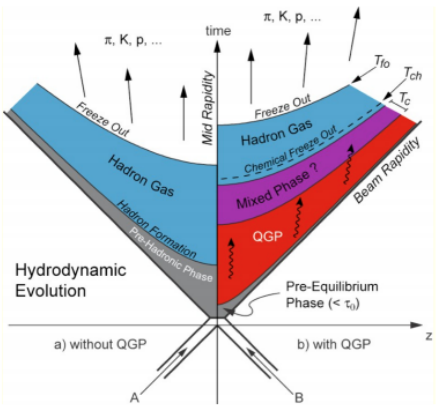

Figure 1.3: Schematic of the proposed space-time evolution of the medium, with and without QGP [6]. We are assuming the b) possibility.

The space-time evolution of the medium following the collision is schematised in Figure 1.3 . With the collision happening for $\tau = 0$, first there is a preequilibrium phase, when parton scattering takes place, until around $\tau = 1fm/c$ [5]. At this point, after thermalisation, because the energy density is high enough, the QGP is formed. The thermal pressure leads to expansion and the medium cools down, until it reaches the phase transition at T_c, and there is hadronization. This can happen instantaneously or through a mixed phase. At T_{ch}, occurs a chemical freeze-out and no more inelastic scatterings take place. This means that hadrons won't undergo more transitions, except through decays. The hadronic gas continues expanding, and the elastic interactions between hadrons occur in kinetic equilibrium. Once the density becomes too low, at freeze-out temperature (T_{fo}), the scatterings cease - this is called kinetic freeze-out. The hadrons decouple, their momenta are fixed, and they can decay sooner or later, depending on their lifetimes.

In these "messy" collisions, experimenters have direct control only over two variables: which nuclei are colliding and at which center-of-mass energy per nucleon-nucleon pair ($\sqrt{s_{NN}}$). However, knowing the colliding nuclei is not the same as knowing the colliding system. In fact, it's much harder to describe geometrically collisions between nuclei formed by multiple nucleons than proton-proton collisions. There are some new important parameters at play [7]:

- Impact parameter (b) - transverse distance between the centers of mass of the two colliding nuclei. It gives information on the centrality of a collision. Being that $0 \leq b \leq R_A + R_B$ (R_N is the radius of nucleus N), central collisions have $b \approx 0$. Collisions with large b are called peripheral.

- N_{part} - the number of participant nucleons within the colliding nuclei. The remaining nucleons are called spectators (N_{spec}). These continue travelling down the beam pipe, almost unaffected. In principle, N_{spec} can be measured directly, but it is difficult to do so, in practice.

- N_{coll} - the total number of nucleon binary collisions.

These parameters are not measured directly. To determine them, there is a well-defined probabilistic model ("Glauber Model Calculation"). To understand the fundamentals let's consider a target A and a projectile B (Figure 1.4).

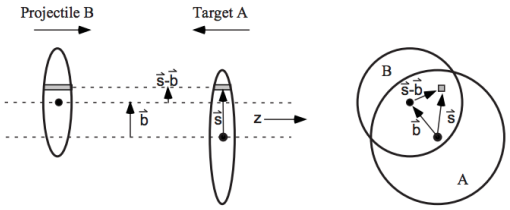

Figure 1.4: Schematic of the geometry used in the Glauber model [8]. A longitudinal view and a transverse view are shown.

b is measured from the target's center-of-mass. Let's focus on two overlapping flux tubes: one in A, at a distance s from its center; the other in B, at a distance s$-$b from its center. The probability per unit transverse area of a nucleon being located in the target flux tube is $T_A(s) = \int \rho_A(\boldsymbol{s}, z_A) dz_A$ where $\rho_A(\boldsymbol{s}, z_A)$ is the probability per unit volume, normalised to unity, for finding the nucleon at location $(\boldsymbol{s}, z_A)$. Then, the probability of nucleons being located in the respective overlapping target and projectile flux tubes is $T_A(\boldsymbol{s}) T_B(\boldsymbol{s} - \boldsymbol{b}) ds^2$. Integrating this expression we get the nuclear overlap function,

$$T_{AB}(b) = \int T_A(\boldsymbol{s}) T_B(\boldsymbol{s} - \boldsymbol{b}) ds^2. \tag{1.5}$$

This quantity can be interpreted as the effective overlap inverse area for which a given nucleon in A (with A nucleons) can interact with another nucleon in B (with B nucleons). It is called nuclear overlap function. Given the nucleon-nucleon inelastic cross section (σ_{NN}^{inel}), the probability of a specific nucleon in A interacting with a given nucleon in B is $T_{AB}(b)\sigma_{NN}^{inel}$. The corresponding probability of having n AB collisions is based in a binomial distribution:

$$P(n, b) = \binom{\mathsf{AB}}{n} [T_{AB}(b)\sigma_{NN}^{inel}]^n [1 - T_{AB}(b)\sigma_{NN}^{inel}]^{\mathsf{AB}-n}. \tag{1.6}$$

From this probability distribution we can calculate N_{coll},

$$N_{coll}(b) = \sum_{n=1}^{\mathsf{AB}} nP(n, b) = \mathsf{AB} \cdot T_{AB}(b)\sigma_{NN}^{inel}. \tag{1.7}$$

This formulation of the Glauber model works within the optical limit approximation [7].

1.2 Heavy Flavour Probes of the QGP

The QGP is short-lived and so it cannot be accessed directly. As such, experimenters need to use indirect ways to study this medium. Different probes can be used [6]: soft probes like anisotropic flow or electromagnetic ones (photons, leptons) or hard probes, like electroweak bosons, jets or heavy flavour.

We will focus on this last kind.

Heavy flavour quarks (namely charm and beauty quarks) are abundantly produced at the LHC and are particularly interesting as probes of the QGP medium giving us insight into its underlying mechanisms. These quarks are produced in the early stages of the heavy ion collisions, in hard scattering processes between partons of the incoming nuclei [9]. Because of their large masses, higher than QGP's critical temperature ($M_{c,b} > T_c$), their production time is shorter than the formation time of QGP. Opposite to what happens for light quarks and gluons, their thermal production and annihilation rates are negligible. Heavy quarks therefore experience the full evolution of the QGP medium, and are cleaner probes than light quarks and gluons, which may be generated or annihilated in different stages posterior to the heavy ion collisions.

Heavy flavour partons produced at the early stage of the collision interact with the medium throughout all its evolution, loosing energy through collisional and radiative processes. The first kind is due to elastic scatterings with the medium constituents (Figure 1.5, left). The second type is the dominant effect for hard partons energy loss in a strongly interacting environment and it happens through medium-induced gluon emission (Figure 1.5, right).

For this radiative energy loss, an important effect is predicted to create a dependence on quark flavour, the "dead cone effect". It predicts the following relation between the spectrum of soft gluons radiated by heavy quarks (dP_{HQ}) and the standard bremsstrahlung spectrum (dP_0) [10]

$$dP_{HQ} = dP_0 \left(1 + \frac{\theta_0^2}{\theta^2}\right)^{-2}, \tag{1.8}$$

with $\theta_0 = M_q/E_q$. It is clear to see that there will be a suppression of gluon radiation for angles smaller than the ratio between the mass of the quark and its energy. Then, energy loss is expected to be higher for lighter quarks that should lead to higher suppression of light-flavoured hadrons. Nevertheless, when E_q becomes large enough, this mass effect should cease. The study of hadrons of different flavours and masses should facilitate an understanding of such dependences of the underlying energy loss mechanisms in the medium.

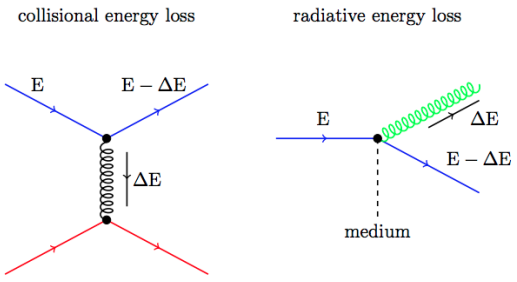

Figure 1.5: Feynman diagrams for the medium induced energy loss processes.

Heavy quarks are also great probes of the strangeness regeneration that is predicted to occur in the QGP medium. It was theoretically proposed that strangeness production in the QGP medium would be enhanced in comparison to a hadron gas. That should be consequence of the high rate of the process $gg \rightarrow s\bar{s}$, if the medium's temperature is above the strange quark mass [11]. Experimental results

obtained at the Relativistic Heavy Ion Collider (RHIC), for strange baryons and mesons, using different collision systems and beam energies, provide support for this prediction [12]. Furthermore, it was also suggested that low-momentum heavy quarks could hadronise via recombination with other quarks in the QGP [9]. If recombination in the medium is significant, one should expect to observe less suppressed strange D and B mesons with respect to lighter mesons of the same kind, in face of the medium with an increased strangeness content.

1.2.1 B mesons

As stated already, charm and bottom quarks are known as "heavy flavour" quarks. By studying the production of heavy flavour hadrons in heavy ion collisions, one can probe the generated medium for the theorised effects. We will focus on B meson production.

B mesons are comprised of two quarks - a bottom antiquark and a quark of a different flavour. Depending on that second quark we can have a B^+ ($\bar{b}u$), B^0($\bar{b}d$), B_s ($\bar{b}s$) or a B_c ($\bar{b}c$). Their rest masses and lifetimes can be found on Table 1.1. In this thesis the main focus will be on B^+ and B_s. Charge conjugated states are implied unless otherwise specified.

B Meson	Rest Mass [MeV]	Lifetime [ps]
B^+	5279.31 $\pm$ 0.15	1.638 $\pm$ 0.004
B^0	5279.62 $\pm$ 0.15	1.520 $\pm$ 0.004
B_s	5366.82 $\pm$ 0.22	1.511 $\pm$ 0.014
B_c	6274.9 $\pm$ 0.8	0.507 $\pm$ 0.009

Table 1.1: Properties of B mesons ground states [2].

In hadron collisions, $b\bar{b}$ pairs are produced via leading order flavour creation or higher order processes such as gluon splitting [2]. In addition, single b quarks can be produced via flavour excitation processes. They can then hadronise with a quark of different flavour with different probabilities, called b fragmentation fractions f_X, where X denotes the flavour of the second quark of the formed B meson in the hedronisation process. Given that they represent probabilities, one must have

$$f_u + f_d + f_s + f_c + f_{baryon} = 1, \tag{1.9}$$

where f_{baryon} represents the probability of the b quark hadronising into a baryon[2]. Complete measurements of b fragmentation fractions do not exist as of yet. Measurements have been performed in an unbiased sample of weakly decaying b hadrons produced at the Z resonance or in $p\overline{p}$ collisions (Table 1.2). B_c decays and doubly heavy baryons were neglected. The constraint of the sum of all the considered fractions being equal to 1 was applied when obtaining these results. The fragmentation fractions cannot be assumed equal in $p\overline{p}$ or pp collisions and in Z decay, since it seems natural that hadronisation might depend on the momentum of the b quark, and the momentum distributions of the b quark in these processes are not the same. LHCb has measured the ratios $f_s/(f_u+f_d)$ and $f_{\Lambda_b}/(f_u+f_d)$ in pp collisions [13], and investigated their dependence on transverse momentum, presenting strong evidence for it in the case of Λ_b hadrons (udb), and verifying a mild dependence for B_s (Figure 1.6). LHCb

and ATLAS have also studied the f_s/f_d dependence on transverse momentum, but the results were inconclusive [14, 15]. If one assumes that because of isospin symmetry, the probability of hadronization of a b quark into a B_s or a B^+ meson will be the same, $f_u = f_d$ and $f_s/(f_u + f_d) = f_s/2f_u$. The independent inclusive (i.e. for the entire range of p_T) measurements of f_s/f_d and $f_s/(f_u + f_d)$ are compatible with this assumption, within uncertainty values.

b hadron	Fraction at Z (%)	Fraction at $p\overline{p}$ (%)
B^+, B^0	41.2 $\pm$ 0.8	34 $\pm$ 2.1
B_s	8.8 $\pm$ 1.3	10.1 $\pm$ 1.5
b baryons	8.9 $\pm$ 1.2	21.8 $\pm$ 4.7

Table 1.2: b fragmentation fractions in $Z \to b\bar{b}$, and in $p\overline{p}$ collisions at $\sqrt{s} = 1.96$ TeV [2].

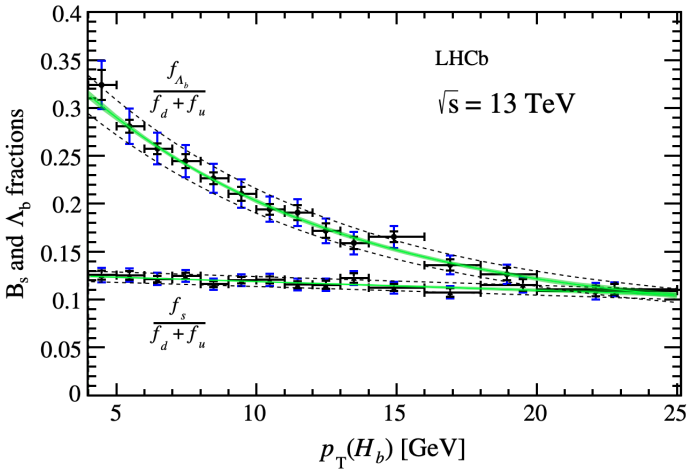

Figure 1.6: Measured $f_s/(f_u + f_d)$ and $f_{\Lambda_b}/(f_u + f_d)$ in pp collisions, at $\sqrt{s} = 13$ TeV [13]. The ratios are presented as a function of the transverse momentum of the b hadron. A strong dependence is verified for $f_{\Lambda_b}/(f_u + f_d)$.

B mesons decay via the weak interaction. The more massive $\bar{b}$ is usually the one that decays, being the other quark called a spectator quark. Since the work of this thesis hopes to shed some light into the QGP medium and that is the realm of the strong interaction, some theoretical aspects of the weak interaction were not delved into in Section 1.1. Nevertheless, it is important to introduce some of its basic aspects allowing a better understanding of the B meson decays pertaining to this work.

The quark eigenstates that undergo weak interaction are not the strongly interacting quark mass eigenstates, but can be instead expressed as admixtures of these latter ones. Mass eigenstates (d, s, b) can be translated into weakly interacting flavour eigenstates (d', s', b'), according to a 3x3 unitary mixing matrix - the Cabibbo-Kobayashi-Maskawa (CKM) matrix [3]. The quark mixing transformation is[2]:

$$\begin{pmatrix} d' \\ s' \\ b \end{pmatrix} = \begin{pmatrix} V_{ud} & V_{us} & V_{ub} \\ V_{cd} & V_{cs} & V_{cb} \\ V_{td} & V_{ts} & V_{tb} \end{pmatrix} \begin{pmatrix} d \\ s \\ b \end{pmatrix}. \tag{1.10}$$

The entries of the CKM matriz represent the strength of nine possible transitions of one flavour

[2]The definition is given in terms of "down-type" quarks, but it could be as easily given in terms of "up-quarks".

to another, being mediated by the charged W boson[3], and suggest how much that interaction will be suppressed. Their experimental magnitudes are [2]:

$$\begin{pmatrix} |V_{ud}| & |V_{us}| & |V_{ub}| \\ |V_{cd}| & |V_{cs}| & |V_{cb}| \\ |V_{td}| & |V_{ts}| & |V_{tb}| \end{pmatrix} = \begin{pmatrix} 0.97417 \pm 0.00021 & 0.2248 \pm 0.0006 & (4.09 \pm 0.39) \times 10^{-3} \\ 0.220 \pm 0.005 & 0.995 \pm 0.016 & (40.5 \pm 1.5) \times 10^{-3} \\ (8.2 \pm 0.6) \times 10^{-3} & (40.0 \pm 2.7) \times 10^{-3} & 1.009 \pm 0.031 \end{pmatrix}. \quad (1.11)$$

By just looking at the entries of the type $|V_{Xb}|$, one can see that $\bar{b} \to \bar{t}W^+$ is favoured. Nevertheless, this is a kinematically forbidden decay due to the large mass of the top. The dominant decay will be then $\bar{b} \to \bar{c}W^+$. The virtual W boson will then materialise into a pair of leptons or quarks which hadronise thereafter. The decays being taken advantage of in this work are two of the latter kind and are represented at leading order in Figure 1.7. The probability of a particle decaying into a specific final state out of all possible final states is referred to as a branching fraction ($\mathcal{B}$). The branching fractions associated to the decays displayed in Figure 1.7 can be found in Table 1.3.

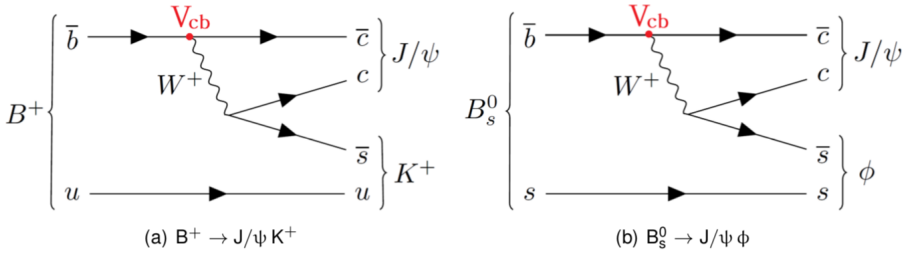

Figure 1.7: Feynman diagrams for the decays relevant for this thesis [16].

Decay	$\mathcal{B}$
$B^+ \to J/\psi\ K^+$	(1.026 ± 0.031) $\times 10^{-3}$
$B_s \to J/\psi\ \phi$	(1.08 ± 0.08)$\times 10^{-3}$
$\phi \to K^+\ K^-$	(4.89±0.50)$\times 10^{-1}$
$J/\psi \to \mu^+\ \mu^-$	(5.961 ± 0.033) $\times 10^{-2}$

Table 1.3: Measured branching fractions used in this thesis [2].

The available decay channels for B mesons are suppressed by the CKM matrix, due to the small values of V_{cb} and V_{ub}. The lifetime of the B meson will be then long enough to produce a measurable displacement between the point of two nucleons' collision and the point of decay. This is an important property of B mesons, that experimenters take advantage of - associated to their decays there is a "displaced vertex".

1.2.2 Production Measurements

We have stated that B meson production measurements can be a window to gaining information about the QGP. In practise, production is quantified by a cross-section. One can perform an inclusive mea-

[3]The Standard Model does forbids the existence of flavour changing neutral currents (FCNC) at the lowest level in perturbation theory.

surement, or if there is the intent of exploring a possible dependence to a specific kinematic variable, a differential measurement can be done. The differential cross section in transverse momentum (p_T), for a given B meson, explored through a specific decay channel, can be computed by [17]:

$$\frac{d\sigma(B)}{dp_T} = \frac{1}{2}\frac{N}{\mathcal{A}\epsilon\mathcal{B}\mathcal{L}\Delta p_T}, \tag{1.12}$$

where N represents the raw yield extracted from data, $\mathcal{A}$ is the detector's acceptance, ϵ the efficiency associated with the event reconstruction and selection, $\mathcal{B}$ is the branching fraction of the decay channel used, $\mathcal{L}$ the integrated luminosity, that is a measurement of the collected data size (in units of inverse area)[4]. The factor of 2 is due to the analysis employing both particle and antiparticles and the result quoted for particle only.

However, the values of the cross sections by themselves are not enough to probe the QGP effects on production. There needs to be an assurance that only so-called final state effects are being measured, i.e. effects that arise through interactions between the produced particles and the generated medium. How, then, can other effects be filtered? Using the cross-sections obtained in pp collisions (vacuum) at the same energies. In the absence of the QGP, nucleus-nucleus collisions behave as superpositions of independent nucleon-nucleon collisions. One can then compute the nuclear modification factor (R_{AA}), a ratio between the production in nucleus-nucleus (σ_{AA}) and pp (σ_{pp}) collisions, scaled by the expected number of binary collisions [5],

$$R_{AA} = \frac{1}{\langle N_{coll}\rangle}\frac{\sigma_{AA}}{\sigma_{pp}}. \tag{1.13}$$

If $R_{AA} < 1$ it is said that the medium caused suppression, and for $R_{AA} > 1$ the opposite effect of enhancement. γ and Z productions have been studied and, as expected, since they don't interact strongly, the results were compatible with $R_{AA} = 1$ [5]. This serves as a check on the validity of the procedure and provides confirmation that AA-vs-pp comparisons of strongly interacting probes give us information about how they are affected by interactions with the nuclear medium[5].

1.2.3 State of the Art

The flavour dependence of energy loss in QGP has been tested by comparing the nuclear modification factors of different hadrons [9]. Figure 1.8 shows the results obtained by CMS as a function of p_T of the hadron. This comparison is performed between: light charged hadrons ($h^{\pm}$), i.e. kaons and pions; prompt D^0, i.e., D^0 not coming from the decays of heavier particles; non-prompt D^0, i.e., D^0 coming from the decays of b hadrons; non-prompt J/ψ, i.e. J/ψ coming from b hadron decays; and $B^{\pm}$ mesons. For low p_T, light charged hadrons are more suppressed than open heavy flavour hadrons. In addition, at intermediate p_T, the nuclear modification factor of non-prompt J/ψ is significantly higher than for D^0, supporting a bottom-charm energy loss hierarchy. That difference is reinforced when one is reminded that non-prompt J/ψ does not carry the full p_T of the B meson that generated it, so a shift for slightly higher p_T should be accounted for when doing the comparison. At high p_T there is a degeneracy of the

[4] Defined in Chapter 2.

[5] The LHC provides in addition p-Pb collisions, allowing to probe so called cold nuclear matter effects

R_{AA}'s. This is expected, since the energy-to-mass ratio becomes large, and so the mass effects should cease. It is also seen that the degenerecy of light-charm hadrons R_{AA} happens at around 10 GeV/c, and bottom R_{AA} further degenerates at around 25 GeV/c.

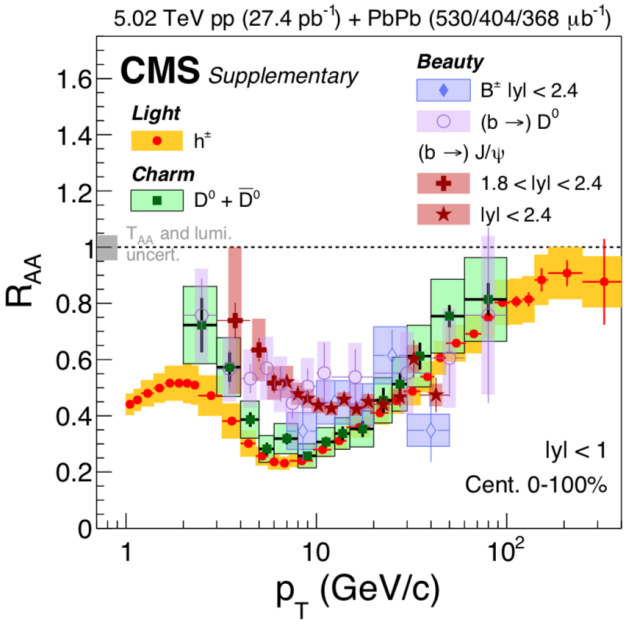

Figure 1.8: Nuclear modification factors of different hadrons, measured in PbPb collisions at $\sqrt{s}$ =5.02 TeV, as a function of transverse momentum. Results obtained by the CMS Collaboration [9].

Also the enhancement of strange heavy flavour mesons relative to their non-strange counterparts, has been probed in heavy ion collisions [9]. D_s and D^0 production has been measured in PbPb collisions at the LHC and in AuAu collisions at RHIC. The D_s and D^0 production ratios for both experiments can be found in Figure 1.9 (a), as a function of transverse momentum. Also showed is the same ratio measured in pp collisions at the LHC. Its behaviour is well reproduced by Monte Carlo simulation (PYTHIA8). A significant enhancement of this ratio is found in the QGP medium.

Using 2015 data from PbPb collisions at 5.02 TeV, B_s and B^+ production results have been recently published by CMS [18**?**]. The nuclear modification factors obtained after normalisation with pp production can be found in Figure 1.10. Their ratio was also presented (Figure 1.9-b). The data seems to suggest an enhancement relative to the B^+ case. However the B_s signal is not sufficiently significant in the dataset analised, and there are large statistical uncertainties affecting the comparison. A more precise measurement must be performed offering more insight on hadronisation in the bottom sector.

In November 2018, a larger dataset was collected by CMS with the LHC running for PbPb collisions. The data sample is larger by a factor of 3, comparatively to the one used for the analysis that yielded Figure 1.9-b. The larger dataset will be employed for this analysis. B mesons are novel probes of the QGP, since only in the last few years has their exclusive measurement been possible in this medium. This means that one can fully reconstruct a specific B decay channel, reconstructing its identity and kinematics. The first observation of the B_s signal in PbPb collisions will result in a robust quantification of the competing medium effects of suppression and enhancement, relative to the B^+.

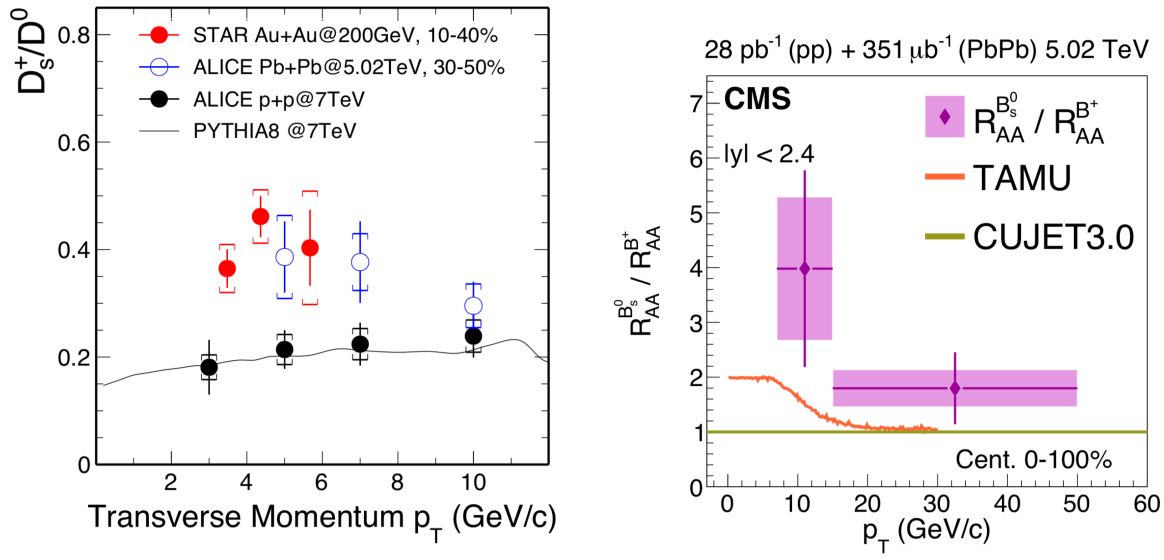

(a) D_s/D^0 production ratios measured in Au-Au collisions by STAR, PbPb and pp collisions by ALICE.

(b) B_s and B^+ nuclear modification factor ratios, in PbPb collisions at CMS.

Figure 1.9: Measurements of strange heavy flavour meson production relative to their non-strange counterparts, as a function of transverse momentum [9].

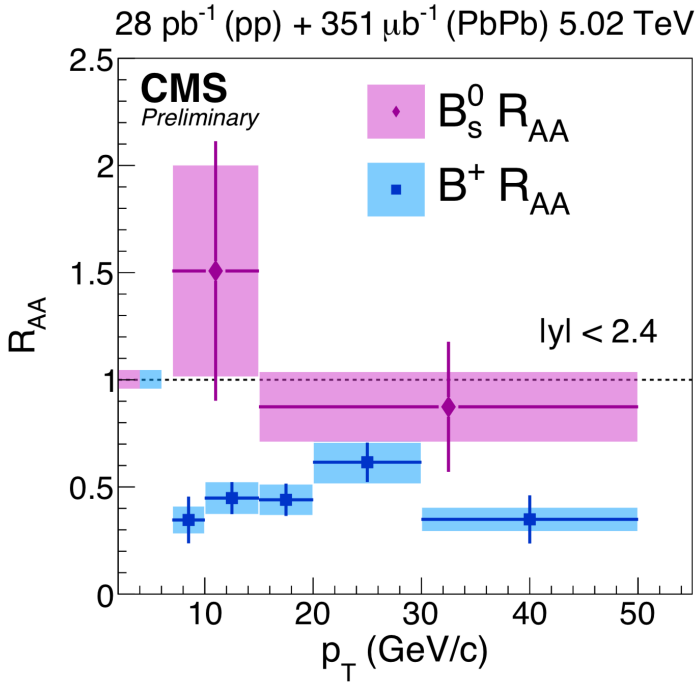

Figure 1.10: B_s nuclear modification factor measured in two p_T intervals, in the range 7-50 GeV/c (pink data points). This measurement was performed with the smaller 2015 dataset, with an integrated luminosity of 351 μb^{-1} [18]. Overlaid is also the B^+ nuclear modification obtained with the same dataset (blue data points). The rectangular boxes, in both cases, represent the systematic uncertainties.

1.3 Thesis Outline

This work presents B_s and B^+ production measurements, performed using data collected by CMS in PbPb collisions at the LHC. It was done at *Laboratório de Instrumentação e Física Experimental de*

Partículas (LIP), and in collaboration with the Heavy Ion Group from Massachusetts Institute of Technology (MIT). The next chapter contains a brief description of the LHC and the CMS experiment, focusing on the subdetectors relevant for this work. Chapter 3 details which datasets and Monte Carlo samples are employed in this analysis, as well as, which was the selection applied from there on. The following chapters detail how the most important ingredients of the analysis were obtained: Chapter 4 describes the signal yield extraction (raw production) and Chapter 5 describes the determination of acceptances and efficiencies, correction factors to be applied to the raw yield. This computation is done using Monte Carlo (MC) samples. Chapter 6 compares the data and MC samples, through two methods (sideband subtraction and SPlot), in order to calculate the deviations to be propagated as systematic uncertainties. Chapter 7 discusses all the systematic uncertainties that were considered in the final result. Finally, cross sections of B_s and B^+ for PbPb collisions at 5.02 TeV are presented in Chapter 8. The ratio between them is further computed allowing the study of the QGP medium effects, and offering insight on B meson hadronisation. Using published CMS results of B_s production cross section in pp collisions, the B_s nuclear modification factor is determined.

Chapter 2

Experimental Framework

The work presented in this thesis uses data collected by the Compact Muon Solenoid (CMS), one of the general purpose experiments at the Large Hadron Collider (LHC). This chapter will introduce this experimental setup, as well as some of the key quantities in any particle physics analysis.

2.1 The Large Hadron Collider

The Large Hadron Collider was built at the European Organisation for Nuclear Research (CERN), near Geneva [19]. It provides both proton and lead nuclei beams in a 27 km circular tunnel 100 m underground, which previously hosted the Large Electron Positron Collider (LEP). It was designed to accelerate protons/nuclei up to very high energies and bring protons/nucleons to collide as often as possible for long times without interruption, allowing the study of the SM and beyond.

Protons/nuclei go through a series of accelerators before being injected into the LHC in the form of two counter-rotating beams, where they are further accelerated to their collision energies. The designed maximum center of mass energy for pp collisions is $\sqrt{s_{pp}} = 14$ TeV and for PbPb is $\sqrt{s_{NN}} = 5.5$ TeV. The proton beam is produced in Linac2, where electrons are stripped of hydrogen atoms, and sequentially injected into the Proton Synchrotron Booster, Proton Synchrotron (PS), Super Proton Synchrotron (SPS), and finally to the LHC ring. In the case of ions, the beam is created from a source of vaporized lead. They enter Linac3 for first acceleration, being then collected and further accelerated by the Low Energy Ion Ring (LEIR), PS and SPS. A schematic of the accelerators mentioned can be found in Figure 2.1.

Electromagnetic fields are used to accelerate and steer the particles. Acceleration is achieved through metallic chambers designed to sustain an electromagnetic field, called radiofrequency (RF) cavities. One can imagine beads on a string, the beads being the RF cavities and the string being the beam pipe, through which the particles travel in vacuum. An RF power generator supplies an electromagnetic field. The cavity's shape was designed to achieve resonance and the build up in intensity of the electromagnetic waves. Consequently, charged particles passing through it, "feel" the overall force and direction of the electromagnetic field, which transfers energy, and propels them forward. The field

in a RF cavity oscillates at 400 MHz, so the timing of the arrival of the particles is important. An ideally timed particle, arriving with the right energy will not be accelerated when passing a cavity. Meanwhile, particles with slightly different energies arriving earlier or later will be decelerated or accelerated. This sorts the beam into packets of the same energy, called "bunches". In the case of protons, the LHC is designed to have 2808 bunches crossing each other every 25 ns, each one with more than 10^{11} protons. This means a bunch collision rate of 40 MHz, producing almost 1 billion collisions per second. These parameters define the instantaneous luminosity ($\mathcal{L}_{inst}$). It is defined as the proportionality factor between the rate of events of a certain process produced in the collisions, and the respective cross section:

$$R = \mathcal{L}_{inst}\sigma. \tag{2.1}$$

It can be calculated through [20]:

$$\mathcal{L}_{inst} = f\frac{N_1 N_2 n_b}{4\pi\sigma_x\sigma_y}, \tag{2.2}$$

where f is the bunch crossing frequency, N_1 and N_2 are the number of particles in each bunch, n_b is the number of bunches and σ_x and σ_y are the transverse dimensions of the beam. To characterise the amount of data collected by a collider experiment, the integrated luminosity in time is used. The cumulated luminosity recorded by CMS in the PbPb run of 2018, used in this work is shown in Figure 2.2. The total number of events observed for a given reaction is

$$N = \sigma\int \mathcal{L}_{inst}dt. \tag{2.3}$$

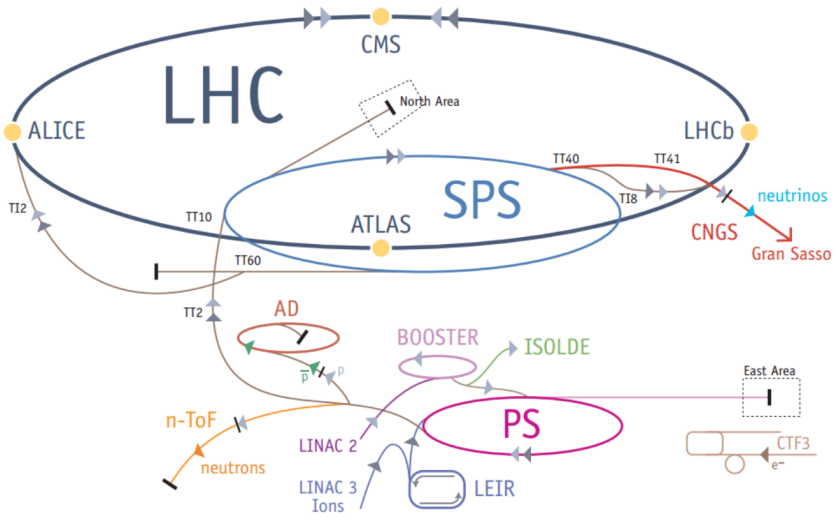

Figure 2.1: Schematic of the accelerator sequence at the LHC.

The beams are kept inside the LHC rings by superconducting dipole magnets, that originate a magnetic field of around 8.3 T. They are cooled to 1.9 K by a liquid helium cryogenic system. Quadrupole magnets focus the beam in interaction points (IP), where the counter-rotating beams are brought to collision. Four main detectors are located in these points (Figure 2.1): the Compact Muon Solenoid (CMS) and A Toroidal LHC ApparatuS (ATLAS), two general purpose experiments; A Large Ion Collider Exper-

iment (ALICE), optimised to study heavy ion collisions; and The Large Hadron Collider beauty (LHCb), dedicated to the study of bottom particles.

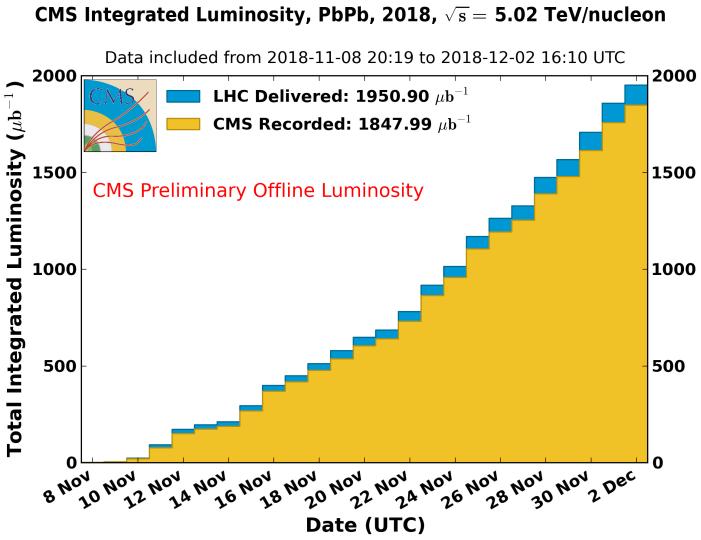

Figure 2.2: The integrated luminosity delivered by the LHC, and measured by CMS, for lead-lead collisions during 2018 [21].

2.2 Compact Muon Solenoid

CMS [22] was designed mainly to search for and study heavy particles. Since those particles would be able to decay into b quarks, the ability to detect and perform measurements involving b-hadrons was taken into account in the conception of this detector. Its central feature is a 13 m long, 6 diameter superconducting solenoid, that creates a magnetic field of around 3.8 T. It is composed of subdetectors that are arranged cylindrically around the beam pipe. In Figure 2.3 a transverse slice through CMS is displayed, showing its layers. From the beam to outside one finds: the silicon tracker, electromagnetic and hadron calorimeters, the solenoid, and the muon chambers. Different particles will deposit their energy at different parts of the detector. Photons and electrons will stop at the electromagnetic calorimeter, and hadrons will stop in the hadron calorimeter. Except for neutrinos that are not detected, only muons get to the last layer, because they do not interact strongly and are too massive to emit a substantial fraction of energy through electromagnetic radiation, being able to penetrate dense materials, like steel. In the rest of this chapter only the most relevant sub-detectors will be highlighted and explained in more detail.

2.2.1 CMS Coordinate System and Parametrization

The coordinate system of CMS originates at the center of the detector. The z axis points along the counter-clockwise beam direction: Following the right-hand rule, the x axis points inward to the LHC ring center, and the y axis points vertically upwards. In spherical coordinates, the azimuthal angle $\phi \in [-\pi, \pi]$ is measured from the x axis in the xy plane, while the polar angle $\theta \in [0, \pi]$ is measured from the z axis. The radial coordinate is denoted by $R = \sqrt{x^2 + y^2}$.

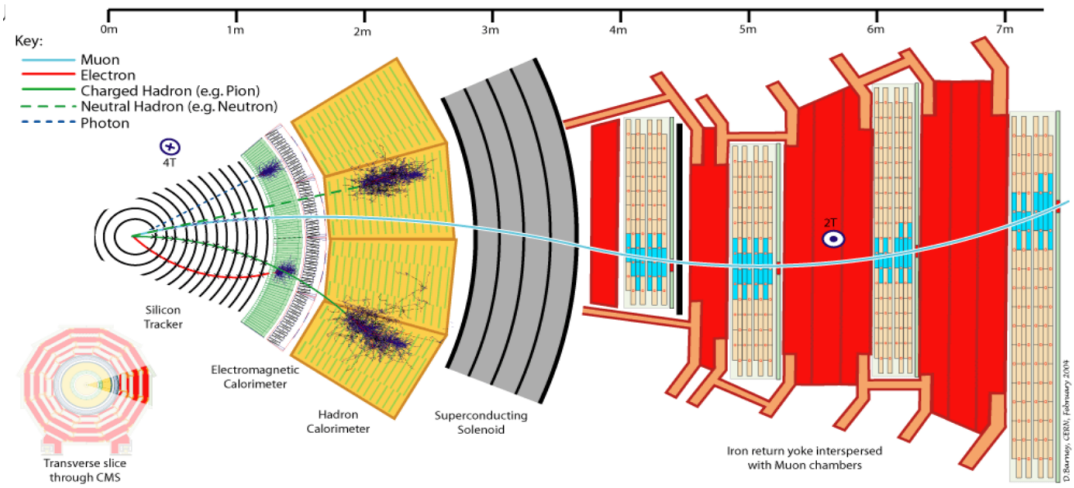

Figure 2.3: Transverse view of the CMS detector, showing its different layers.

A quantity of particular importance for this thesis, and in general for experimental particle physics is the transverse momentum p_T, defined as

$$p_T = \sqrt{p_x^2 + p_y^2}. \tag{2.4}$$

It is invariant with respect to Lorentz boosts along z and can be more precisely measured than the total momentum, given the absence of detectors close to the z axis. Another quantity usually used in accelerator physics is the rapidity (y) [20]:

$$y = \frac{1}{2} \ln \left(\frac{E + p_z}{E - p_z} \right). \tag{2.5}$$

Interpreting the expression, one can conclude that if a particle is directed essentially in the transverse xy plane, its rapidity will be close to 0, while if it is in the beam direction, the rapidity will go to infinity. Rapidity differences are invariant under boosting in the z direction. This quantity can prove hard to measure precisely, since it needs both the particle energy and the momentum along z. Another quantity, easier to measure, is the pseudorapidity,

$$\eta = -\ln \left(\tan \frac{\theta}{2} \right) = \frac{1}{2} \ln \left(\frac{|p| + p_z}{|p| - p_z} \right). \tag{2.6}$$

For relativistic particles, $\eta \approx y$. Conventionally, the region of the detector of $|\eta| < 1.2$ is called the barrel and the region of $1.2 < |\eta| < 2.4$ is called the endcap. In Figure 2.4 one can find a z-R transverse section of the CMS detector, with the pseudorapidity denoted for different θ angles.

2.2.2 Silicon Tracker

The tracking system is situated at the innermost part of CMS. Its goal is to provide precise measurements of trajectories of charged particles with $|\eta| < 2.5$. It consists of two sub-systems, the silicon pixels,

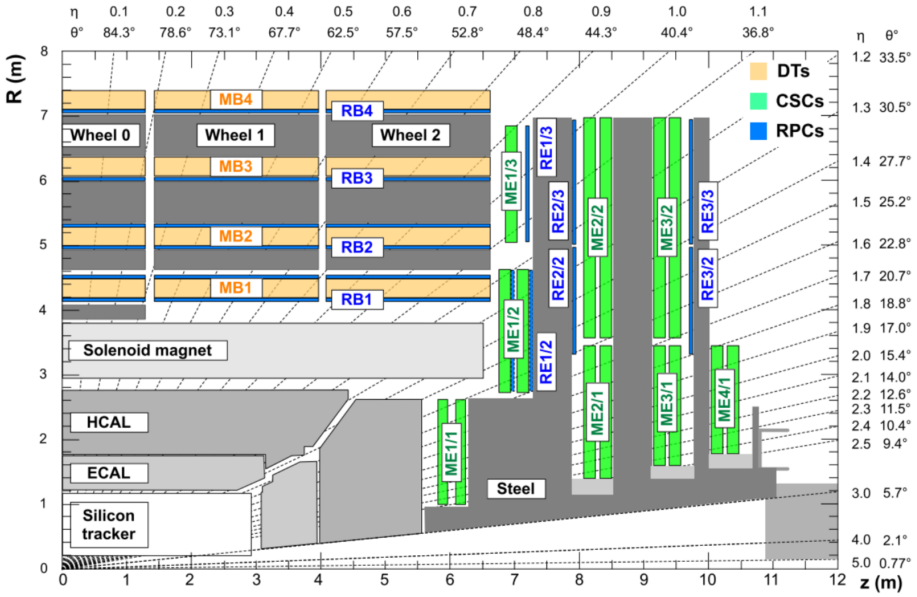

Figure 2.4: z-R transverse section of the CMS detector [23].

located closer to the beam, and the silicon strips, with 75 million separate electronic read-out channels. The tracking is conceptually simple. When a charged particle crosses the tracker, electrons will be knocked-out of the silicon atoms, creating electron-hole pairs. An electric current is used to collect these charges as a small electric signal, that is then amplified. In this way, through ”hits” of the charged particles, their path can be reconstructed, and their properties measured. CMS's silicon tracker has a very good spacial resolution: about 10 μm in the radial direction and 20 μm in the z direction [24]. For the purpose of this thesis, muons and kaons constitute the final states, and their reconstruction is possible thanks to this detector layer. It is important to note that CMS does not employ a dedicated hadron identification detector, and cannot straightforwardly distinguish between charged hadrons like kaons, pions and protons. On the other hand, muons can be easily identified, given that there is also information from the muon chambers. The tracker is also crucial in the precise measurement of the displaced vertex of the B meson[1].

2.2.3 Hadron Calorimeter

The hadron calorimeter is installed between the electromagnetic calorimeter and the superconducting solenoid (Figure 2.3) and it is responsible for hadron energy measurements. It is a sampling calorimeter, which means that it is composed by layers of scintillating active material (in this case, plastic scintillating tiles), interspersed by layers of absorber material (brass). When a hadron crosses the absorbers, it interacts with the brass material and generates showers of secondary particles. These showers activate the scintillators that emit light. The photons are then transmitted to multi-channel hybrid photodiodes, designed to operate under a high intensity magnetic field. The light signal emitted is proportional to the interacting particle's energy. The hadron calorimetry system is organised in an inner barrel region

[1] As already mentioned in Chapter 1, between production and decay, the B meson travels a measurable distance in the detector.

(HB), endcap regions (HE), two forward calorimeters (HF) and an outer detector (HO), placed outside of the solenoid, sampling the energy of penetrating hadron showers (Figure 2.5). The HF detector has a particular importance in analysis of PbPb collisions due to its role in measuring the centrality.

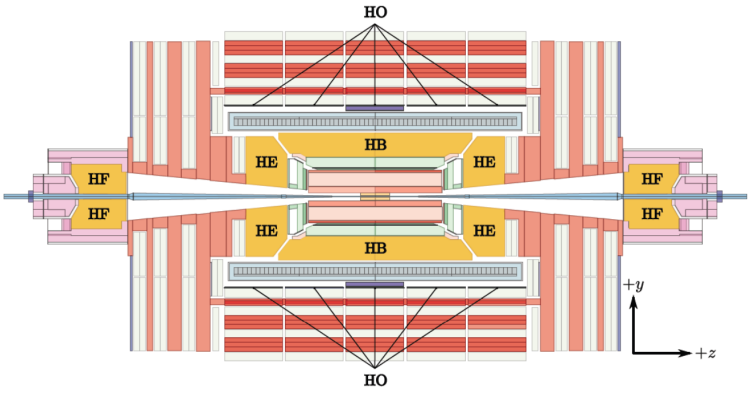

Figure 2.5: A view of the CMS detector in y-z projection with specified components of the hadronic calorimeter.

As already explained in the previous chapter, the centrality of a collision quantifies the extent of the overlap between the two colliding nuclei. The smaller the transverse distance between the two centers (the impact parameter b), the more central the collision. Assuming a monotonic relation between the impact parameter and the amount of energy originated in a collision, the larger the overlap between the nuclei (and the smaller the b), the more energy is expected to be deposited in the hadron forward calorimeters ($3 < |\eta| < 5$). So, experimentally, one uses the distribution of the total transverse energy deposited in the HF, to divide an event sample into centrality classes. For instance, the top 10% most energy deposited corresponds to a centrality class of 0–10% (Figure 2.6).

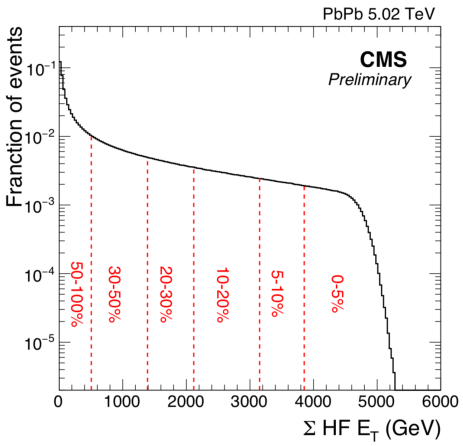

Figure 2.6: Distribution of the sum of HF measured total transverse energy, and the corresponding division of the event sample in centrality classes [25].

2.2.4 Muon Stations

The muon stations are located in the outermost part of the detector, embedded between iron "return yoke" layers (in red in Figure 2.3), that confine the magnetic field. They are used for muon identification, momentum measurement and triggering. Only muons (and neutrinos) are able to penetrate all the components located inside the solenoid, and go through multiple iron layers without interacting. The good muon identification of CMS is then achieved by reconstructing its path by fitting a curve to hits in the muon stations together with the hits produced in the tracker. The muon system is composed by three types of gaseous detectors [26]:

- drift tubes (DT) in the barrel region, seen in yellow in Figure 2.4;
- cathode strip chambers (CSC) in the endcap region, seen in green in Figure 2.4;
- resistive plate chambers (RPC), marked in blue in Figure 2.4.

Their fundamental functioning is the same. With the passage of a muon, electrons are liberated from the gas atoms, producing an electric signal that allows the tracking of the muons.

2.2.5 Trigger System

Only a small fraction of the collisions that occur at the interaction point will contain physics processes of interest to each analysis. Furthermore, the storage space and rate of data transfer required make it impossible to keep a record of all the collision events. As a result, a trigger system is crucial to select only the interesting fraction of the events. The CMS trigger system is divided into two decision levels: level one (L1) trigger, and high-level trigger (HLT) [27]. Together they are designed to reduce the amount of collected data by a factor of 10^6.

The L1 trigger is entirely hardware based and it is used to make a first, fast decision ($\sim$ 4 μs). The decisions are based on the quality of object candidates like muons, electrons, photons or jets, that are built from the energy deposits in the calorimeters and the hits in the muon stations. In the case of the trigger employed for this analysis only events that triggered the individual sub-systems of the muon detector, are considered. Regional track reconstruction is performed gathering information from the individual sub-systems, for the highest quality candidates (depending on criteria like object p_T). In parallel, high energy deposits are found in the calorimeters, and the highest quality candidates are chosen (following criteria like isolation). In the end, a Global Trigger incorporates the information from this track reconstruction algorithm and the and the calorimeter trigger.

Events retained by the L1 Trigger are further processed by the HLT, a software trigger that rejects the surviving events by a factor of 10^3. It makes use of a processor farm with thousands of commercial processors, that further reconstructs the physics objects and applies selection criteria. The HLT is the first stage of the triggering process in which the tracker information is used. The HLT is configured to trigger events according to a list of algorithms that employ different selection strategies (HLT paths). Different HLT paths will be more suitable to retain the desired events (the so called signal events),

depending on the physics analysis to be performed. The retained events are classified into different primary datasets (PDs) according to the passed HLT path. These PDs are used for offline reconstruction and analysis. Events used in this analysis were collected with triggers requiring the presence of two independent muon candidates in the muon detector with no explicit muon p_T or rapidity threshold.

Chapter 3

Data, MC Samples and Selection

In the previous chapter, the ways in which the collected data is filtered through triggers and grouped in primary datasets to be used in physics analyses was summarised. Nevertheless, the data samples are not enough to arrive at correct measurements of B meson production. One needs to be able to calculate the analysis efficiency[1] and for that Monte Carlo (MC) simulation is key. In this chapter the datasets and MC samples used in this work are presented. Furthermore, one must still go from the final state information recorded in the datasets to B meson candidates. A description of this reconstruction is thus here documented. Finally, the analysis selection applied is detailed.

3.1 Datasets

This analysis was performed using the data from the 2018 PbPb run, with a center-of-mass energy of $\sqrt{s_{NN}} = 5.02$ TeV, and corresponding to a total integrated luminosity of 1.5 nb^{-1}. Only data events that fired the `HLT_HIL3Mu0NHitQ10_L2Mu0_MAXdR3p5_M1to5_v1` HLT path are considered. It requires the presence of two muon candidates (dimuon). No selection is made on momentum (including transverse momentum) or pseudorapidity. This path takes advantage of two HLT sub-levels, the L2 and L3 triggers. The L2 trigger takes the events that passed the L1 trigger, and further filters them, still just employing information from the muon stations and the calorimeter. The L3 trigger uses information from the entire detector, including the silicon tracker. So, for a dimuon to fire the trigger chosen for this analysis, one of the muons needs to pass an L2 single muon filter and the second dimuon needs to pass an L3 single muon trigger, plus the dimuon itself needs to pass a third filter that has a mass cut. There are in total 24 million events kept by this path. This HLT path was saved in two primary datasets (PD). The full name of the used datasets can be found in Table 3.1.

[1] Be reminded of the cross section expression presented in Chapter 1.

Table 3.1: List of PbPb HLT datasets and triggers with the corresponding integrated luminosities used in the analysis.

Primary dataset	Trigger	Luminosity
/HIDoubleMuonPsiPeri/HIRun2018A-04Apr2019-v1/AOD	HLT_HIL3Mu0NHitQ10_L2Mu0_MAXdR3p5_M1to5_v1	484 μb^{-1}
/HIDoubleMuon/HIRun2018A-04Apr2019-v1/AOD	HLT_HIL3Mu0NHitQ10_L2Mu0_MAXdR3p5_M1to5_v1	1019 μb^{-1}
Combined All		1.5 nb^{-1}

3.2 Monte Carlo Samples

Monte Carlo simulations are key for particle physics analysis, since they allow access to the correspondence between a physics process and detector signatures. In this work they are employed in the computation of efficiencies, the estimation of systematic uncertainties and the extraction of the signal shape in the process of yield calculation. Different generators can be used to produce the final state particles, modelling the processes of interest. In this case, the commonly used PYTHIA8 [28] was used to generate inclusive (all quark, anti-quark, as well as gluon initiated) QCD processes at a center of mass energy of 5.02 TeV. Only signal events with at least one B meson candidate were kept in the samples. Through the EVTGEN package [29], these mesons were forced to decay through the decay channels introduced in Chapter 1. The B mesons phase space was restricted to $p_T > 5.0$ GeV and $|\eta| < 2.4$. Final state radiation is generated using PHOTOS [30]. Since a full heavy ion event generator is not yet available, underlying events of heavy ion collisions and the beauty probes are generated separately, with HYDJET [31]. The generated signal events were embedded into this PbPb background.

B mesons with a higher p_T will have a lower probability of being produced in a collision. This translates into a falling p_T spectrum for the B mesons generated in simulation, and a large fraction of low p_T mesons relative to high p_T mesons present in the same MC simulation. Therefore, in order to increase the generation efficiency of high p_T B mesons, several MC generations were performed, with the only difference being the lower bound for the momentum transfer between the two colliding nucleons ("p_T hat"). Around fifty thousand events were generated in simulations with 5 different lower bounds - 0, 5, 15, 30, 50 GeV/c.

3.3 B meson Reconstruction and Baseline Selection

The B meson reconstruction procedure takes advantage of the long decay length of these particles, that produce what is called a displaced vertex in the CMS detector. This displacement exists between the point where the nucleon collision occurred (Primary Vertex) and the point where the B mesons decayed (Secondary Vertex). The mesons were reconstructed in the final states $B^+ \to J/\psi K^+$ and $B_s \to J/\psi$, with $J/\psi \to \mu^+\mu^-$ and $\phi \to K^+K^-$. Before reconstruction, one has access to final state objects: in this analysis 2 muons, and 1 kaon, in the case of the B^+, or 2 kaons, in the case of the B_s. From now on the term "track" will be used to characterise the kaons, since they leave a trail only on the silicon tracker. For each event, combinations of tracks and muons are then fitted together, reconstructing one,

or more[2] secondary vertices, displaced from the corresponding primary vertices. Figure 3.1 shows the decay scheme for the B^+ meson, with the final state particles, PV and SV represented.

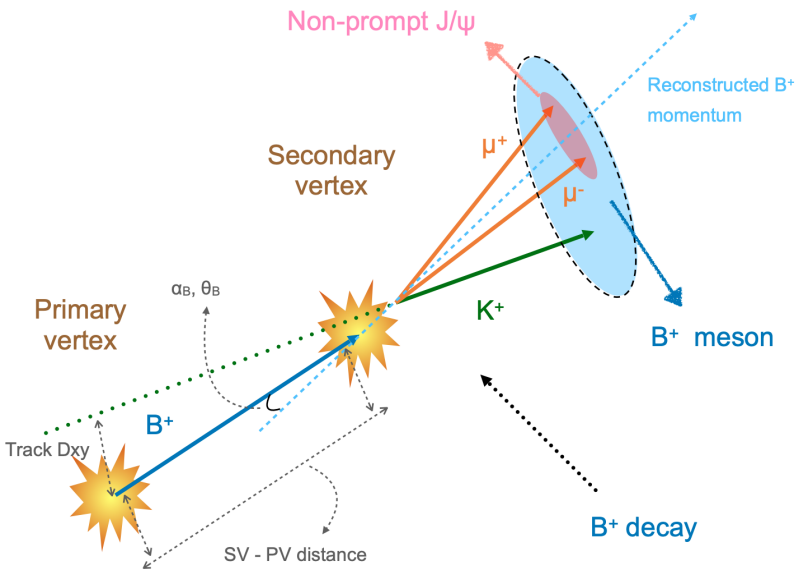

Figure 3.1: A schematic of the B^+ meson decay and the definitions of variables included in the BDT training [32].

A flowchart representing the B^+ meson reconstruction workflow is found in Figure 3.3. For B^+ the workflow is analogous, the only difference being the fact that B_s has an extra final state track. Going through this workflow, first there are some basic selections applied to both muons and tracks. Starting with the muons, selection criteria are applied to ensure a high signal to noise ratio (quality cuts):

- *isGlobalMuon* and *isTrackerMuon* - a global muon was successfully reconstructed by matching muon trajectories in the muon chambers to tracks left in the silicon tracker, in an "outside-in" approach, while a tracker muon was successfully reconstructed with an "inside-out" approach;
- *isGoodMuon* > 0 - tracker track matched with at least one muon segment (in any station) in both x and y coordinates;
- transverse impact parameter[3] $\mathrm{D_{xy}} < 0.3$ cm;
- longitudinal impact parameter $\mathrm{D_z} < 20$ cm;
- *nPixWMea* > 0 and *nTrkWMea* > 5 - *nPixWMea* and *nTrkWMea* are the number of pixel layers and strips, with valid hits, crossed by a single muon track.

Some requirements are also made to the phase space of the muons. These are needed because of the design and positioning of the muon chambers in the CMS detector, that define the detector muon acceptance. It is observed that only muons with a minimum p_T as function of η are able to produce enough hits in the muon chambers, for the muon to be well reconstructed (Figure 3.2). Muons with low

[2]There can be more than one B meson candidate for each event!
[3]Distance of closest approach between the line of motion of a particle and the nucleon-nucleon collision vertex.

p_T will get lost in the detector before reaching the muon stations. The acceptance selection thus applied to the muon candidates is:

$$\begin{aligned} p_T^\mu &> 3.5 \text{ GeV/c} && \text{for } |\eta^\mu| < 1.2 \\ p_T^\mu &> (5.47 - 1.89 \times |\eta^\mu|) \text{ GeV/c} && \text{for } 1.2 \leq |\eta^\mu| < 2.1 \\ p_T^\mu &> 1.5 \text{ GeV/c} && \text{for } 2.1 \leq |\eta^\mu| < 2.4. \end{aligned} \tag{3.1}$$

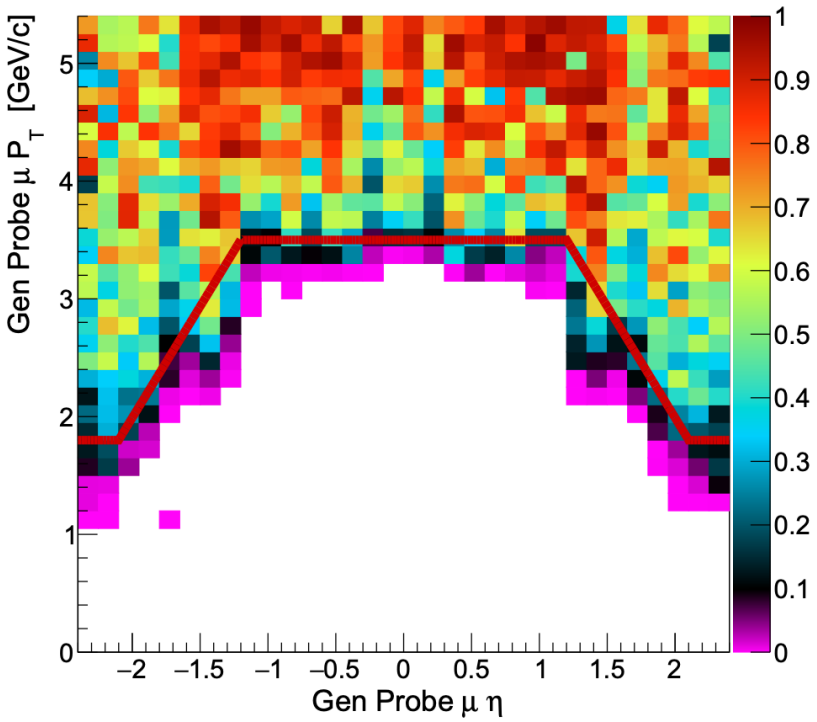

Figure 3.2: Muon p_T and η 2D distribution in Monte Carlo simulation. The red line represents the single muon acceptance cuts applied [33].

This single muon selection is chosen in order to guarantee a reasonable (above $\approx 10\%$) reconstruction and trigger efficiency for all the selected muons [33].

In the case of hadron tracks, the following criteria were required:

- they must be of *highPurity* [24], rejecting badly reconstructed tracks;
- $|\eta|$ <2.4;
- Total number of valid hits on the silicon tracker (pixel and strip layers) > 10;
- $p_T >$ 1.0 GeV/c and $\frac{\Delta p_T}{p_T} < 0.1$;
- χ^2 probability normalized by number of degrees of freedom and sum of the numbers of Pixel and Strip Layer hit > 0.18.

Muons of opposite charge are fitted together, through a Kinematic Constraint Vertex Fitter [34], based in a least means squared minimisation, reconstructing a J/ψ candidate. In the same way, ϕ candidates

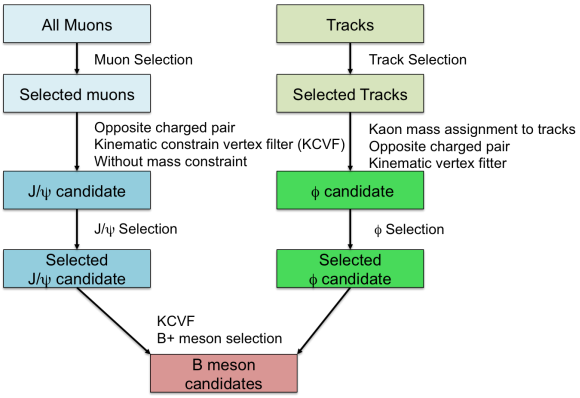

Figure 3.3: Flowchart of the B_s meson reconstruction workflow [32].

are reconstructed through a vertexing procedure to the tracks, in the case of the B_s. In addition to single muon and track quality selections the following selections are applied to the muon and track pairs (in the case of B_s):

- dimuon invariant mass within 0.15 GeV/c^2 from the J/ψ PDG mass [2];
- track pair invariant mass within 0.015 GeV/c^2 around the ϕ meson PDG mass [2];
- probability of the two muon tracks to originate from the same decay vertex $>$ 1%;
- probability of the two tracks to originate from the same decay vertex $>$ 0.05%.

Finally, the B_s (B^+) candidates are built by combining the J/ψ candidates with the ϕ (K^+) candidates.

3.4 Optimised Selection

After reconstruction, the data and MC samples will contain information relative to the B candidates found for each event. One refers to these objects as candidates, since they were reconstructed as combinations of tracks and muons with no certainty of having been originated through the decay of a B meson. Some of these candidates may be the random combination of tracks and muons. These random combinations constitute what is called background, and the ones that truly come from B mesons are what we call signal. The baseline selection described in the previous section rejects some of the background candidates (particularly the cuts in the dimuon and track pair invariant masses), but is not enough to truly distinguish signal from background, *i.e.* to observe a peak in the invariant mass spectrum of the B candidates in data. A multivariate analysis (MVA) was thus conducted in order to devise a B candidate selection to better separate signal from background.

In a general sense, MVA is a set of techniques that exploit multiple variables at the same time, achieving vastly superior performances with respect to using selection based on single variables (what are called rectangular cuts). MVA discriminators, usually under the form of Boosted Decision Trees (BDTs) and Neural Networks (NNs), are widely used in particle physics analyses. In this work, the optimised selection was obtained through a BDT method, using the Toolkit for Multivariate Data Analysis

with Root (TMVA) [35]. A decision tree recursively splits data by checking requirements on its features. A BDT is an ensemble of decision trees [36]. If a candidate was misclassified by the first decision tree, that event will be assigned a higher weight. The second tree is built using the new weights that determine how important they are during the classification process. This is done successively as many times as the number of trees chosen by the analyser[4]. A BDT must be "trained" on known signal and background candidates (the variables), and the input variables must have discriminating power, meaning that they need to capture differences between signal and background candidates.

In the case of the training used by this work, the collection of signal events in training comes from the MC samples, where it is known if candidates are signal or background. On the other hand, the reconstructed mass of the B mesons in data was used to identify background candidates. This is possible since the B meson mass is known (and presented in Chapter 1), and the resolution of the signal distribution can be checked in Monte Carlo, so one can determine the signal region. Outside of that region, candidates will surely be background. This region is usually called sideband region. Candidates from the sideband region were then the ones used for the training. The total collection of known background and signal candidates is divided in two sub-samples, so that one can be used in testing the constructed discriminator, before its application in the analysis. It is important to refer that the training was performed independently for different ranges of the B meson transverse momentum.

Different kinematic and topological variables were used as input variables for the training. When choosing the input variables one needs to look for features that will help to discriminate signal from background. Since the B meson reconstruction is based on a vertexing procedure where tracks and muons were fitted together, the χ^2 of the fit naturally serves as a good feature. The distance between the primary and secondary vertices will also be helpful, given the characteristically large decay length of B mesons. The whole decay system is expected to be boosted. Opening angles between the momentum and the displacement of the B mesons are expected to be smaller for signal candidates. Kinematic properties of the final state particles were also considered. Listing all the input variables for the optimisation associated to each B meson, and starting with the B^+ there are six variables taken advantage of:

- Normalized decay length, meaning the distance between primary and secondary vertices normalized by its uncertainty (dls3D);
- The angle between B^+ meson displacement and B^+ meson momentum in 3D (Balpha);
- K^+ transverse momentum (Btrk1Pt);
- The χ^2 probability of the secondary decay vertex fitting (Bchi2cl);
- The absolute value of the K^+ pseudorapidity (|Btrk1Eta|);
- Transverse distance between track and the primary vertex normalized by its uncertainty (Btrk1Dxysig).

[4]More trees will allow the construction of a better classifier, but one must avoid overtraining. That would constitute a perfect separation for the sample of events used during training that could not be replicated to a testing sample.

In the case of B_s, the input variables used, with signal and background distributions shown in Figure 3.4 (for B_s p_T in the range of 20-50 GeV/c) were:

- The transverse momentum of the K^+ and K^- track (Btrk1Pt and Btrk2Pt);
- The transverse distance between the K^+ and K^- track to primary vertex, divided by its error (Trk1DCAxy and Trk2DCAxy);
- The longitudinal distance between the K^+ and K^- track to primary vertex, divided by its error (Trk1DCAz and Trk2DCAz);
- The absolute difference between the invariant mass of the track pair (which form a ϕ meson candidate) and PDG mass of a ϕ meson (MassDis);
- The distance between primary and B_s vertex normalized by its uncertainty (dls);
- The angle between B_s meson displacement and B_s meson momentum (Balpha);
- The cosine value of the angle between B_s meson displacement and B_s meson momentum in the transverse direction (cos(Bdtheta));
- The χ^2 probability of the secondary decay vertex fitting (Bchi2cl).

During the training, each decision tree will place different selection requirements ("cuts") on these input variables. Each candidate will be classified as either signal (being assigned a score of 1) or background (being assigned a score of -1), for each tree. The final BDT score combines the predictions of each tree. A higher value means that more individual trees predicted that the candidate is signal, and so the candidate is "signal-like". A lower BDT score translates into a candidate being "background-like". So in the end, the optimised cuts will not be placed on individual variables but on the BDT score obtained through the application of our discriminant to each candidate of the data sample.

The goal of the optimisation process is to reject background while keeping signal candidates. A decision must be made on what is the best value to place the cut on the BDT score. This optimal working point was found by scanning the cut to the BDT and checking which one maximises the figure of merit:

$$\frac{S}{\sqrt{S+B}}, \tag{3.2}$$

where S is the number of signal candidates in signal region after applying a given cut to the BDT, while B is the number of background candidates in the signal region after applying that same cut. These values can be estimated from the number of signal and background candidates in the signal region before applying optimised selection (S' and B') and the signal and background efficiencies, $i.e.$, the ratio of signal and background events that are kept using the discriminator. As an example, the obtained efficiencies during the training performed for B_s are shown as a function of the BDT score cut applied, for the p_T range of 20-50 GeV/c, in Figure 3.5 (a). S' is estimated by multiplying the expected theoretical yield (obtained using FONLL [37]) by the efficiency of the baseline selection listed in the previous section,

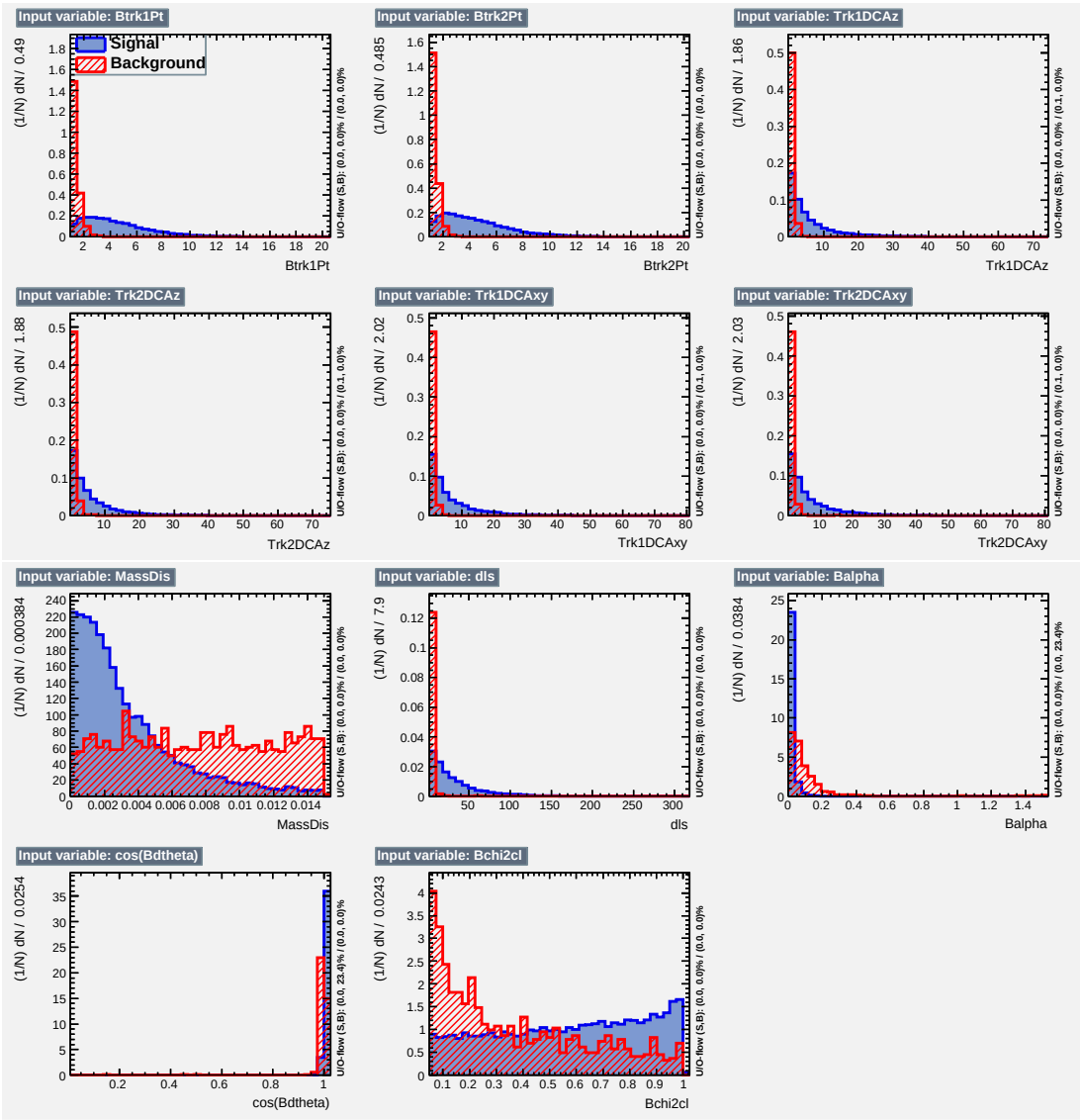

Figure 3.4: Input variables signal and background distributions for MVA training used in PbPb B_s p_T 20-50 GeV/c.

calculated using MC simulation[5]. B' is estimated by a linear interpolation using the number of candidates in sideband region. The signal region was defined as $|M_B - M_B^{PDG}| < 0.08$ GeV/c^2. The distribution of $S/\sqrt{S+B}$ as a function of the requirement applied to the BDT score is shown in Figure 3.5 (b), for B_s candidates of p_T 20-50 GeV/c. The maximum found for $S/\sqrt{S+B}$ was 0.33, and that is the working point chosen for candidates with p_T in the given range. In Figure 3.5 one can check that the background efficiency for this cut is close to 0 and the signal efficiency is close to 1, as desirable. Tables 3.2 and 3.3 summarise the working points chosen depending on the given B meson p_T range, for B_s and B^+, respectivelly.

[5]In Chapter 5 the method of calculating efficiency through MC is explained

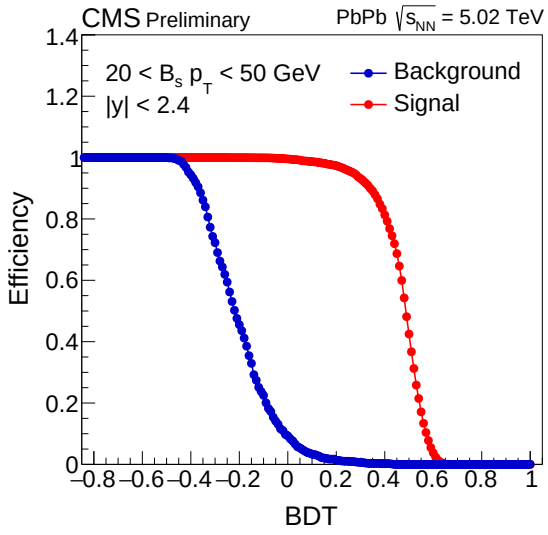

(a) Background and signal efficiencies as a function of the BDT score cut.

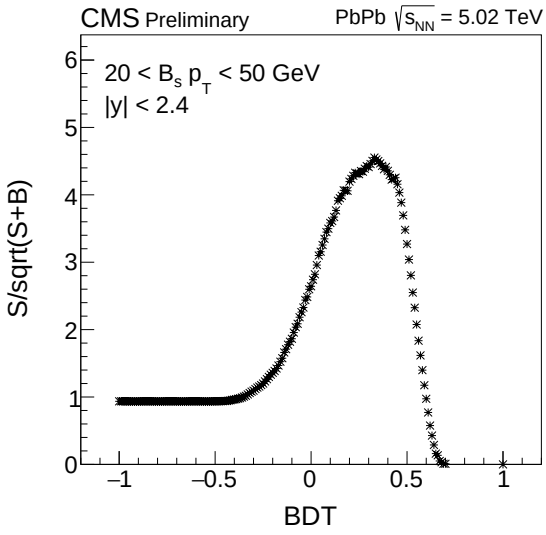

(b) $S/\sqrt{S+B}$ as a function of the BDT score cut.

Figure 3.5: Background and signal efficiencies, and the value of the figure of merit used as a function of the cut applied to the BDT score, in the case of B_s candidates with p_T of 20-50 GeV/c.

p_T (GeV/c)	**5-10**	**10-15**	**15-20**	**20-50**
BDT Score	> 0.32	> 0.29	> 0.35	> 0.33

Table 3.2: Selection criteria used for B_s, depending on its p_T.

3.5 Fiducial Region

Figures 3.6 and 3.7 show the B candidates distributions, as function of rapidity and transverse momentum, for B^+ and B_s, respectively. These maps show that for low B p_T, there are no candidates for low $|y|$ ranges. From this observation, a fiducial region is defined, $i.e$, the phase space that the analysis is able to cover. The analysis is then performed for B meson candidates satisfying[6]

$$\begin{aligned} B^+ : &\quad |y| < 1.5,\ p_T > 10 \text{ GeV/c}; \quad 1.5 < |y| < 2.4,\ 5 < p_T < 60 \text{ GeV/c}\,, \\ B_s : &\quad |y| < 1.5,\ p_T > 10 \text{ GeV/c}; \quad 1.5 < |y| < 2.4,\ 7 < p_T < 50 \text{ GeV/c}\,. \end{aligned} \tag{3.3}$$

This is referred as the analysis fiducial region.

[6] Acceptance corrections explained in Chapter 5 will not correct for the fiducial region definition criteria.

p_T (GeV/c)	**5-7**	**7-10**	**10-15**	**15-20**	**20-30**	**30-50**	**50-100**
BDT Score	>0.07	>0.08	>0.09	>0.09	>0.07	>0.12	>0.24

Table 3.3: Selection criteria used for B^+, depending on its p_T.

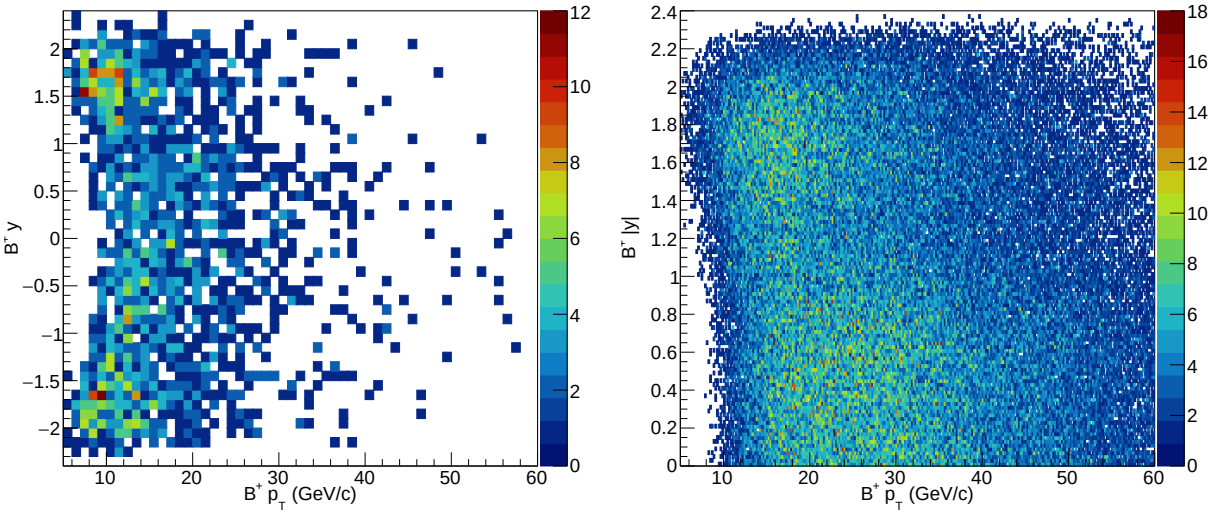

(a) 2-dimensional map for candidates in data.

(b) 2-dimensional map for candidates in MC.

Figure 3.6: 2-dimensional maps in p_T and y of B^+ candidates that met all the selection requirements.

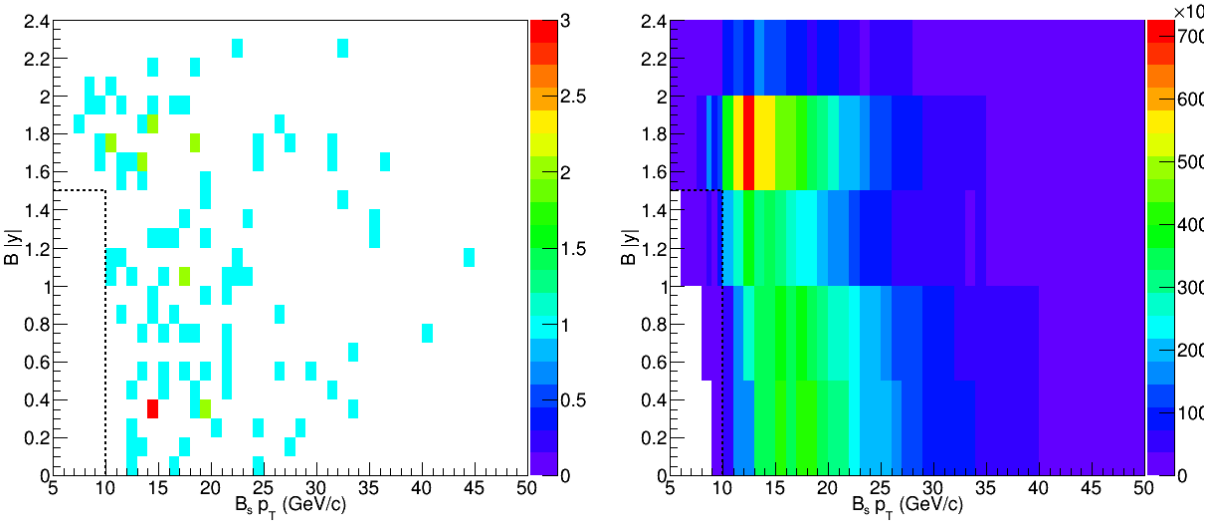

(a) 2-dimensional map for candidates in data.

(b) 2-dimensional map for candidates in MC.

Figure 3.7: 2-dimensional map in p_T and $|y|$ of B_s candidates that met all the selection requirements.

Chapter 4

Signal Extraction

The central ingredient for a production measurement is the raw signal yield extracted from data, the N in the cross section expression presented (1.12). Using the optimised selection described in the previous chapter allowed observing a peak in the B invariant mass distribution. Nevertheless, the background rejection is not perfect, and there will still be present background candidates in the region of interest (the signal region), so one cannot merely ”count” the candidates in that region. To accurately estimate the signal yield of each B meson, one must look for the probability density functions that best describe the signal and background components and fit the reconstructed B mesons' invariant mass distribution. In this chapter, the fitting procedure is described and the resulting invariant mass fits are presented. Finally, the signal statistical significance is evaluated.

4.1 Extended Unbinned Maximum Likelihood Method

Given a data sample, one can estimate the parameters of a probability density function (PDF) through a maximum likelihood method [2]. This method looks for the parameters that maximise the likelihood function, so that the observed data distribution is most probable under the constructed statistical model. The likelihood function can be defined as

$$\mathcal{L}(\boldsymbol{\theta}|\boldsymbol{x}) = P(\boldsymbol{x}|\boldsymbol{\theta}) = \prod_{i=1}^{n} f(x_i|\boldsymbol{\theta}), \tag{4.1}$$

where $\boldsymbol{x}$ is a set of n statistically independent quantities $\boldsymbol{x} = (x_1, ..., x_n)$, that follow the same PDF $f(x, \boldsymbol{\theta})$, a function of $\boldsymbol{\theta}$, the set of parameters $\boldsymbol{\theta} = (\theta_1, ..., \theta_{N_\theta})$. The joint PDF of the data sample is then a product of all the $f(x_i, \boldsymbol{\theta})$. Because of the properties of the logarithm that make it easier to deal with analytically, it becomes advantageous to work with $\ln \mathcal{L}$. The maximum likelihood estimators for $\boldsymbol{\theta}$ are then found by solving the following likelihood equations

$$\frac{\partial \ln \mathcal{L}}{\partial \theta_i} = 0, \quad i = 1, ..., N_\theta. \tag{4.2}$$

This method can be used with binned data. Given a small number of data values x_i this can only

result in loss of information, and hence larger statistical errors for the resulting parameter estimates. The unbinned version is thus prefered, rendering the fitting process independent of binning choices.

The last feature of the used method to be explained is the ”extended” qualifier. When the probability of observing n events depends on the parameters being estimated, this must be introduced into the likelihood expression. If n follows a Poisson distribution of mean μ, the likelihood function becomes

$$\mathcal{L}(\boldsymbol{\theta}|\boldsymbol{x}) = \frac{\mu^n}{n!}e^{-\mu}\prod_{i=1}^{n} f(x_i|\boldsymbol{\theta}). \tag{4.3}$$

The extended unbinned maximum likelihood (EUML) fitting that was performed during this work took advantage of the ROOFIT [38] package, of the ROOT framework. The likelihood maximisation is performed by ROOT's MINUIT [39]. To be exact, MINUIT actually minimises the monotonic function of $\mathcal{L}$, $-\ln 2\mathcal{L}$. The PDFs used during fitting are empirically selected by the user. The domain of $\boldsymbol{\theta}$, $i.e.$, the values that the parameters belonging to $\boldsymbol{\theta}$ are allowed to take, is also set by the user.

4.2 Invariant Mass Fits

Raw yields are extracted through extended unbinned maximum likelihood fits to the invariant mass of reconstructed B meson candidates. The data sample $\boldsymbol{m} = (m_1, ..., m_{N_{obs}})$ is composed of signal and background components, modelled with different PDFs $f_\alpha(m_i;\boldsymbol{\theta})$. Adapting Equation 4.3 to this case, one gets:

$$\mathcal{L}(\boldsymbol{\theta}|\boldsymbol{m}) = \left(\frac{N^{N_{obs}}}{N_{obs}!}e^{-N}\right)\prod_{i=1}^{N_{obs}}\sum_{\alpha} N_\alpha f_\alpha(m_i|\boldsymbol{\theta}). \tag{4.4}$$

The index i runs over the number of observed candidates N_{obs}, while α runs over the number of sample components. The Poisson distribution of the observed number of candidates has an estimated average given by $N \equiv \sum_\alpha N_\alpha$, where N_α is the number of observed candidates belonging to each component of the sample (signal or background), that is estimated by the fitting procedure. N_S is then the signal yield to be extracted, the main parameter of interest.

The fit was done in the mass range of 5-6 GeV/c^2, where the signal mass peak is sure to be found and leaving enough sideband to model the background. It was performed for different B p_T and centrality bins, since the final goal is to achieve a differential production measurement, studying dependencies on these two observables. Especially in the case of B_s the available statistics is limited, and that is even more pronounced when doing the differential measurement. One must then constrain the parameter space during the fit. With that in mind, the fit is first performed to the MC invariant mass distribution of genuine B signal, and the signal shape is extracted to then fit the data mass spectrum. The chosen PDF (probability density function) describing the signal component was a sum of two gaussian functions with the same mean (M) and different widths (σ_1 and σ_2):

$$f_S(\boldsymbol{m}; M, \sigma_1, \sigma_2, \beta) = \beta \cdot \mathsf{G}(\boldsymbol{m}; M, \sigma_1) + (1-\beta)\cdot \mathsf{G}(\boldsymbol{m}; M, \sigma_2). \tag{4.5}$$

The Gaussian function is represented by the letter 'G',and β is the proportion between the two gaussians. The EUML fits to the B meson invariant mass for the entire p_T and centrality range, in MC can be found in Figure 4.1 (a), for B_s, and Figure 4.2 (a), for B^+. The values obtained for the fitted parameters are presented in the boxes near the fit result.

After modelling the invariant mass distribution in MC, the fit is performed to the reconstructed B invariant mass distribution in data, fixing the values of the widths and the relative proportion between the two gaussians to the value obtained from the MC fit. The mean is left as a floating parameter. To describe the combinatorial background produced by the random combination of a J/ψ candidate with tracks that are not coming from the same B decay, an exponential function was chosen. This is enough to model background candidates in B_s. However, studies done to a non-prompt J/ψ MC sample[1], revealed that there is a clear and sizable contribution of two additional background components:

- partially reconstructed B meson decays, for instance $B_s \to J/\psi\ K^+K^-$, where one kaon (K^-) is missed;
- the Cabibbo-suppressed decay $B^+ \to J/\psi\ \pi^+$, where the π is misreconstructed as a K^+.

The model of the combination of these two background components will be called non-prompt background, and is chosen to be the sum of an error function and a gaussian. The error function component mostly comes from the partially reconstructed B meson decays that form peaking structures for values of the invariant mass below ≈5.20 GeV/c^2. The Gaussian contribution mainly comes from $B^+ \to J/\psi\ \pi^+$. The non-prompt background shape is fixed by MC simulation. In the case of B_s, non-prompt J/ψ background component is not considered in the mass fitting in this analysis, since a tight selection on the mass pf the ϕ candidate makes it negligible. Studies done using non-prompt J/ψ MC samples show that the contribution is negligible comparing to the B_s signal after applying the optimal cut. The combined PDF expression for B_s is then:

$$f(\boldsymbol{m}; N_S) = N_S \cdot (\beta^{fixed} \cdot \mathsf{G}(\boldsymbol{m}; M, {\sigma_1}^{fixed}) + (1 - \beta^{fixed}) \cdot \mathsf{G}(\boldsymbol{m}; M, {\sigma_2}^{fixed})) + N_B \cdot \mathsf{E}(\boldsymbol{m}; \lambda_m), \quad (4.6)$$

where G and E denote respectively Gaussian and Exponential functions, normalized in the fitting mass window; N_S denotes the signal yield (the parameter of interest), N_B is the background yield, while λ_m is the exponential decay slope). As mentioned already, the widths of the gaussians, and the proportion β are fixed from the MC fit, and the mean M is left free. In the case of B^+ the combined PDF is given by:

$$f(\boldsymbol{m}; N_S) = N_S \cdot (\beta^{fixed} \cdot \mathsf{G}(\boldsymbol{m}; M, {\sigma_1}^{fixed}) + (1 - \beta^{fixed}) \cdot \mathsf{G}(\boldsymbol{m}; M, {\sigma_2}^{fixed})) + N_B \cdot \mathsf{E}(\boldsymbol{m}; \lambda_m) + N_{NP} \cdot (\text{fixed}), \quad (4.7)$$

where N_{NP} is the number of non-prompt background candidates. The EUML fits to the B meson invariant mass for the entire p_T and centrality range, in data can be found in Figure 4.1 (b), for B_s, and Figure 4.2 (b), for B^+. The values obtained for the fitted parameters are presented in the boxes near the fit result, where only free parameters are shown. The fit results display the χ^2 normalised by its degrees

[1] An inclusive sample with J/ψ coming from the totality of B meson decays.

of freedom as a proof of goodness of fit. Also the pull histogram is shown below the fit results, where one can see that all the data points are within 2σ of the fitting model.

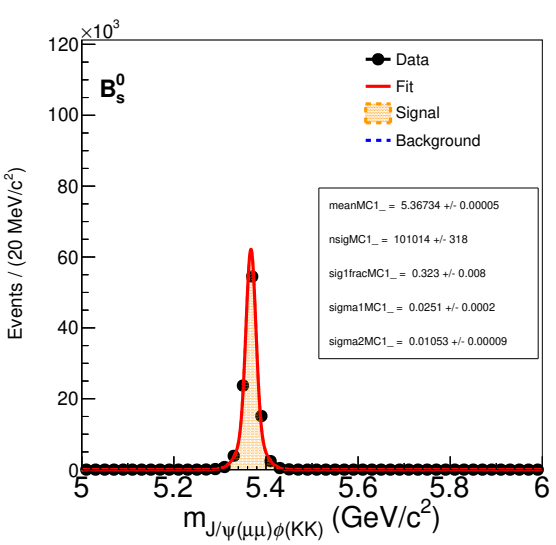

(a) B_s meson invariant mass fit in MC simulation. The mean (meanMC1), widths (sigma1MC1, sigma2MC2) and relative proportion (sig1fracMC1) of the gaussians are presented.

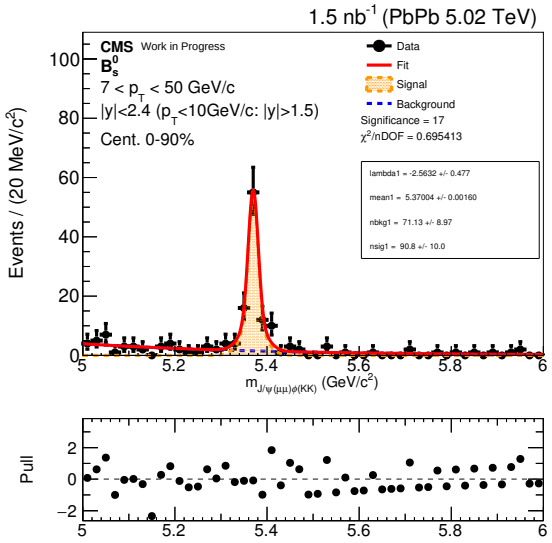

(b) B_s meson invariant mass fit in data. nsig1 and nbkg1 are the number of signal and background candidates, lambda1 is the exponential decay slope and mean1 is the mean of the gaussian. Below the fit, the pull histogram is displayed.

Figure 4.1: Fit results associated with the signal extraction for B_s, for the centrality range 0%-90%, and the B p_T range of 7-50 GeV/c. The parameters shown in the boxes are the ones left free when fitting. In black are the data points; in blue the background model; in yellow the signal model; and in red the resulting total model.

4.3 Signal Statistical Significance

Having the results of the signal extraction, one must estimate how statistically significant it is. The higher the significance, the more unlikely a result is of having occurred given a null hypothesis (H0). In this case, the null hypothesis is the signal shape only being a statistical fluctuation. If this were true the N_S parameter would be 0, and all the candidates would be background.

Defining the likelihood of the background only hypothesis as $\mathcal{L}_B$ and the likelihood of the background+signal hypothesis as $\mathcal{L}_{S+B}$, the significance can be calculated through the likelihood ratio method [40]:

$$\text{Significance} = \sqrt{2 \log \frac{\mathcal{L}_{S+B}}{\mathcal{L}_B}}. \tag{4.8}$$

$\mathcal{L}_{S+B}$ is just the likelihood of the fit results presented in the previous section, with N_S being allowed to float and $\mathcal{L}_B$ is likelihood obtained when repeating the fits but with the value of N_S fixed to 0. In an intuitive manner, if the data distribution is likely under H0, then $\mathcal{L}_{S+B}/\mathcal{L}_B$ will be small and so will be its monotonic function presented in Equation 4.8. Using 4.8 the statistical significance of the B^+ observation was estimated as 51σ and for B_s observation 17σ. This is then the first significant observation of B_s in PbPb collisions, and the most significant one for B^+.

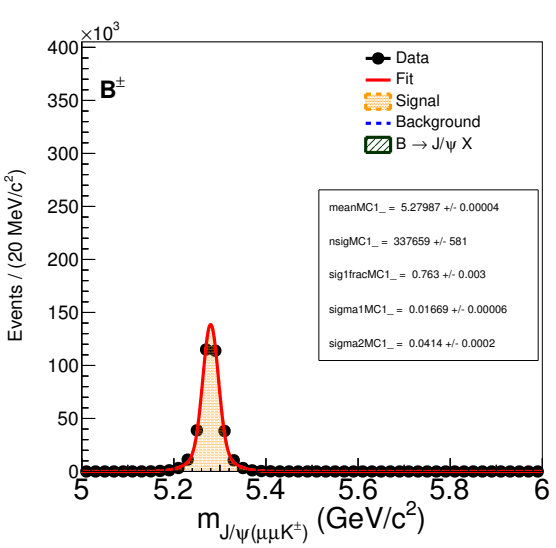

(a) B^+ meson invariant mass fit in MC simulation. The mean (meanMC1), widths (sigma1MC1, sigma2MC2) and relative proportion (sig1fracMC1) of the gaussians are presented.

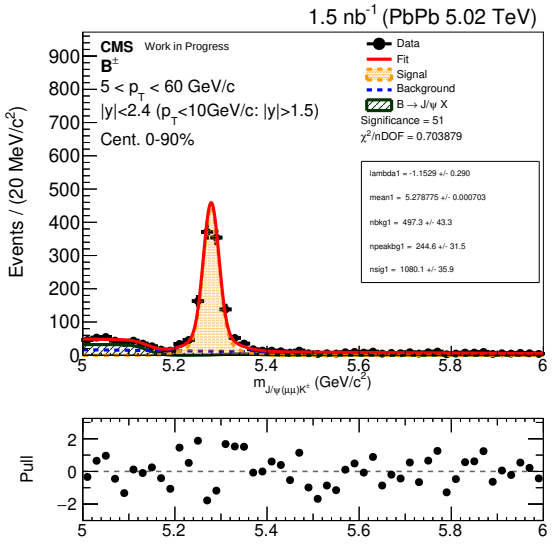

(b) B^+ meson invariant mass fit in data. nsig1, nbkg1 and npeakbg1 are the number of signal, combinatorial background and non-prompt background candidates, respectivelly. lambda1 is the exponential decay slope and mean1 is the mean of the gaussian. Below the fit, the pull histogram is displayed.

Figure 4.2: Fit results associated with the signal extraction for B^+, for the centrality range 0%-90%, and the B p_T range of 5-60 GeV/c. The parameters shown in the boxes are the ones let free when fitting. In black are the data points; in blue the combinatorial background model; in yellow the signal model; in green the non-prompt background; and in red the resulting total model.

Chapter 5

Acceptance and Efficiency

After performing the signal extraction procedure detailed in the previous chapter, one already has the raw yield (N in (1.12)) necessary to compute the cross section. This chapter will focus on obtaining the corrections coming from acceptance (α) and efficiency (ϵ) through the employment of signal MC samples. One must apply these correcting factors, since not all B mesons can be reconstructed by the detector and measured in the analysis. To account for discrepancies between data and MC, regarding muon selection and identification, the tag and probe method is employed. This method is here introduced and explained.

5.1 Acceptances and Efficiencies Estimation

Acceptances and efficiencies corrections are determined from signal MC simulations. Because of the detector design, not all particles generated by the collisions can be detected. For instance, the muon chambers are located in CMS in the $|\eta|$ <2.4 region, so muons with $|\eta|$ >2.4 (possibly coming from B meson decays here studied) will not be detected. The acceptance (α) is here defined as the fraction of B mesons generated within the fiducial region ((3.3)) that produced tracks and muons that lie within the detector's constraints and that fulfil the single muon (see (3.1)) and track ($|\eta|$ <2.4 and p_T >1 GeV/c) acceptance selections. It can be computed by:

$$\alpha = \left. \frac{\mathrm{N_{gen}(B|muon\ and\ track\ acceptance\ selection)}}{\mathrm{N_{gen}(B)}} \right|_{\mathrm{fiducial\ region}}, \tag{5.1}$$

where N(B|selection criteria) stands for the number of B mesons meeting the specified selection criteria. The subscript 'gen' indicates that these are generated mesons.

In order to observe a peak in the B meson invariant mass, the selection detailed in Chapter 3 was applied to the data. There might have been signal candidates that did not pass all the requirements. Also the trigger and B meson reconstruction process results in some fraction of the signal candidates lost. The efficiency (ϵ) is here defined as the fraction of detectable B mesons, with daughters that survived their individual selection requirements, and that were correctly reconstructed and survived all

the selection requirements (detailed in Section 3.4). It can be computed by:

$$\epsilon = \frac{\mathrm{N_{reco}(B|analysis\ selection)}}{\mathrm{N_{gen}(B|muon\ and\ track\ acceptance\ selection)}}\Bigg|_{\mathrm{fiducial\ region}}, \tag{5.2}$$

where the subscript 'reco' refers to reconstructed B mesons. In the end, the correction to the yields extracted in the previous chapter will be done with $\alpha \times \epsilon$, given by:

$$\alpha \times \epsilon = \frac{\mathrm{N_{reco}(B|analysis\ selection)}}{\mathrm{N_{gen}(B)}}\Bigg|_{\mathrm{fiducial\ region}}. \tag{5.3}$$

These formulas are applied for different ranges of B p_T and y. The obtained 2D $\alpha(p_T, y) \times \epsilon(p_T, y)$ map is shown in Figure 5.1, as an example, for B^+.

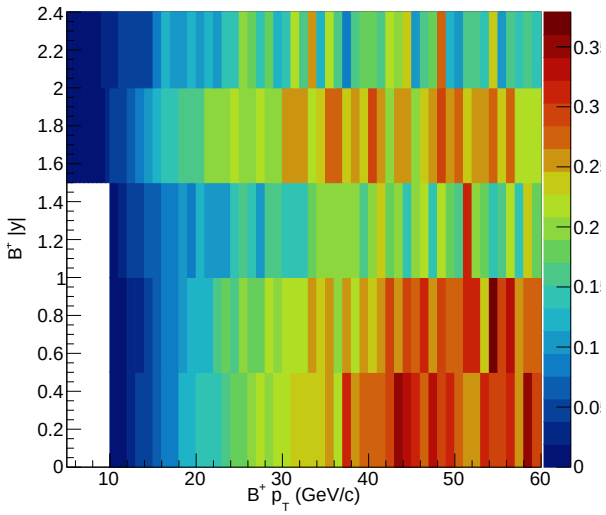

Figure 5.1: Product of B^+ meson acceptance and efficiency as a function of p_T and y within 0-90% centrality. The TnP scaling has already been applied.

From the fine-grained 2D maps one can read a $\alpha \times \epsilon$ value for each candidate in data, with specific p_T and y values. Then, for each p_T range used in the analysis (Δp_T), one computes the average

$$\left\langle \frac{1}{\alpha \times \epsilon} \right\rangle_{\Delta p_T} = \frac{1}{N_{\Delta p_T}} \sum_{i=1}^{N_{\Delta p_T}} \frac{1}{\alpha \times \epsilon(p_T, y)_i} \tag{5.4}$$

where $N_{\Delta p_T}$ represents the number of candidates belonging to the signal region ($|M_B - M_B^{PDG}| < 0.08$ GeV/c^2) of the specific p_T bin for which the calculation is being done. The average should be done strictly speaking over the B signal candidates. The sample of B candidates in data however contains both signal and background candidates, as already explained. The background contamination is thus reduced by restricting to the sample of candidate in the signal region, *i.e.* candidates with invariant mass close to the B meson mass. Given the reduced level of background in the analysis, this approach is found sufficient. More generally, the simple average in (5.4) could be replaced by an weighted average using signal weights obtained with the SPlot method (introduced and presented in the next chapter). Figure 5.2

shows the results of $\langle 1/(\alpha \times \epsilon) \rangle$ for the different p_T bins, for B^+ (a), and B_s (b).

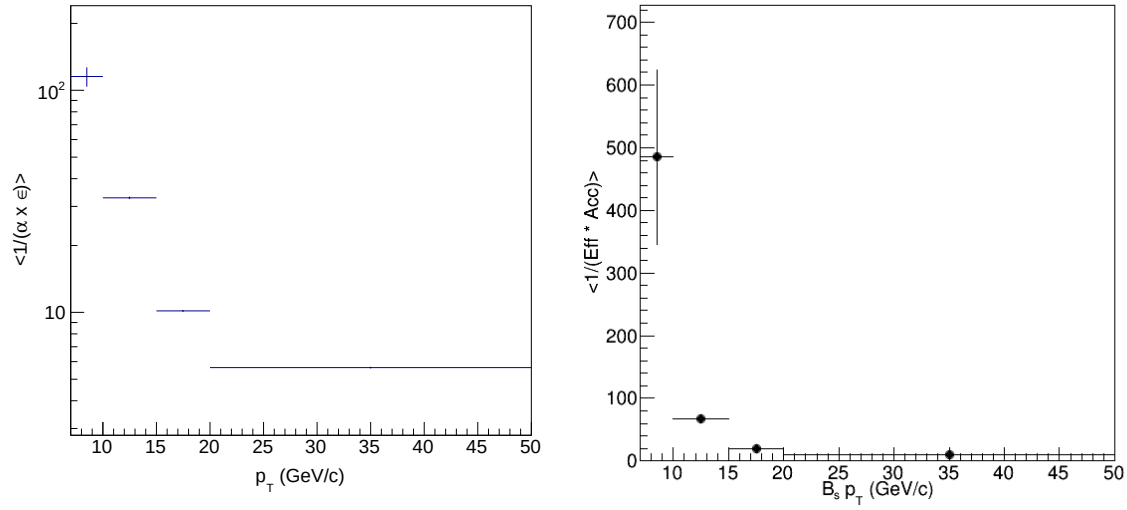

(a) $\langle 1/(\alpha \times \epsilon) \rangle$ for B^+.

(b) $\langle 1/(\alpha \times \epsilon) \rangle$ for B_s.

Figure 5.2: Product of B meson acceptance and efficiency correction factors as a function of p_T within 0-90% centrality. The TnP scaling is included.

5.2 Muon Efficiency: Tag and Probe Corrections

Generally, Monte Carlo simulations are used for efficiencies calculations, as is the case for this analysis. Nevertheless, these simulations do not perfectly model the data taking conditions and the detector response. Therefore, ideally one would want to calculate efficiencies using data, avoiding possible systematic uncertainties arising from data-MC discrepancies. One well established approach, relying on data to estimate particle detection efficiencies, is the Tag and Probe (TnP) method [41].

The fundamental idea of TnP is to reconstruct a well-known resonance built from two objects. In this case, the interest is on muon efficiency so the resonance may be, for instance, the Z or J/ψ particle decaying into two muons. This resonance is built on two muons, one will be called the "tag", the other will be the "probe". Tag muons are required to meet tight[1] selection criteria, so they will almost certainly be muons[2]. On the other hand, probe muons are selected with a very loose set of criteria, that introduces very zero bias: the criteria the efficiency of which is being measured is not used in selecting the probe muon. The probe objects are the ones that will be used to examine the efficiency of some specific selection criteria. A probe muon is paired with a tag muon such that the invariant mass of the formed dimuon is consistent with the mass of the chosen resonant peak. Two invariant mass distributions are formed: "passing probes" and "failed probes", according to whether or not the probe meets the selection criteria for which the efficiency is being estimated. The resulting mass peaks are fitted and the yields

[1]The meaning of this term is quite intuitive. If a lot of requirements are made to data, to make misidentification very unlikely, one calls the selection tight. When few requirements are favourable, to avoid loss of information, the selection is loose.

[2]The fake rate for passing tags selection criteria should be much lower than 1%

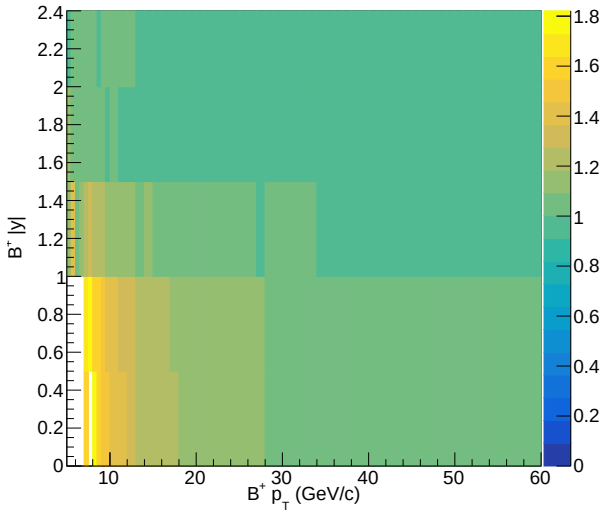

Figure 5.3: TnP scaling factors applied in efficiency calculation for B^+, as function of p_T and y. Computed in the centrality range 0%-90%.

(N) can be used to calculate the measured efficiency for a specific selection, according to:

$$\epsilon_{\text{selection}} = \frac{\text{N}_{\text{passing probes}}}{\text{N}_{\text{passing probes}} + \text{N}_{\text{failed probes}}}. \tag{5.5}$$

The efficiencies of muon trigger (ϵ_{trg}), track reconstruction (ϵ_{trk}), and identification (ϵ_{muid}) were calculated by the CMS dilepton group in this way. Comparing the results obtained from the TnP method in data and MC, the discrepancy can be estimated. The efficiencies were measured as functions of $p_T(\mu)$ and $\eta(\mu)$, in data and MC and their ratios translated into binned muon weights (scaling factors):

$$w(p_T(\mu), \eta(\mu)) = \frac{\epsilon_{\text{data}}(p_T(\mu), \eta(\mu))}{\epsilon_{\text{MC}}(p_T(\mu), \eta(\mu))}. \tag{5.6}$$

These weights were applied to the B meson candidates when calculating the acceptance and efficiencies. There are two muons generated by the B meson, so two single muon scaling factors were applied. Figure 5.3 shows the magnitude of the resulting scaling factors as a function of B^+ p_T and y, for the centrality 0%-90%. These are used to correct the computed $\alpha \times \epsilon(p_T, y)$ maps, as it was done for Figure 5.1. The associated uncertainties are propagated as asymmetric systematic uncertainties for the final cross section value.

Chapter 6

Data-MC Comparison

As stated in the previous chapter, the signal MC samples presented in Chapter 3 are employed in acceptances and efficiencies determination. However, simulation will not describe the data perfectly. This discrepancy was taken into account for muon efficiency, through the TnP method, as detailed in Section 5.2. Potential discrepancies between data and simulation for other variables also need to be quantified. In this chapter, the methods employed for extracting signal distributions from data are described. These allow in turn to perform comparisons between data and simulation, thereby quantifying the effect of detected differences in the efficiency determination.

6.1 Sideband Subtraction Method

The detector acceptance and efficiency are determined from signal MC samples[1]. It is thus important to ensure the MC describes the data. One must be able to obtain data signal distributions of the observables used in the selection, to compare against MC. The sideband subtraction method (SSM) can be used for this purpose. This method requires the use of a separation variable to split the data into regions: a signal region and one or more background regions (the so called "sidebands"). It is assumed that the separation variable is not correlated to the variables of interest, and that no signal events can be found in the background region. The signal region, on the other hand, includes background events. The goal is to estimate the ratio of background events that lie in the signal region, relative to the sidebands and use that factor to arrive at the signal distributions for the variables of interest.

In this case, the invariant mass of the reconstructed B meson candidates was chosen as the separation variable. As already shown in Chapter 4, after applying the optimised selection, there is an observable peak in the distribution, formed by the signal candidates. In Figure 6.1 (a) the B^+ invariant mass distribution is shown, once again. The signal region is defined so that it contains the mass peak. In this case, it was defined as 5.15-5.4 GeV. Outside of the signal region are the sidebands (that we will refer to as left and right sidebands), that only contain background candidates. Having defined the data regions, one can now model the sideband data and integrate the resulting function on the signal region

[1] This is necessary: for example, data cannot be directly used to estimate the fraction of events that fall outside the detector acceptance ... because no such events were detected in the first place!

and the two sidebands, to calculate:

$$\xi = \frac{I_S}{I_{LS} + I_{RS}}, \tag{6.1}$$

where I_S stands for the integral of the fit function in the signal region and I_{LS} and I_{RS} represent the integrals in the left and right sidebands, respectively. An exponential function was used to model the combinatorial background (represented in blue, in Figure 6.1 a). For B^+, the background to the left side of the peak has a sizable contribution from partially reconstructed decays (refer to Chapter 4). Since the behaviour of the background in the signal region is combinatorial, only the right sideband was considered in the fitting and ξ calculation (I_{LS}=0). ξ is the ratio of background candidates in the signal region, relative to the number of background events in the sidebands being considered. One can then obtain the signal distribution of data for the variable of interest (X), according to the expression:

$$N_S(X|\text{signal region}) = N_T(X|\text{signal region}) - \xi \times N_B(X|\text{sidebands}), \tag{6.2}$$

where $N_S(X|\text{signal region})$ stands for the number of signal candidates from the signal region as a function of X, $N_T(X|\text{signal region})$ the total number of candidates from the signal region and $N_B(X|\text{sidebands})$ the number of background candidates from the sidebands. When using the sideband subtraction method the distributions will be in histogram form, and so (6.2) is applied in bins of the variable of interest X. Figure 6.1 (b) shows the signal ($N_S(p_T|\text{signal region})$), background ($N_B(p_T|\text{sidebands})$) and total distributions ($N_T(X|\text{signal region})$) as function of B^+ p_T[2]. The comparison of the obtained signal distribution in data with the distribution in MC can be found in Figure 6.2. These distributions have been normalised to unity, allowing direct comparison. A panel with the ratio between the two distributions is also presented. Most of the ratios are compatible with 1. For p_T 50-100 GeV/c, only the MC is represented, indicating that there are no signal candidates in those bins in the data.

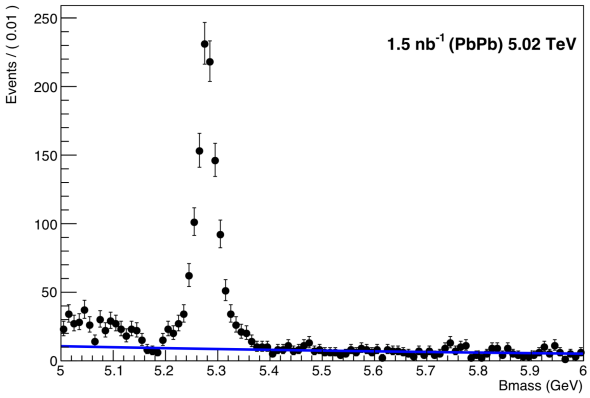

(a) B^+ invariant mass distribution (data points in black). In blue is the exponential function resulting of fitting the right sideband (5.4-6 GeV).

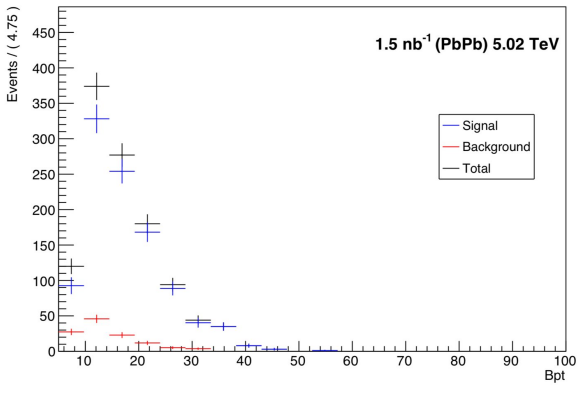

(b) Signal (blue), background (red), and total (black) distribution of candidates from the signal region (5.15-5.4 GeV) as a function of B p_T.

Figure 6.1: Distribution of the separation variable (a). Distributions of one variable of interest, obtained through the sideband subtraction method (b).

[2]B p_T was chosen here just as an example, not for being more interesting than other variables.

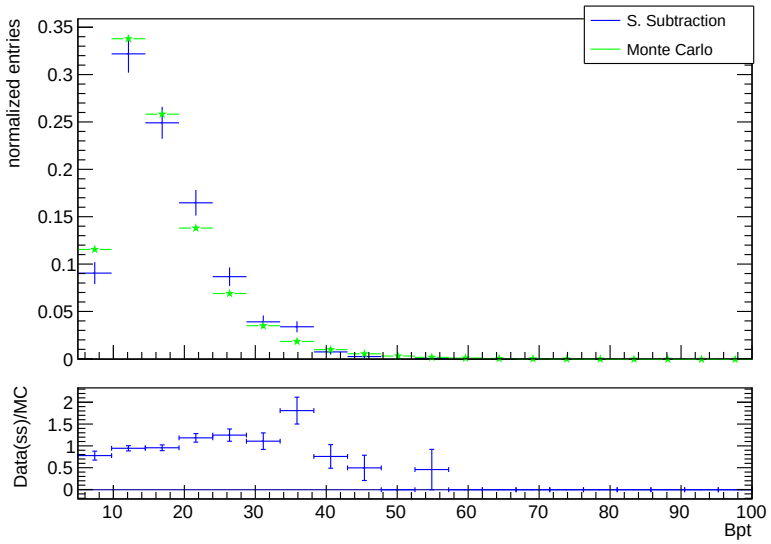

Figure 6.2: Comparison between the signal B p_T distribution obtained with the sideband subtraction method (blue), and its distribution from MC simulation. The bottom panel displays the ratio between the two.

6.2 SPlot Method

The Splot method [42] is another technique that can be employed to obtain signal distributions from data samples. In a general sense, given a data sample composed by different components (signal and background), one can perform an unbinned maximum likelihood fit to a discriminating variable (y) and compute the following weights:

$$ {}_s\mathcal{P}_n(y_e) = \frac{\sum_{j=1}^{N_s} V_{nj} f_j(y_e)}{\sum_{k=1}^{N_s} N_k f_k(y_e)}, \tag{6.3} $$

where y_e is the value of the discriminating variable for an event e, N_s is the number of sample components, f_j is the probability density function of the discriminating variable[3] for the jth component, V_{nj} is the covariance matrix obtained from the fit and N_k is the yield estimated by the fit for the kth component. These are event-by-event weights computed to obtain the distribution of the sample component n. Having computed these weights, one can plot the data distribution of some variable of interest, by weighting each event by its corresponding ${}_s\mathcal{P}_n(y_e)$. The SPlot technique is implemented in ROOT's Roofit package by the class RooStats::SPlot.

The chosen discriminating variable was, as for SSM, the B meson invariant mass. The modelling used is the same as the one detailed in Section 4.2, from which the covariance matrices and yields were calculated. Weights were computed for the background and signal component, originating two weights for each candidate that represent the probability of being a signal (w_s) or background (w_b) given its mass. In an intuitive manner, a candidate with a reconstructed mass that lies in the center of the signal region in Figure 6.1 (a) will have high w_s and low w_b. On the other hand, a candidate with a mass of around 6 GeV/c^2 will very likely have low w_s and high w_b. These weights were applied to the distributions of

[3]That, as was true for the sideband subtraction method, is assumed to be uncorrelated to the variables of interest.

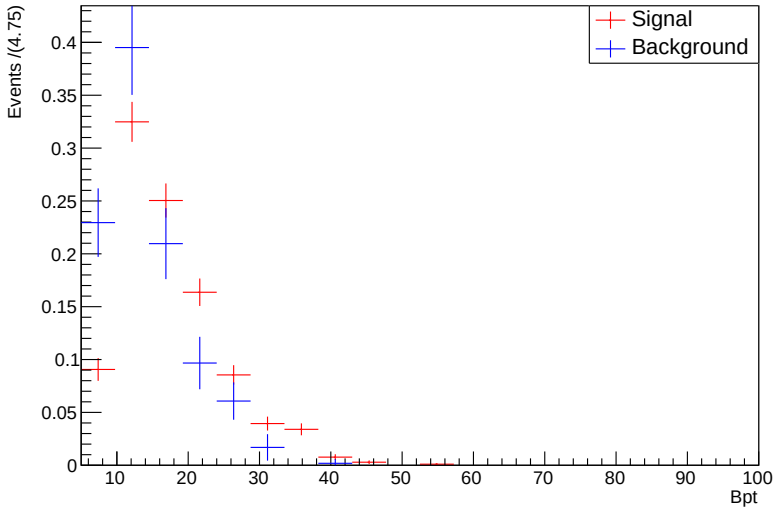

Figure 6.3: Signal (red) and background (blue) distributions of B^+ p_T, obtained by re-weighting the original distribution in data with the weights calculated through the SPlot method.

different variables. As an example, Figure 6.3 shows the signal and background distributions obtained for B^+ p_T. As was done for the SSM, a comparison was made between the p_T signal distribution and its distribution in MC, and can be seen in Figure 6.4. Once again, the distributions have been normalised to unity. Looking at the ratio plot on the bottom, one can see that, once again, most of them are compatible with one, indicating fairly good data-MC agreement.

6.3 Method Comparison

Figure 6.5 shows the comparison between methods and MC for B^+ p_T, the variable used until now as an example. The distributions were again normalised to allow direct comparison. One can see that the results from the two methods are compatible.

Now the question arises of which method can be trusted the most. The SSM here described clearly has various shortcomings. The first one arises by empirical definition of the sidebands. First, because it is possible that some signal will be present in the chosen sideband region, affecting the calculation of the scaling factor ξ. Furthermore, variations may arise depending on the choice of sidebands, which would introduce a systematic uncertainty. The SPlot does not require a division of the discriminating variable into regions, and so these problems do not arise. Another instability associated with the SSM arises from performing the fit only to the sidebands and extrapolating to the signal region. This was already an issue when employing the method for B^+, where different background composition of left and right sidebands did not allow reliable interpolation. Only the right sideband was used, what might not have been sufficient. Overall, the SPlot method is more robust, since it employs the complete modelling of the discriminating variable. The ratios obtained through the SPlot method will be the ones used in the estimation of the systematic uncertainties related to the efficiency calculation.

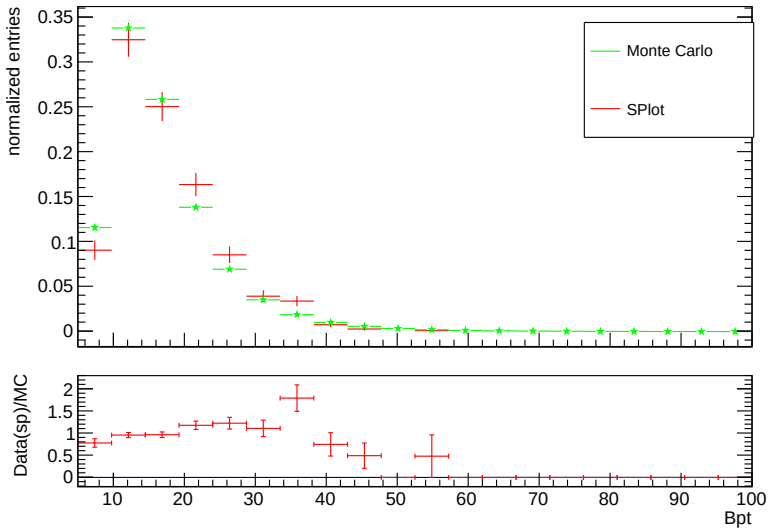

Figure 6.4: Comparison between the signal B p_T distribution obtained with the SPlot method (red), and its distribution from MC simulation (green). The bottom panel displays the ratio between the two.

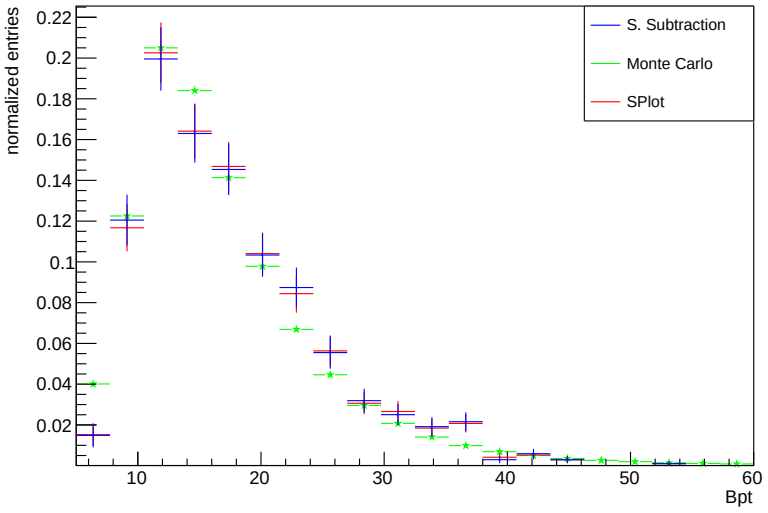

Figure 6.5: Comparison between signal distributions obtained through the SSM (blue) and SPlot (red) for B^+ p_T. These distributions are further compared with the distribution in MC (green).

6.4 Variable Distributions

The comparison between data and MC was performed in order to estimate deviations to be propagated as systematic uncertainties on the efficiencies. Since the optimised selection was obtained from BDT training, and the optimised cuts are applied to the BDT score, the discrepancies found for this variable are the ones that are chosen to be propagated. The training was performed independently for different ranges of the candidates' p_T, and as such the individual distributions of the BDT score in data and MC are compared. Figures 6.6 and 6.7 show the comparisons between the BDT score distribution in MC and the signal BDT score distribution obtained from data through the SPlot method. The variable name displayed in the x axes indicates from which individual training in a specific p_T range the distribution of BDT score was obtained. So, for instance, 'BDT_pt_10_15' is the distribution of the BDT score obtained from the application of the classifier trained in the range of p_T of 10-15 GeV/c. The ratios between the two normalised histograms are also presented, for each comparison. From these ratios, one can obtain the following weight distribution:

$$w(\mathrm{BDT}) = \frac{\mathrm{N_{SPlot}(BDT)}}{\mathrm{N_{MC}(BDT)}}, \tag{6.4}$$

where N(BDT) is the number of events in the bin to which a specific BDT value belongs, and the subscripts 'SPlot' and 'MC' indicate which histogram is being referred to. Section 7.3 details how weights of this kind can be used in the systematic uncertainties estimation.

Looking closer at Figure 6.7, one notices that, for B_s, the statistical uncertainties associated with the SPlot points are considerable. This is expected, since there is much less statistics for this channel. It is also for that reason that for some bins in the histograms there are no signal candidates, and so there is no SPlot data point. For the bins where there are data candidates the results are, in general, compatible within the large statistical uncertainties. In the case of B^+ (Figure 6.6), the uncertainties are much less pronounced. The distributions show the same behaviour for data and MC, and the ratios are, in general, compatible with unity.

Due to the low statistics in B_s, it is not possible to compute the weights described by (6.4) with a fine enough binning. Since the decay topologies and applied selections are similar, the B^+ will be used as a calibration channel for B_s, in the estimation of the systematics associated with data-MC discrepancy (Section 7.3). The main difference between the two channels is the extra kaon in the final state of the B_s decay. So, when computing the final production ratios between these two channels, most systematic uncertainties arising from Data-MC disagreement should cancel to first order, except for the ones coming from track-related variables. Weights can be computed from the ratios obtained for these distributions, like in (6.4), where, instead of BDT, one will use a specific track related variable. Figure 6.8 shows data-MC comparisons for the most relevant track-related variables. These comparisons are shown only for higher yield channel B^+.

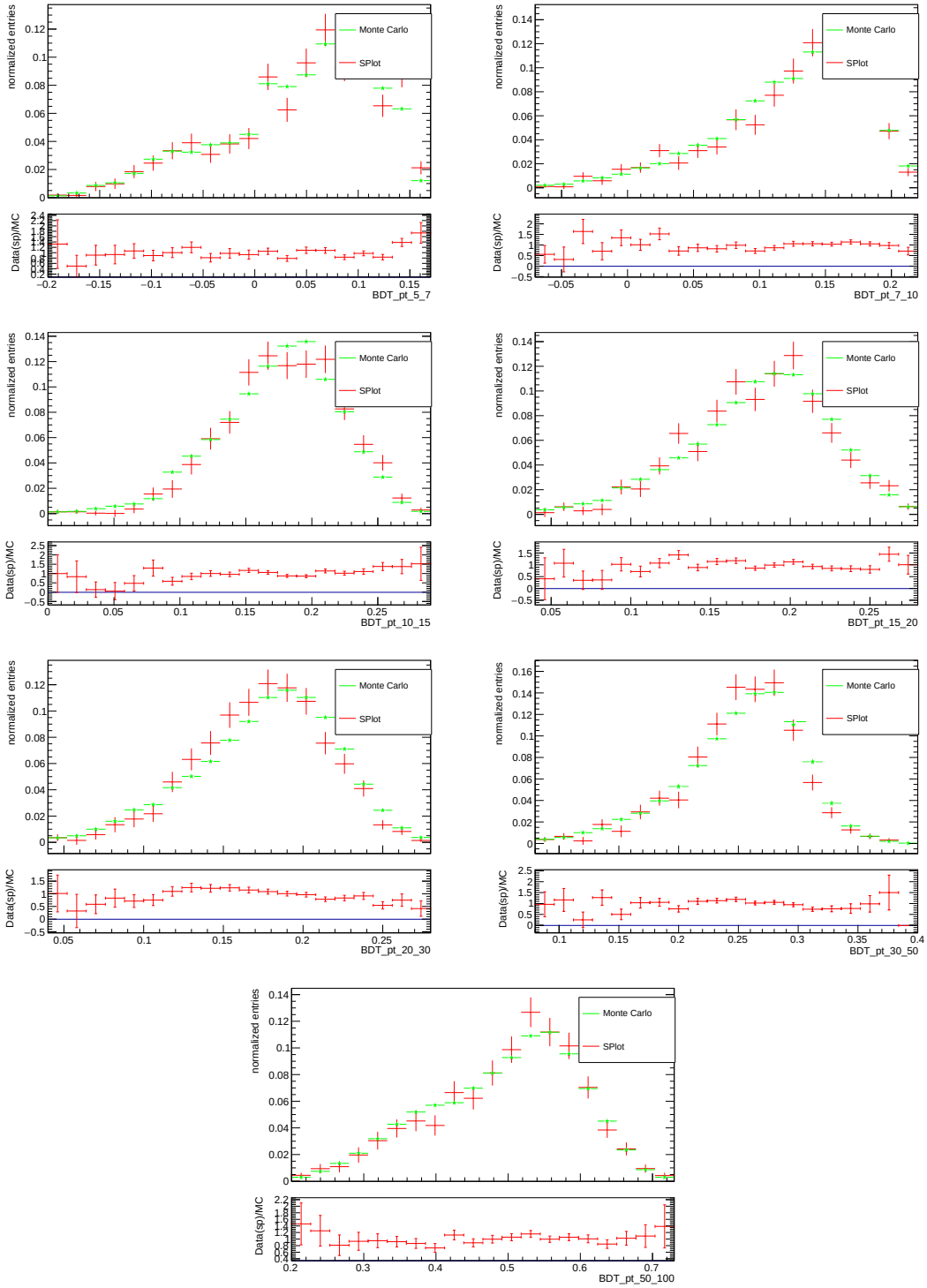

Figure 6.6: Comparison of B^+ BDT score distributions in data (obtained through SPlot) and MC.

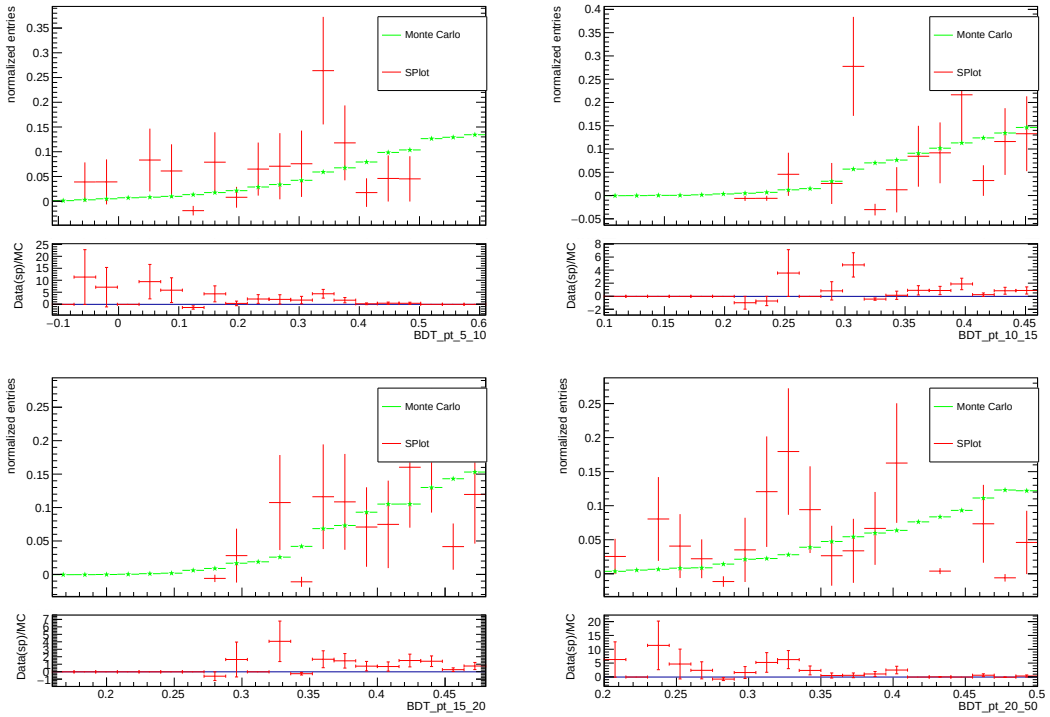

Figure 6.7: Comparison of B_s BDT score distributions in data (obtained through SPlot) and MC.

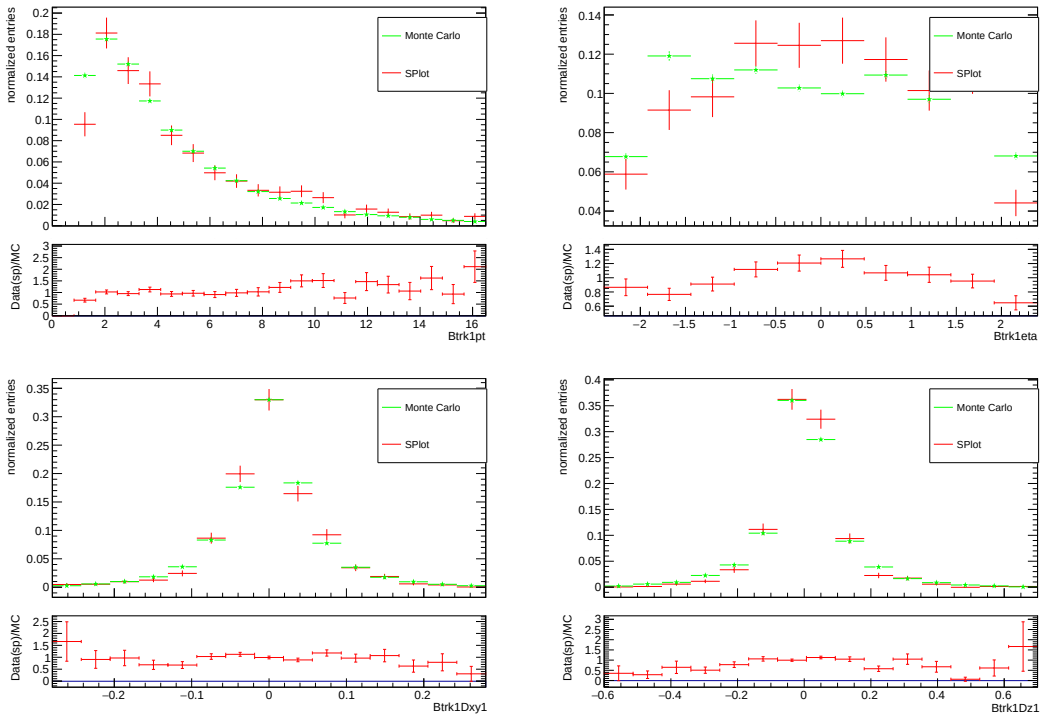

Figure 6.8: Comparison of B^+ distributions in data (obtained through SPlot) and MC, for track-related variables. Transverse momentum of the kaon (Top left); Pseudo-rapidity of the kaon (Top right); Transverse distance to the primary vertex (Bottom left); Longitudinal distance to the primary vertex (Bottom right).

Chapter 7

Systematic Uncertainties

As is true for every experimental result, the production measurements performed for this work are affected by systematic uncertainties arising from various sources. This chapter will tackle the ones that can more significantly affect the final results. The methods used to estimate uncertainties associated with the signal extraction process and with the efficiency estimation will be described. The uncertainty of the branching fraction and the nuclear overlap function will also be presented.

7.1 PDF Variation

The signal extraction detailed in Chapter 4 is central to the analysis, since it allows the determination of the signal yields, the key ingredient of any cross-section measurement. It relies on the empirical choice of the modelling PDF, and while the goodness of fit was verified for the nominal choice, other PDFs could be used to describe the data. In this section, the effect of varying the fitting functions used to model signal and combinatorial background is studied. Variations are sequentially done to the background PDF, while keeping the nominal signal PDF, and the differences between the yield obtained for the variation and the nominal signal yield are calculated. These differences are further divided by the nominal fit models, in order to get a relative value. The biggest deviation is taken as the systematic uncertainty associated with the combinatorial background modelling. The same is done for the signal component of the fit, obtaining the uncertainty arising from the variations in the signal modelling. Finally, both contributions are summed in quadrature and this will be the systematic uncertainty from PDF variation. This process is repeated for all the p_T and centrality bins that are considered in the final differential measurements. The nominal modelling detailed in Section 4.2 is:

- Signal: two gaussians with the same mean but different widths. The widths and the proportion between the gaussians are fixed from MC simulation;
- Combinatorial Background: Exponential function.

In the case of B^+ there is also the non-prompt background component, modelled by an error function and a gaussian, with the parameters fixed from MC. The modelling for this component was not varied

during this estimation.

Starting with the systematics associated with the combinatorial background modelling, the PDF is changed to a linear function, 2nd and 3rd order polynomials. The fit results of these variations, for B_s in the p_T range of 5-50 GeV/c and centrality 0-90%, are presented in Figure 7.1.

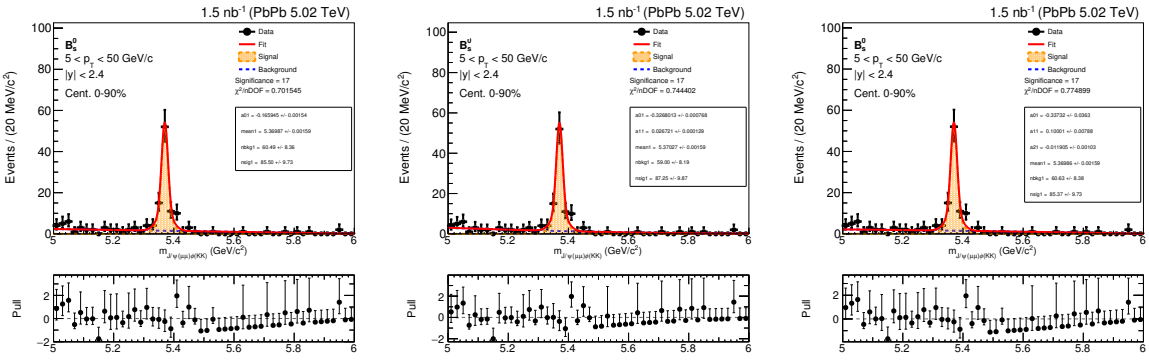

Figure 7.1: Invariant mass fit of B_s candidates. The background PDF from left to right is linear, 2nd order polynomial and 3rd order polynomial.

The systematic uncertainty arising from the variation of the signal PDF was calculated by changing the model from the nominal double Gaussian to a triple Gaussian. A second variation was made where, while keeping the default two gaussians, the mean was fixed to the value obtained from the MC fit. Futhermore, recall that in the signal extraction process the signal shape (except the gaussians' mean) is fixed from MC. Trying to cover a possible discrepancy between the MC and data gaussian resolution, a fit was done to the data with an extra free parameter - a scaling factor between the gaussians' width in data and MC.The signal model used in the fit to data is, in that study:

$$\alpha \frac{1}{a\sigma_1\sqrt{2\pi}} e^{-\frac{1}{2}\frac{(B_{mass}-\mu)^2}{(a\sigma_1)^2}} + (1-\alpha)\frac{1}{a\sigma_2\sqrt{2\pi}} e^{-\frac{1}{2}\frac{(B_{mass}-\mu)^2}{(a\sigma_2)^2}}, \tag{7.1}$$

where a is the resolution scaling factor (the same for both gaussians), α is the relative proportion between the gaussians, σ_1 and σ_2 are the gaussians' widths and μ is the mean shared by both gaussians. In order to examine the potential systematic difference in data and MC signal fit, one is required to define a moderate variation range of the scaling factor in order not to introduce statistical fluctuations in our estimation. To achieve this, the fit was first performed by letting the scaling factor float around in individual p_T bins and inclusive p_T bin (Figure 7.2). Since this study implies adding an extra free parameter, and there is more statistics for B^+, that channel was used to perform the study. The parameter values from the best fit are summarised in Table 7.1.

The result for the most inclusive bin is a = 1.09 $\pm$ 0.04. Looking at the results from the other p_T bins, there are deviations from unity (nominal value of *a*), that are larger for the bins with less statistics (5-7, 7-10). For bins with comparably large statistics the results are compatible with unity. On the other hand, the optimal scaling factors of individual p_T bins agree with that of inclusive p_T bin within a significance of 2 σ. From these observations, the sizable differences are considered to mainly come from statistical limitation in each small p_T range, and the 2 σ deviations are considered to be the statistical uncertainties

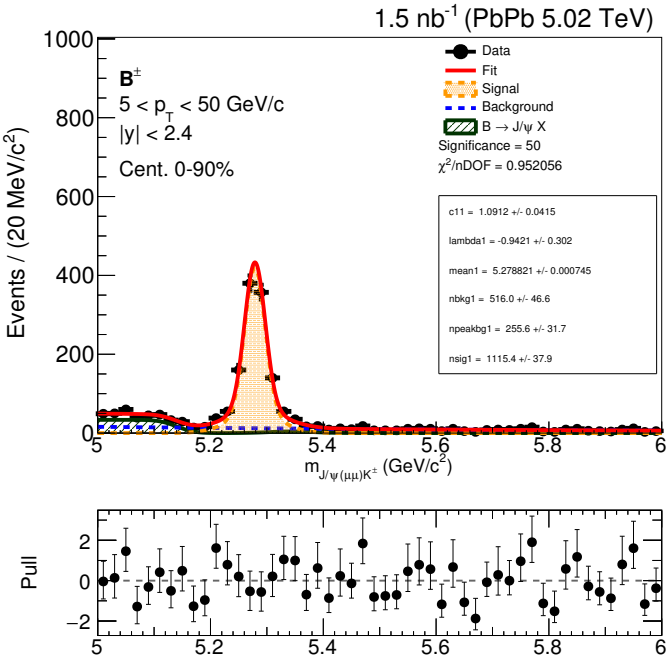

Figure 7.2: Invariant mass fit of B^+ candidates for $5 < p_T < 50$ GeV/c, with an extra free parameter in the signal model *a*, as described by (7.1) ('c11' in the parameter box).

p_T(GeV/c)	Scaling factor *a*
5−7	1.45 ± 0.25
7−10	1.33 ± 0.16
10−15	1.07 ± 0.07
15−20	0.98 ± 0.08
20−30	1.02 ± 0.08
30−40	1.12 ± 0.13
40−50	0.89 ± 0.18
50−60	0.95 ± 0.18
5−50	1.09 ± 0.04

Table 7.1: Summary table of the value obtained for the parameter *a*, when using the signal model described by (7.1), in different p_T bins.

of the scaling factor for individual p_T bins. In conclusion, we can claim that the scaling factor of the inclusive p_T is representative of the scaling factor for all p_T bins. Consequently, we choose to take a 10% variation from the nominal value as a signal PDF systematic uncertainty, following the discrepancy observed for the most inclusive p_T bin. In the end, 2 variations were done from the nominal signal model to account for the resolution discrepancy between data and MC: an 'increased width' with the parameter *a* set to 1.1 and a 'decreased width' with the parameter *a* fixed to 0.9.

The systematic uncertainties associated with PDF variation are summarised in Tables 7.2 and 7.3, for B^+, and Tables 7.4 and 7.5, for B_s.

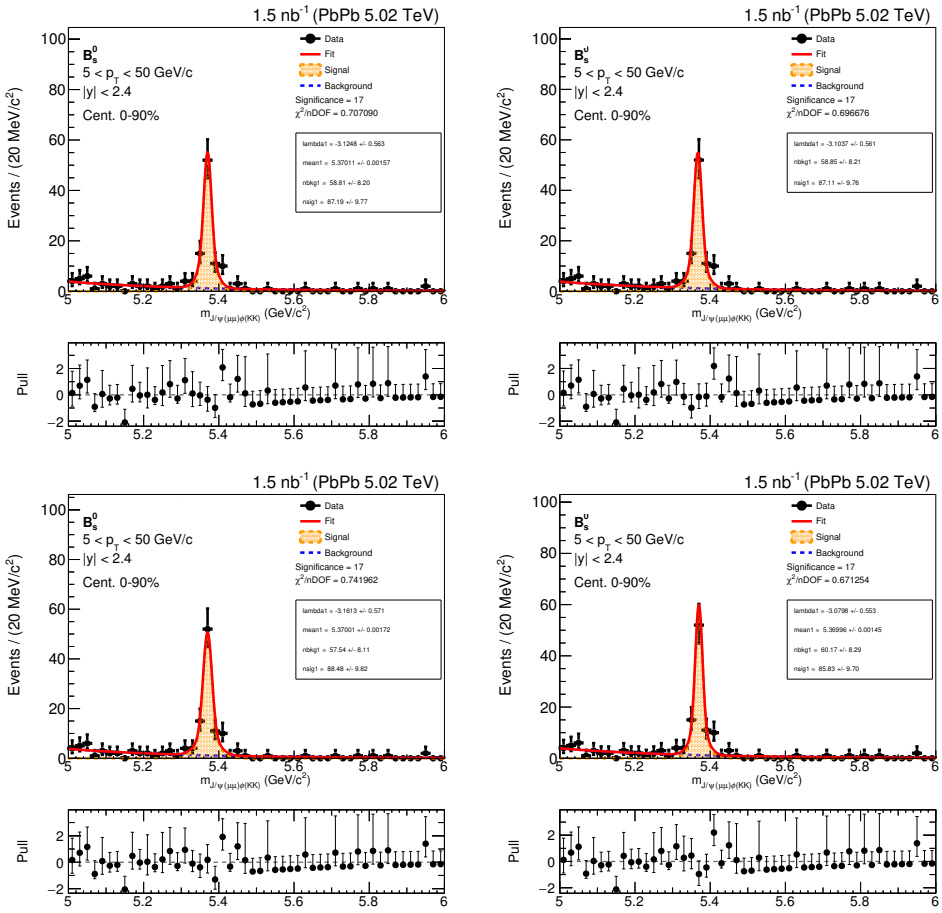

Figure 7.3: Invariant mass fit of B_s candidates. From left to right, top to bottom, the chosen signal pdf is triple gaussian (with widths and relative proportions fixed from MC), double gaussian with all the parameters fixed (including the mean), increased width (a=1.1), and decreased width (a=0.9).

PDF/p_T(GeV/c)	5-7	7-10	10-15	15-20	20-30	30-40	40-50	20-50	50-60
Signal	6.39	4.46	2.67	2.74	2.64	0.701	1.22	2.36	0.420
Background	1.06	0.117	0.546	0.576	0.584	0.174	5.33	1.03	-
Total	6.48	4.46	2.73	2.80	2.70	0.722	5.45	2.57	0.420

Table 7.2: Total systematic uncertainties associated with PDF variation for B^+ p_T bins. All values are in units of %.

PDF/Centrality	0-30%	30-90%	0-90%
Signal	2.71	2.72	2.73
Background	0.405	5.21	0.664
Total	2.74	5.88	2.81

Table 7.3: Total systematic uncertainties associated with PDF variation for inclusive B^+ p_T and different centrality bins. All values are in units of %.

PDF/p_T(GeV/c)	7-10	10-15	15-20	20-10
Signal	0.862	2.62	0.993	1.77
Background	-	2.72	1.56	3.29
Total	0.862	3.78	1.82	3.74

Table 7.4: Total systematic uncertainties associated with PDF variation for B_s p_T bins. All values are in units of %.

PDF/Centrality	0-30%	30-90%	0-90%
Signal	1.71	1.09	1.65
Background	2.36	1.36	2.18
Total	2.92	1.74	2.73

Table 7.5: Total systematic uncertainties associated with PDF variation for inclusive B_s p_T and different centrality bins. All values are in units of %.

7.2 Fit Bias

Another systematic uncertainty associated with the signal extraction procedure arises if there is a bias in the fit. By definition, the fit procedure is unbiased if it yields, on average, the correct value for the parameter of interest, in this case, the number of signal events. One can test this through a pseudo-experiments study. What this entails is the generation of samples of pseudo-data according to the resulting PDF from the fits described in Section 4.2. These are called Toy MCs, since they do not involve underlying realistic physics models or detector responses. In this case, 5000 Toy MCs were generated. Since the original fits to data were extended, the number of events generated in each toy sample follows a Poisson distribution. Each sample of pseudo-data is fitted with the same function that was used in fitting the data. The generation and fitting of the pseudo-data samples is performed using class RooMCStudy [38], implemented in ROOFIT's framework. It allows the drawing of different distributions, like the distribution of the obtained signal yield from the fits to the Toy MC's. Furthermore, it provides the distribution of the quantity:

$$\text{Pull} = \frac{\mathrm{N}_i - \mathrm{N}_0}{\sigma_{\mathrm{N}_i}}, \tag{7.2}$$

where N_i is the number of signal events obtained from the fit to each Toy MC sample, σ_{N_i} is the uncertainty of the fit to each Toy MC and N_0 is the nominal signal yield. The pull distribution is expected to

be a Gaussian with mean equal to 0 and standard deviation equal to 1. Deviations from unit gaussian will be propagated as the systematic uncertainty associated with fit bias. The produced pull distributions can be found in Figure 7.4.

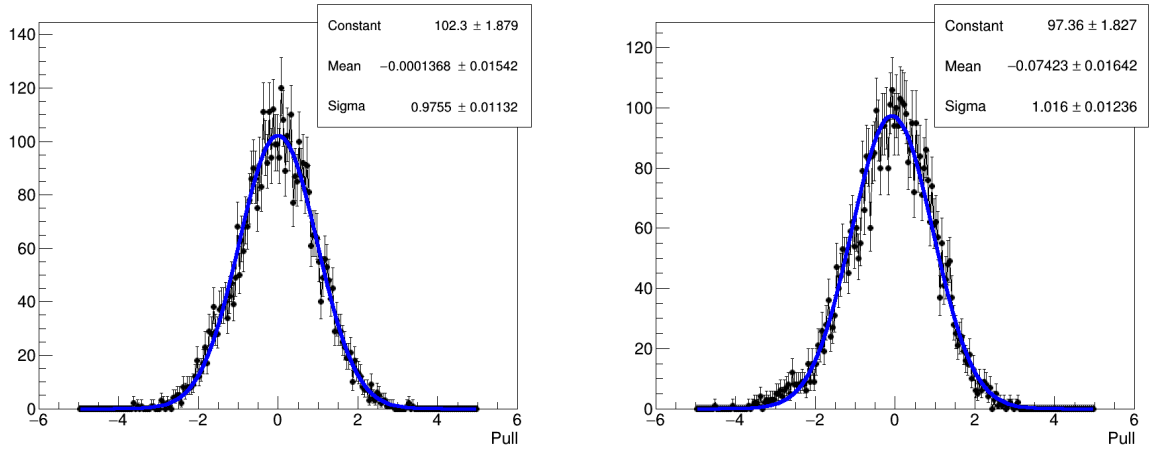

(a) Pull distribution obtained for B^+.

(b) Pull distribution obtained for B_s.

Figure 7.4: Pull distributions obtained from toy MC study.

The deviations to null mean are multiplied by the statistical uncertainty of the signal yield of the corresponding fit to data. The obtained value is further divided by the signal yield, to obtain a relative systematic uncertainty. This estimation is only done for the full datasets of either B^+ or B_s. The systematic uncertainties for both channels can be found in Table 7.6.

Channel	Syst. Uncertainty (%)
B^+	4.6×10^{-4}
B_s	0.83

Table 7.6: Relative systematic uncertainty associated with fit bias, for both channels of the analysis.

7.3 Efficiency Systematics

As stated already, since the $\langle 1/(\alpha \times \epsilon) \rangle$ corrections are calculated employing MC simulation, data-MC disagreement must be accounted for as a systematic uncertainty on the efficiency value, and consequently, on the final production measurements. Since the optimised cuts were applied to the BDT score this was the chosen variable to use in the systematic uncertainties estimation. From the ratios between the signal distributions obtained through SPlot and the MC distributions, weights following (6.4) are computed. These weights are applied to the MC samples and the entire process to compute $\langle 1/(\alpha \times \epsilon) \rangle$ is repeated. The relative systematic uncertainty is then computed through:

$$\Delta = \frac{\langle 1/(\alpha \times \epsilon) \rangle_{\text{weighted}} - \langle 1/(\alpha \times \epsilon) \rangle_{\text{nominal}}}{\langle 1/(\alpha \times \epsilon) \rangle_{\text{nominal}}}, \tag{7.3}$$

where 'nominal' refers to the $\langle 1/(\alpha \times \epsilon) \rangle$ values presented in Chapter5, and 'weighted' refers to the $\langle 1/(\alpha \times \epsilon) \rangle$ values obtained starting with re-weighted MC. Both are displayed in Figure 7.5.

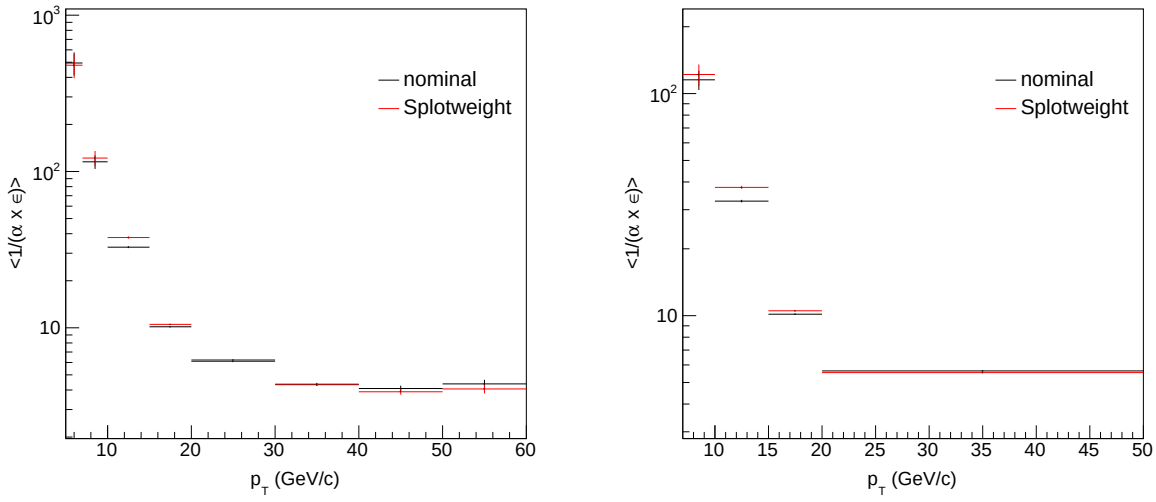

(a) p_T binning used in the final B^+ cross section measurement. (b) p_T binning used in the final B_s cross section measurement.

Figure 7.5: Comparison of nominal $\langle 1/(\alpha \times \epsilon) \rangle$ correction factor with the one obtained with re-weighted MC.

For B^+, MC was re-weighted using the weights obtained from the ratios displayed in Figure 6.6 (data-MC comparison for the BDT score). The systematic uncertainties obtained can be found in Table 7.7, for different p_T bins, and Table 7.8, for different centrality ranges.

p_T(GeV/c)	5-7	7-10	10-15	15-20	20-30	30-40	40-50	20-50	50-60
Syst(%)	3.22	5.67	15.30	3.61	2.15	0.81	4.69	1.72	7.17

Table 7.7: Efficiency systematic uncertainties for different B^+ p_T bins, calculated from the discrepancies between data and MC for BDT score. This comparison was done using the B^+ channel.

Centrality	0-30%	30-90%	0-90%
Syst(%)	9.71	10.66	9.19

Table 7.8: Efficiency systematic uncertainties, for different centrality ranges, calculated from the discrepancies between data and MC for BDT score. This comparison was done using the B^+ channel.

In the case of B_s, since there is not a lot of statistics, it is not possible to compute the weights described by (6.4) with a fine enough binning. Besides, results obtained from the comparisons of B_s are more prone to statistical fluctuations. As such, calculations of the systematic uncertainties using these values would not be a faithful estimation of the systematic uncertainty coming from this source. Trying to avoid overestimation, the results obtained for B^+ were used as a baseline for B_s, given the similar decay topologies. The main difference between the two decay channels is the extra kaon in the final state, for B_s. So, still using B^+, an estimation of the effect of data-MC disagreement for track-related variables was performed. Weights can be computed from the ratios displayed in the bottom panels in Figure 6.8, just like it was done for the BDT score variables. The MC re-weighting was done using the different track-related variables, and the $\langle 1/(\alpha \times \epsilon) \rangle$ computation was performed in each case. The deviations were

calculated with (7.3), and the highest one was summed in quadrature with the systematic uncertainty estimated with the BDT score for the corresponding p_T or centrality range, in the following way:

$$\text{Syst} = \sqrt{\Delta^2_{\text{BDT}} + \Delta^2_{\text{trk}}}. \tag{7.4}$$

p_T(GeV)	7-10	10-15	15-20	20-50
Syst(%)	38.01	7.42	15.92	10.58

Table 7.9: Efficiency systematic uncertainties for different B_s p_T bins, calculated with 7.4. The B^+ channel was used as a baseline channel.

Centrality	0-30%	30-90%	0-90%
Syst(%)	16.53	11.64	20.26

Table 7.10: Efficiency systematic uncertainties for different centrality ranges, calculated with 7.4. The B^+ channel was used as a baseline channel.

7.4 Summary

All the systematic uncertainties that are accounted for in the final cross section results presented in the next chapter are summarised in Tables 7.12 to 7.15. The 'Total' values are obtained by adding all the presented components in quadrature. In addition to the signal yield N and acceptance (α) and efficiency (ϵ) terms, that were presented in the previous section, the branching fractions ($\mathcal{B}$), nuclear modification factor (T_{AA}), and number of minimum bias collisions[1] (N_{MB}), contribute systematic uncertainties. Uncertainties on the branching fractions were calculated by adding in quadrature the uncertainties of each sub-channel. For instance, for the B^+ channel

$$\text{Syst}(\mathcal{B})_{B^+} = \sqrt{\text{Syst}(\mathcal{B})^2_{B^+\to J/\psi K^+} + \text{Syst}(\mathcal{B})^2_{J/\psi\to\mu^+\mu^-)}}. \tag{7.5}$$

The muon efficiency uncertainties arising from the Tag and Probe method are propagated as asymmetric systematic uncertainties on the $1/\langle\alpha\times\epsilon\rangle$ factors. Also, for the charged hadrons, the tracking efficiency uncertainty is considered. The difference in track reconstruction efficiency in data and simulation was estimated in the $D^*\to\pi\pi(\pi\pi)$ analysis [43]. A value 5% was obtained, and is here propagated for each final state track (one kaon for the B^+ and two kaons for the B_s).

Table 7.11 compiles the values of global systematics, $i.e.$ the uncertainties that are not bin dependent, while Tables 7.12 and 7.14 detail the systematic uncertainties calculated for different bins of B p_T, for the two channels used in the analysis. Systematics depending on the centrality range being studied can be found in Tables 7.13 and 7.15. For the production ratio between B_s and B^+, some global uncertainties (T_{AA}, N_{MB}) will cancel. Also the systematic coming from data-MC discrepancies in the BDT scores distributions will cancel (note that it was computed using B^+ in both cases). The remaining

[1] This normalisation is explained in the next chapter.

uncertainty will be then the one coming from data-MC disagreement for track related variables. Finally, coherent variation was employed for numerator and denominator of efficiency in the propagation of the TnP related systematics.

Channel	$\mathcal{B}$	Tracking	Fit Bias	N_{MB}	Total
B^+	2.8	5	(4.6 $\times$ 10^{-4})	$^{+1.03}_{-0.51}$	$^{+5.82}_{-5.75}$
B_s	7.6	10	0.83		$^{+12.63}_{-12.60}$

Table 7.11: Global systematic uncertainties of the analysis. All the values are in form of percentages.

Table 7.12: Summary of systematic uncertainties from each factor for different p_T bins within centrality 0-90% of B_s. All the values are shown in percentage.

Sources/p_T(GeV)	7-10	10-15	15-20	20-50
TnP muon efficiency	+20.0	+9.34	+6.01	+6.05
	-14.2	-8.08	-5.68	-5.73
Selection efficiency	38.01	7.42	15.92	10.58
Signal extraction	0.862	3.78	1.82	3.74
Total	+42.92	+12.51	+17.11	+12.75
	-40.58	-11.60	-17.00	-12.60

Table 7.13: Summary of systematic uncertainties for the B_s meson, for different centrality ranges. All the values are shown in percentage.

Sources/Centrality	0-30%	30-90%	0-90%
T_{AA}	2.0	3.6	2.2
TnP muon efficiency	+22.2	+7.98	+14.3
	-14.0	-7.09	-10.9
Selection efficiency	16.53	11.64	20.26
Signal extraction	2.92	1.74	2.73
Total	+24.16	+13.78	+18.29
	-17.20	-13.29	-16.01

Table 7.14: Summary of systematic uncertainties from each factor for different p_T bins within centrality 0-90% of B^+. All the values are shown in percentage.

Sources/p_T(GeV)	5-7	7-10	10-15	15-20	20-30	30-40	40-50	20-50	50-60
TnP muon efficiency	+21.91	+10.39	+6.99	+5.90	+5.78	+5.96	+6.57	+5.84	+6.46
	-15.20	-8.74	-6.51	-5.54	-5.55	-5.65	-6.07	-5.59	-5.81
Selection efficiency	3.22	5.67	15.30	3.61	2.15	0.81	4.69	1.72	7.17
Signal extraction	6.48	4.46	2.73	2.80	2.70	0.722	5.45	2.57	0.420
Total	+23.07	+12.70	+17.04	+7.43	+9.50	+11.07	+8.19	+6.61	+9.65
	-16.83	-11.39	-16.85	-7.14	-9.36	-7.89	-7.68	- 6.39	-9.23

Table 7.15: Summary of systematic uncertainties for the B^+ meson, for different centrality ranges. All the values are shown in percentage.

Sources/Centrality	0-30%	30-90%	0-90%
T_{AA}	2.0	3.6	2.2
TnP muon efficiency	+8.04	+6.90	+8.10
	-7.14	-6.42	-7.20
Selection efficiency	9.71	10.66	9.19
Signal extraction	2.74	5.88	2.81
Total	+13.05	+14.46	+12.76
	-12.52	-14.24	-12.21

Chapter 8

Results and Discussion

By now all the major components needed to present a final cross section measurement were introduced and discussed: raw signal yields (Chapter 4), acceptances and efficiencies (Chapter 5) and systematic uncertainties associated with these values (Chapter 7). In this chapter, the results for the B^+ and B_s cross sections (within the fiducial region defined in (3.3)) in PbPb collisions at 5.02 TeV are presented. The ratio between the two is also calculated, and compared with the $f_s/(f_d + f_u)$ measured in pp collisions by LHCb [13]. The B_s cross section is further scaled by the published pp cross sections at the same center-of-mass energy [18]. The obtained measurement for the nuclear modification factor is compared with the one already published and shown in Figure 1.9 (b).

8.1 Cross Section

The general expression for a differential cross section as a function of p_T is (1.12). Furthermore, this is the expression used by analysers measuring production in pp collisions. For nuclear collisions, however, the cross section is computed in a slightly different manner:

$$\frac{d\sigma^B}{dp_T} = \frac{1}{2\,\mathcal{B}\,N_{\text{MB}}\,T_{AA}} \frac{N_{\text{obs}}(p_T)}{\Delta p_T} \left\langle \frac{1}{\alpha(p_T, y) \cdot \epsilon(p_T, y)} \right\rangle . \tag{8.1}$$

The main difference is in the normalisation, that is not done with luminosity, due to higher uncertainties in the measuring of this quantity for runs of PbPb collisions. One uses instead the nuclear overlap function (T_{AA}) multiplied by the number of minimum bias events (N_{MB}). N_{MB} is the number of events sampled by minimum bias triggers, that are designed to select hadronic interactions [43]. As already explained in Section 1.1.3, T_{AA} is the effective overlap inverse area for which a given nucleon in one nucleus can interact with another nucleon in the other nucleus. It cannot be directly measured, but average values in centrality classes can be obtained from simulations. These are Monte Carlo simulations that follow the Glauber model and in which each nucleon position in a nucleus is determined event-by-event, allowing the estimation of the geometric quantities of heavy ion collisions (N_{part}, N_{coll}, T_{AA}), by averaging over multiple events. Using HYDJET, the detector effects are also simulated, and these quantities can be averaged in centrality classes defined by the distribution of HF transverse energy. As shown in

Centrality	$< N_{coll} >$	$< T_{AA} >$	$< N_{part} >$
0 - 30%	1042.0±21.0(2%)	15.41±0.30(2%)	269.1±1.0(0.38%)
30 - 90%	115.3±3.7(3.2%)	1.705±0.055(3.2%)	54.44±0.60(1.1%)
0 - 90%	424.1±9.3(2.2%)	6.274±0.137(2.2%)	126.0±0.8(0.67%)

Table 8.1: Summary of the $N_{\rm coll}$, $T_{\rm AA}$ and $N_{\rm part}$ values for the centrality bins used in the analysis. In brackets are also the associated systematic uncertainties [25].

Figure 2.6 this definition is also used in data, and so a correspondence can be made. The geometric quantities estimated by CMS through this method, for the centrality classes used in this analysis, including T_{AA}, can be found in Table 8.1.

All the analysis steps were done for different ranges of B p_T, in order to finally compute the cross section as a function of p_T. The higher statistics for the B^+ channel allowed for a finer binning than the one chosen for the B_s. Figures 8.1 and 8.2 show the measured production of B^+ and B_s (within the fiducial region defined in (3.3)) in PbPb collisions at 5 TeV as a function of p_T. The data points are represented at the signal weighted-average of the p_T distributions of each bin (obtained with the SPlot method). The horizontal bars do not represent uncertainties, but the range of the p_T bin. Only the systematics that vary for different p_T ranges are drawn, represented by the rectangular boxes around the data points. The global uncertainties[1] appear in the top right corner. The dominant systematic uncertainty is the one arising from data-MC disagreement. For bins with relatively low statistics (lower p_T bins for both B_s and B^+), the statistical uncertainty dominates over the systematic one. As expected, the cross section decreases as p_T increases, showing that the production of low p_T B mesons is more probable.

Doing a quantitative comparison with the published cross sections of B_s [18] and B^+ in PbPb collisions [**?**] (measured in the smaller dataset collected in 2015), the present measurement is within the same range of $10^3 - 10^6$ pbGeV^{-1}c. The measurement here presented improved upon those results, having been performed in a wider p_T range for both mesons. The 3 times larger dataset allowed for a finer binning, and thus a better description of B meson production in PbPb collisions as a function of p_T. When comparing the results, it is however important to note that for $p_T < 10$ the present analysis was only performed for B $|y| > 1.5$, while the previous analysis (performed with the 2015 dataset) probed the rapidity range of $|y| < 2.4$ also for 7-10 GeV/c p_T[2].

The cross sections were also measured for different centrality ranges (for the entire, accessible p_T range). The ranges probed were 0-30%, 30-90% and the most inclusive 0-90%. The most inclusive measurement performed within the fiducial region defined in (3.3) can be found in Table 8.2, for both B^+ and B_s.

[1] From sources not differing from bin to bin.

[2] The reason for having adopted a fiducial measurement in this bin is to avoid sensitivity to MC simulation, as indeed QGP physics may modify the B kinematics!

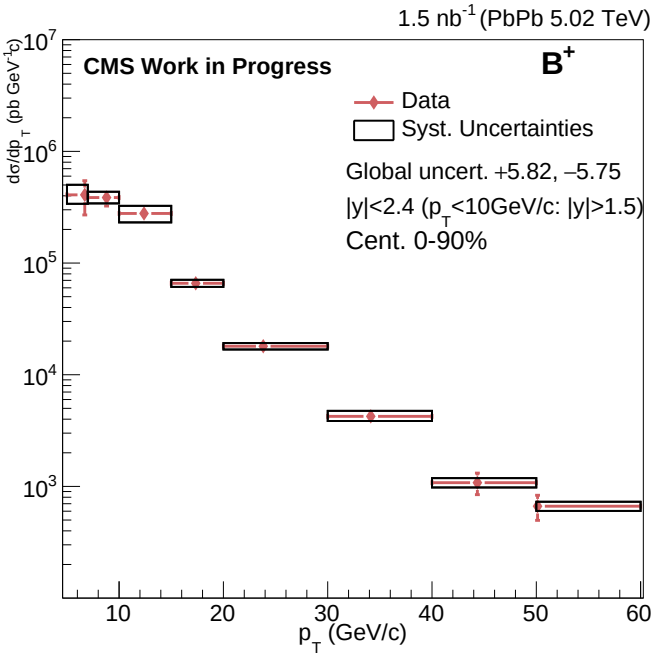

Figure 8.1: B^+ cross section in PbPb collisions, as a function of p_T. The measurement was performed within the analysis fiducial region, defined in (3.3). The data points (represented at the weighted-average of the p_T distributions of each bin), and their respective statistical uncertainties can be seen in light red. The rectangular boxes represent the systematic uncertainties. The horizontal bars do not represent uncertainties, but the range of the p_T bin. The p_T bins range from 5 to 60 GeV/c.

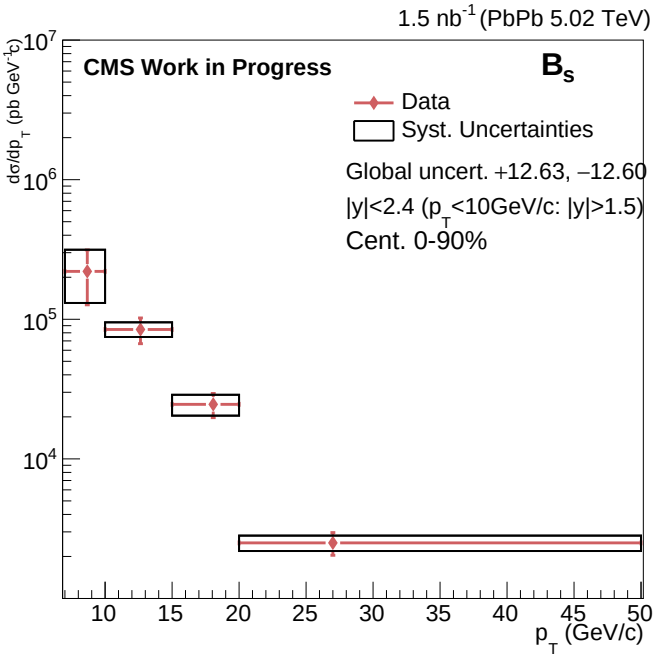

Figure 8.2: B_s cross section in PbPb collisions, as a function of p_T. The measurement was performed within the analysis fiducial region, defined in (3.3). The data points (represented at the weighted-average of the p_T distributions of each bin), and their respective statistical uncertainties can be seen in light red. The rectangular boxes represent the systematic uncertainties. The horizontal bars do not represent uncertainties, but the range of the p_T bin. The p_T bins range from 7 to 50 GeV/c.

Table 8.2: Cross section measurements for 0-90% centrality, within the analysis fiducial region defined in (3.3).

Channel	Cross Section (pb)	Stat. Uncertainty (%)	Syst. Uncertainty (%)
B^+	3.19 $\times$ 10^6	5.13	$^{+14.02}_{-13.50}$
B_s	1.32 $\times$ 10^6	18.5	$^{+22.23}_{-20.37}$

8.2 B_s/B^+ Production Ratio

The cross section measurements quantify the production of B mesons in the QGP medium, and are thus interesting by themselves. However, the physics effects discussed on the first chapter of this thesis can only be probed when in comparison with other production measurements. With that in mind, the cross section of B^+ was calculated for the binning that was used in the B_s case, and the ratio between the two cross sections was computed:

$$R = \frac{\mathcal{B}^{B^+}}{\mathcal{B}^{B_s}} \frac{N_{\text{obs}}^{B_s}}{N_{\text{obs}}^{B^+}} \frac{\langle 1/\alpha^{B_s}\epsilon^{B_s}\rangle}{\langle 1/\alpha^{B^+}\epsilon^{B^+}\rangle} \,. \tag{8.2}$$

The normalisation factors are no longer a source of systematic uncertainty, since they cancelled in the division. Given the similar topology of the decay channels, systematics related to the efficiency determination cancel in first order. The systematics associated with muon efficiency (coming from the application of the tag and probe technique) are then neglected for the ratio. Since the only difference in the final state of the two decay channels is the presence of an extra track for B_s, only uncertainties arising from data-MC disagreement between track-related variables are considered. There is also still a 5% contribution from tracking efficiency (a global uncertainty for the p_T differential measurement). The ratio computed through (8.2) is shown as a function of B p_T in Figure 8.3. The measurement was, once again, performed within the fiducial region defined in (3.3).

As discussed in Chapter 1, one of the signatures of the QGP is strangeness content enhancement. If bottom quarks hadronise through recombination with lighter quarks in the medium (as is predicted for low p_T), one would expect the production ratio between B_s and B^+ to be higher in the QGP medium, comparatively with vacuum. In other words the probability of the bottom quark hadronising with a strange quark should increase in the QGP medium. These probabilities are measured in pp collisions in the form of fragmentation fractions (as explained in Chapter 1). One can then compare the production ratio here obtained for PbPb collisions, with the measured f_s/f_u in pp collisions. LHCb has recently published results at 13 TeV for the fraction $f_s/(f_u + f_d)$. Assuming $f_u \sim f_d$ (reasonable given isospin symmetry), $f_s/(f_u + f_d) \sim 0.5(f_s/f_u)$. The results are then scaled by a factor of 2 and superimposed over the production ratio results. The LHCb results were measured for the p_T range of 3-25 GeV/c which matches well the kinematics of our dataset; while LHCb probes a different rapidity region, no y dependences have been found. The LHCb data points were, in that analysis, fitted to a linear polynomial, modelling the behaviour of the fragmentation fraction as a function of p_T, for the 3-25 GeV/c range. The fit result was superimposed, and drawn only for the p_T range of 7-25 GeV/c. The comparison shows

evidence of strangeness enhancement and hadronisation via recombination, for low to mid p_T. There are still large statistical uncertainties, but even taking the lower bounds for the 7-10 and 15-20 p_T bins, the results indicate enhanced production of B_s with respect to the B^+ in PbPb collisions. For hight p_T (20-50 GeV/c) there are no LHCb data points, and the only point of comparison comes from the linear polynomial fitted in the lower p_T range. However it might be naive to extrapolate the model to the full range of p_T. CMS has not measured significant p_T dependence of f_s/f_u in that p_T range [16]. Consequently, no conclusion is drawn for high p_T, comparatively with the results from the pp collisions. To further probe the high p_T region more PbPb data shall be needed.

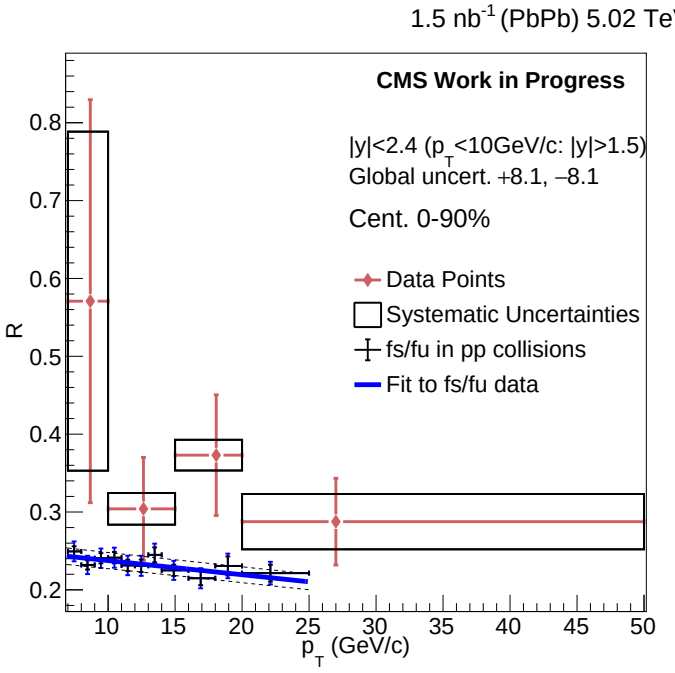

Figure 8.3: B_s/B^+ production ratio, as a function of p_T. The measurement was performed within the analysis fiducial region, defined in (3.3). The data points (represented at the weighted-average of the B_s p_T distributions of each bin), and their respective statistical uncertainties can be seen in light red. The rectangular boxes represent the systematic uncertainties. The horizontal bars do not represent uncertainties, but the range of the p_T bin. The p_T bins range from 7 to 50 GeV/c. The f_s/f_u in pp collisions (LHCb measurement) is also displayed, for comparison [13]. The smaller (black) error bars represent the bin-by-bin systematics of that analysis, and the blue error bars represent the global uncertainties. The resulting function from the linear fit to those data points (performed in the LHCb analysis) is superimposed, in blue. The dashed lines give the total uncertainties on the fit results.

Table 8.3: Production ratio in different centrality ranges.

Centrality range	Production ratio	Stat. Uncertainty (%)	Syst. Uncertainty (%)
0 - 30%	0.568	32.6	9.22
30 - 90%	0.223	20.0	19.18
0 - 90%	0.415	19.2	14.83

The production ratios were also computed for different centrality ranges (Table 8.3). The dominant source of uncertainty is statistic. Figure 8.4 shows the B_s/B^+ production ratio, as a function of $\langle N_{part} \rangle$,

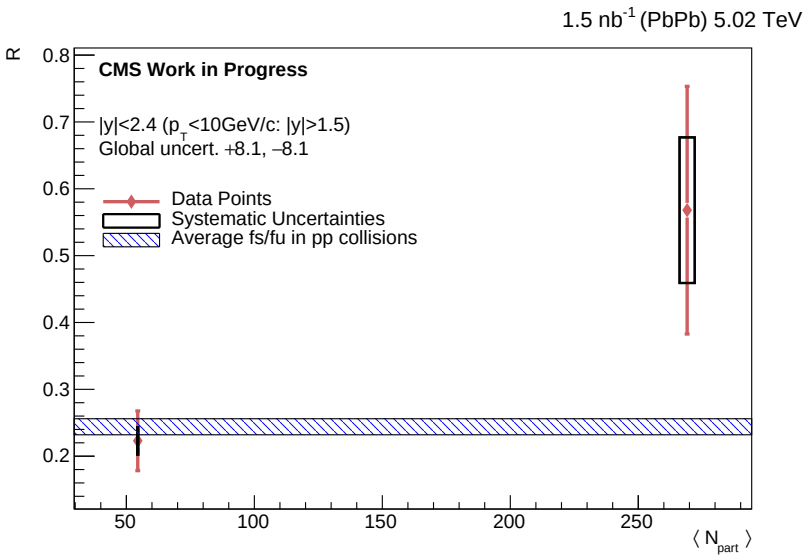

Figure 8.4: B_s/B^+ production ratio, as a function of $\langle N_{part} \rangle$ (corresponding to the centrality class being studied). The measurement was performed within the analysis fiducial region, defined in (3.3). The data points, and their respective statistical uncertainties can be seen in light red. The rectangular boxes represent the systematic uncertainties. The average fragmentation fraction ratio f_s/f_u, measured by LHCb in pp collisions [13] within its uncertainty is represented in blue.

corresponding to the 0-30% and 30-90% centrality classes. One can see that R is higher for the centrality range of 0-30% than for centrality 30-90%. This means that for higher centrality, the production of B_s over B^+ is higher. This is expected, since for higher number of nucleon participants the strangeness content of the medium must be enhanced. The results are compared with the average fragmentation fraction ratio f_s/f_u, measured by LHCb in pp collisions [13], showing evidences of enhanced production ratio for more central collisions.

8.3 Nuclear Modification Factors

In the scope of this thesis, only data coming from PbPb collisions has been analysed. However, as has been explained in Chapter 1, a valuable production measurement to gain insight into the QGP medium is the nuclear modification factor, computed through (1.13). To produce this measurement one must scale the cross sections calculated in PbPb collisions with the cross sections measured in pp collisions at the same center-of-mass energy.[3] A dataset was collected by CMS in 2015, during an LHC run of pp collisions at 5.02 TeV. The B_s cross section was measured with good precision through that dataset[4] [18]. That measurement was performed in 3 p_T intervals in the range of 7-50 GeV/c. Two of those intervals coincided with the ones chosen for the present analysis: 15-20 and 20-50 GeV/c. The B_s nuclear modification is here computed for those p_T ranges, using the published results for the pp reference. The ratio could not be taken for the p_T range from 7 to 15 GeV/c given the fact that for that range the PbPb

[3]The cross section calculated in this work already includes the normalisation by number of collisions(through the factor $1/(T_{AA} \cdot N_{MB})$).

[4]The lack of precision in the previous B_s nuclear modification factor measurement came from the lack of statistics in PbPb, not pp collisions!

cross section was here measured in the fiducial region defined in (3.3), and that the same was not done for pp. The difference in phase space would bias the results. Figure 8.5 shows the resulting nuclear modification factors. The systematic uncertainties associated with the B_s production in pp collisions were added in quadrature to the ones already described for the measurement here performed in PbPb collisions. The resulting uncertainties are represented as rectangular boxes around the data points. The dominant uncertainty is statistical. Table 8.4 summarises the B_s nuclear modification factor results for the 2 p_T intervals.

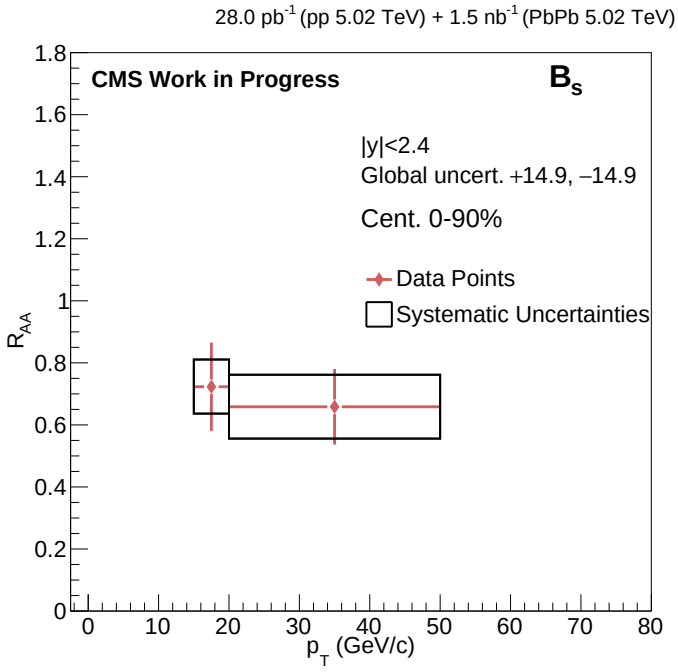

Figure 8.5: B_s nuclear modification factor measured in two p_T intervals, in the range 15-50 GeV/c. The cross sections measured in this work were normalised by the cross sections measured in pp collisions at the same center-of-mass energy, published by CMS [18]. The data points (represented at the center of the bin), and their respective statistical uncertainties can be seen in light red. The rectangular boxes represent the systematic uncertainties. The horizontal bars do not represent uncertainties, but the range of the p_T bin.

Table 8.4: B_s nuclear modification factor for the two p_T intervals studied.

p_T (GeV/c)	R_{AA}	Stat. Uncertainty (%)	Syst. Uncertainty (%)
15-20	0.72	19.7	$^{+12.13}_{-11.97}$
20-50	0.66	18.5	$^{+15.69}_{-15.57}$

A comparison can be made with the nuclear modification results obtained from the 2015 dataset (Figure 1.10). The published B_s R_{AA} for the p_T of 15-50 GeV/c was $R_{AA} = 0.80 \pm 0.30$ (stat) $\pm$ 0.17 (syst) [18]. That result was compatible with values higher than unity (within systematic and statistical uncertainties), and so there was still a case to be done for enhancement in that p_T range. The measurement here presented is finer in that range, and while still being compatible with the previous result, even taking the most conservative value from the statistical uncertainty, it is lower than unity. This ob-

servation leads to the conclusion that there is no absolute[5] B_s enhancement in the QGP medium, when compared to the vacuum, for the p_T range of 15-50 GeV/c, and that this meson production is, on the contrary, suppressed by the medium for this kinematic range (as was already observed for the B^+).

One can go further and compare the calculated B_s R_{AA} with the B^+ R_{AA} shown in Figure 1.10. It is seen that for the p_T range of 15-20 GeV/c the B^+ R_{AA} is below 0.5. The measured B_s R_{AA} shows increased production in the QGP medium relative to the B^+, even when taking the most conservative value (the lower bound). That is compatible with what was seen in the comparison between the B_s/B^+ production ratio and the fragmentation fraction f_s/f_u, for the same p_T range of 15-20 GeV/c, and once again corroborates B meson production through recombination in the medium with increased strangeness content. On the other hand, the B_s R_{AA} measured for the p_T range of 20-50 GeV/c is compatible with the B^+ R_{AA} for 20-30 GeV/c. This measurement becomes lower than the B_s R_{AA} again for 30-50 GeV/c. A direct comparison could be done, allowing to draw definite conclusions, between the same p_T ranges.

[5]Without normalising with B^+ production. It could never truly be an absolute value, since we are comparing with the results from pp collisions.

Chapter 9

Conclusions

The advent of the LHC and its detectors has brought large advancements in the study of nuclear collisions at the highest energies, and to the understanding of the properties of the hot and dense medium produced therein. This thesis is developed in the framework of the exploration of heavy quark production as novel probes of the QGP. B meson decays are here reconstructed for the first time in ion collisions, thanks to the exquisite capability of the CMS detector despite the harsh environment produced by energetic ion collisions.

B meson production measurements in PbPb collisions allow to probe the properties of the QGP medium. In particular, it allows to study the phenomena of parton energy loss - its precise kinematic dependence (facilitated by the full reconstruction of its decay) - and of quark recombination effects such as strangeness enhancement.

In this work, productions of B^+ and B_s mesons were measured in PbPb collisions at $\sqrt{s_{NN}}$ =5.02 TeV, using a dataset collected by CMS at the end of 2018, corresponding to an integrated luminosity of 1.5nb^{-1}. The mesons were reconstructed in the final states $B^+ \to J/\psi K^+$ and $B_s \to J/\psi$, with $J/\psi \to \mu^+\mu^-$ and $\phi \to K^+K^-$. The first observation of the B_s meson in PbPb collisions was here achieved, with a statistical significance well in excess of 5 standard deviations. The production cross sections for both mesons have been measured, by correcting the signal yields extracted from the data by detector acceptance and reconstruction efficiency, as well as T_{AA} and N_{MB}. The measurements were performed differentially, as a function of the mesons transverse momenta (p_T) and collision centrality. Previous related measurements [18], performed by CMS with a PbPb data set collected in 2015 that was three times smaller than the current data set, did not provide a sufficiently significant B_s signal. While measurements were nevertheless extracted from those data, the results were affected by too large uncertainties and did not allow definitive conclusions on the production of B_s relative to B^+ in PbPb collisions. In the current measurement, higher levels of significance and precision are attained, and a wider kinematic region reached (p_T up to 50 GeV/c).

In addition to their individual cross sections, also the B_s/B^+ production ratio is measured. The ratio is compared to the corresponding fragmentation fraction ratio (f_s/f_u) results measured by LHCb in pp collisions, at 13 TeV, as a function of p_T in the range of 7-25 GeV/c. The ratio results provide evidence

of an enhancement in the low to mid p_T region, indicating a possibly sizeable contribution to b-quark hadronization from recombination effects in a medium with an enhanced strangeness population. The B_s cross section results in PbPb collisions at 5.02 TeV here obtained are also normalised by the corresponding results obtained in pp collisions at the same energy [18]. This study was done for the p_T range of 15-50 GeV/c. The obtained result for the B_s nuclear modification factor, R_{AA}, increases significantly the precision of the previous CMS measurement [18]. While preliminary hints of enhancement had been suggested by those results in the lower p_T region, these updated results point to an overall suppression of B_s production, in PbPb compared to pp collisions, in the mentioned, higher p_T range. Further comparing the B_s R_{AA} here obtained with the B^+ R_{AA} previously reported [18], one can see that there is an hint of an enhancement by the QGP of B_s production relative to B^+. The outcome of this R_{AA} comparison study is accordingly compatible with the production ratio comparison with f_s/f_u also reported above. These results would be explained, as mentioned previously, by sizeable contribution of bottom quark recombination with lighter quarks in the presence of a medium with increased strangeness content.

The precision of the results here reported will benefit from increased PbPb data sets that will be collected in future LHC runs. The combined PbPb data collected during 2015 and 2018 can be used at once to obtain improved results. In particular, this will yield more precise results for the low-p_T region, where recombination effects are expected to be more pronounced. The larger overall sample could also allow for a finer kinematic and centrality binning. The B^0 meson as not studied as part of this thesis, due to lack of simulated samples. The production ratios between B^+ and B^0 could be further used to probe bottom-quark hadronization in the QGP medium, and the effect of recombination. The nuclear modification factor measurements shall benefit from the combined PbPb samples, as well as from the larger pp reference dataset collected by CMS in 2017, at the same center-of-mass collision energy as studied in this work. Furthermore, the nuclear modification factors of all 3 mesons B^+, B_s and B^0, could be measured with greater precision by using all the PbPb and pp data collected at 5.02 TeV. More data will allow to start exploring rarer processes, and new hadrons, such as the B_c meson, allowing to probe potential effects of charm enhancement, and the X(3872), opening the window into the study of exotic spectroscopy in ion collisions. All these measurements and novel probes shall add precision to the study of energy loss, its flavour dependence, quark recombination effects, and beyond — towards an improved understanding of the primordial QGP medium.

Bibliography

[1] M. D. Schwartz. *Quantum Field Theory and the Standard Model*. Cambridge University Press, 2014. ISBN 1107034736, 9781107034730. URL http://www.cambridge.org/us/academic/subjects/physics/theoretical-physics-and-mathematical-physics/quantum-field-theory-and-standard-model.

[2] M. Tanabashi et al. Review of Particle Physics. *Phys. Rev. D*, 98:030001, Aug 2018. doi: 10.1103/PhysRevD.98.030001. URL https://link.aps.org/doi/10.1103/PhysRevD.98.030001.

[3] A. Bettini. *Introduction to Elementary Particle Physics*. Cambridge University Press, 2008. doi: 10.1017/CBO9780511809019.

[4] F. Karsch and E. Laermann. Thermodynamics and in medium hadron properties from lattice QCD. pages 1–59, 2003.

[5] W. Busza, K. Rajagopal, and W. van der Schee. Heavy Ion Collisions: The Big Picture, and the Big Questions. *Ann. Rev. Nucl. Part. Sci.*, 68:339–376, 2018. doi: 10.1146/annurev-nucl-101917-020852.

[6] J. Crkovska. *Study of the J/ψ production in pp collisions at $\sqrt{s} = 5.02$ TeV and of the J/ψ production multiplicity dependence in p-Pb collisions at $\sqrt{s_{NN}} = 8.16$ TeV with ALICE at the LHC*. PhD thesis, Université Paris-Saclay, 10 2018.

[7] C. A. Salgado. Lectures on high-energy heavy-ion collisions at the LHC. In *2008 European School of High-Energy Physics, Herbeumont-sur-Semois, Belgium, 8-21 June 2008*, pages 239–280, 2009.

[8] M. L. Miller, K. Reygers, S. J. Sanders, and P. Steinberg. Glauber modeling in high energy nuclear collisions. *Ann. Rev. Nucl. Part. Sci.*, 57:205–243, 2007. doi: 10.1146/annurev.nucl.57.090506.123020.

[9] X. Dong, Y.-J. Lee, and R. Rapp. Open Heavy-Flavor Production in Heavy-Ion Collisions. 2019.

[10] Y. L. Dokshitzer and D. E. Kharzeev. Heavy quark colorimetry of QCD matter. *Phys. Lett.*, B519: 199–206, 2001. doi: 10.1016/S0370-2693(01)01130-3.

[11] J. Rafelski and B. Müller. Strangeness production in the quark-gluon plasma. *Phys. Rev. Lett.*, 48: 1066–1069, Apr 1982. doi: 10.1103/PhysRevLett.48.1066. URL https://link.aps.org/doi/10.1103/PhysRevLett.48.1066.

[12] The STAR Collaboration. Strangeness Enhancement in Cu-Cu and Au-Au Collisions at $\sqrt{s_{NN}} = 200\ \mathrm{GeV}$. *Phys. Rev. Lett.*, 108:072301, Feb 2012. doi: 10.1103/PhysRevLett.108.072301. URL https://link.aps.org/doi/10.1103/PhysRevLett.108.072301.

[13] The LHCb Collaboration. Measurement of b hadron fractions in 13 TeV pp collisions. *Phys. Rev. D*, 100:031102, Aug 2019. doi: 10.1103/PhysRevD.100.031102. URL https://link.aps.org/doi/10.1103/PhysRevD.100.031102.

[14] The ATLAS Collaboration. Determination of the ratio of b-quark fragmentation fractions f_s/f_d in pp collisions at $\sqrt{s} = 7$ TeV with the ATLAS detector. *Phys. Rev. Lett.*, 115(26):262001, 2015. doi: 10.1103/PhysRevLett.115.262001.

[15] The LHCb Collaboration. Measurement of the fragmentation fraction ratio f_s/f_d and its dependence on B meson kinematics. *JHEP*, 04:001, 2013. doi: 10.1007/JHEP04(2013)001.

[16] B. A. F. S. Alves. Measurement of b-quark fragmentation fractions ratios at the CMS experiment: a key ingredient for the $B_s^0 \to \mu^+\mu^-$ rare decay analysis. Master's thesis, Instituto Superior Técnico, 2018. URL http://cds.cern.ch/record/2649927?ln=en. CERN-THESIS-2018-274.

[17] The CMS Collaboration. Measurement of the total and differential inclusive B^+ hadron cross sections in pp collisions at $\sqrt{s}$ = 13 TeV. *Phys. Lett.*, B771:435–456, 2017. doi: 10.1016/j.physletb.2017.05.074.

[18] The CMS Collaboration. Measurement of $\mathrm{B_s^0}$ meson production in pp and PbPb collisions at $\sqrt{s_{\mathrm{NN}}} =$ 5.02 TeV. *Physics Letters B*, 796:168–190, Sep 2019. ISSN 0370-2693. doi: 10.1016/j.physletb.2019.07.014. URL http://dx.doi.org/10.1016/j.physletb.2019.07.014.

[19] Bruning et al. LHC design report. vol. i: The LHC main ring. Technical report, CERN, 2004.

[20] A. De Angelis and M. Pimenta. *Introduction to Particle and Astroparticle Physics*. Springer Milano, 2008. URL https://link.springer.com/book/10.1007/978-3-319-78181-5.

[21] The CMS Collaboration. CMS Luminosity - Public Results. URL https://twiki.cern.ch/twiki/bin/view/CMSPublic/LumiPublicResults. Accessed on September 20th 2019.

[22] The CMS Collaboration. The CMS Experiment at the CERN LHC. *JINST*, 3:S08004, 2008. doi: 10.1088/1748-0221/3/08/S08004.

[23] The CMS Collaboration. The Performance of the CMS Muon Detector in Proton-Proton Collisions at $\sqrt{s}$ = 7 TeV at the LHC. *JINST*, 8:P11002, 2013. doi: 10.1088/1748-0221/8/11/P11002.

[24] The CMS Collaboration. Description and performance of track and primary-vertex reconstruction with the CMS tracker. *Journal of Instrumentation*, 9(10):P10009–P10009, oct 2014. doi: 10.1088/1748-0221/9/10/p10009. URL https://doi.org/10.1088%2F1748-0221%2F9%2F10%2Fp10009.

[25] The CMS Collaboration. Centrality and Event Plane reconstruction for PbPb collisions at 5 TeV in 2015. CMS AN Note 2015/080, 2015. URL http://cms.cern.ch/iCMS/user/noteinfo?cmsnoteid=CMS%20AN-2015/080.

[26] *The CMS muon project: Technical Design Report*. Technical Design Report CMS. CERN, Geneva, 1997. URL https://cds.cern.ch/record/343814.

[27] The CMS Collaboration. The CMS trigger system. *Journal of Instrumentation*, 12(01): P01020–P01020, Jan 2017. ISSN 1748-0221. doi: 10.1088/1748-0221/12/01/p01020. URL http://dx.doi.org/10.1088/1748-0221/12/01/P01020.

[28] T. Sjöstrand and et al. An Introduction to PYTHIA 8.2. *Comput. Phys. Commun.*, 191:159–177, 2015. doi: 10.1016/j.cpc.2015.01.024.

[29] D. J. Lange. The EvtGen particle decay simulation package. *Nucl. Instrum. Meth.*, A462:152–155, 2001. doi: 10.1016/S0168-9002(01)00089-4.

[30] E. Barberio, B. van Eijk, and Z. Was. PHOTOS: A Universal Monte Carlo for QED radiative corrections in decays. *Comput. Phys. Commun.*, 66:115–128, 1991. doi: 10.1016/0010-4655(91)90012-A.

[31] I. P. Lokhtin and A. M. Snigirev. A Model of jet quenching in ultrarelativistic heavy ion collisions and high-p_T hadron spectra at RHIC. *Eur. Phys. J.*, C45:211–217, 2006. doi: 10.1140/epjc/s2005-02426-3.

[32] T.-W. Wang. *Probing Quark-Gluon Plasma with Beauty Quarks*. PhD thesis, MIT, 6 2019.

[33] The CMS Collaboration. Dimuon performance studies in 2015 5.02 TeV pp and PbPb data. CMS AN Note 2016/048, 2016. URL http://cms.cern.ch/iCMS/jsp/db_notes/noteInfo.jsp?cmsnoteid=CMS%20AN-2016/048.

[34] K. Prokofiev and T. Speer. A kinematic and a decay chain reconstruction library. 2005. doi: 10.5170/CERN-2005-002.411. URL https://cds.cern.ch/record/865614.

[35] A. Hocker et al. TMVA - Toolkit for Multivariate Data Analysis. 2007.

[36] B. P. Roe, H.-J. Yang, J. Zhu, Y. Liu, I. Stancu, and G. McGregor. Boosted decision trees, an alternative to artificial neural networks. *Nucl. Instrum. Meth.*, A543(2-3):577–584, 2005. doi: 10.1016/j.nima.2004.12.018.

[37] M. Cacciari, M. Greco, and P. Nason. The p_T spectrum in heavy flavor hadroproduction. *JHEP*, 05:007, 1998. doi: 10.1088/1126-6708/1998/05/007.

[38] W. Verkerke and D. Kirby. *RooFit Users Manual v2.91*, 2008. URL https://root.cern.ch/download/doc/RooFit_Users_Manual_2.91-33.pdf.

[39] F. James. *MINUIT - Function Minimization and Error Analysis*. CERN, 2008. CERN Program Library Long Writup D506.

[40] Y.-S. Zhu. On Statistical Significance of Signal. *HEPNP*, 30:331–334, 2006.

[41] The CMS Collaboration. Measurements of inclusive W and Z cross sections in pp collisions at $\sqrt{s}$ = 7 TeV. *Journal of High Energy Physics*, 2011(1):80, Jan 2011. ISSN 1029-8479. doi: 10.1007/JHEP01(2011)080. URL https://doi.org/10.1007/JHEP01(2011)08.

[42] M. Pivk and F. R. Le Diberder. SPlot: A Statistical tool to unfold data distributions. *Nucl. Instrum. Meth.*, A555:356–369, 2005. doi: 10.1016/j.nima.2005.08.106. URL http://dx.doi.org/10.1016/j.nima.2005.08.106.

[43] The CMS Collaboration. Charged-particle nuclear modification factors in PbPb and pPb collisions at $\sqrt{s_{\mathrm{N\,N}}} = 5.02$ TeV. *JHEP*, 04:039, 2017. doi: 10.1007/JHEP04(2017)039.